Multimodal X-ray imaging with Hartmann masks

Zur Erlangung des akademischen Grades einer

DOKTORIN DER INGENIEURWISSENSCHAFTEN (Dr.-Ing.)

von der KIT-Fakultät für
Elektrotechnik und Informationstechnik
des Karlsruher Instituts für Technologie (KIT)

angenommene

DISSERTATION

von

M.Sc. Margarita Zakharova
geb. in Tomsk, Russland

Tag der mündlichen Prüfung:	25.02.2022
Hauptreferent:	Prof. Dr. Ulrich Lemmer
Korreferent:	Dr. habil. Anton Plech

Nobody in this world can tell me what to think, but I think everybody has a lesson to teach me.
Lex Fridman

To my father

Kurzfassung

Die multimodale Röntgenbildgebung mit Hartmann-Masken ist ein nicht - interferometrisches Single-Shot-Verfahren. Dabei werden kundenspezifische optische Komponenten, Hartmann-Masken, verwendet, um Absorptions-, Differenzphasen- und Streukontrastmodalitäten in einem einzigen Projektionsbild zu erzielen. Diese Bildgebungsmethode kann in einem robusten Röntgenaufbau implementiert werden; sie kann mit breitbandiger Strahlung betrieben werden, ermöglicht einen entspannten Aufbau und eine beträchtliche Vielseitigkeit, was für die Charakterisierung dynamischer Prozesse entscheidend ist. Trotz ihrer Einschränkungen in Bezug auf die räumliche Auflösung ist diese Methode vielversprechend für Anwendungen, die dynamische Messungen auf verschiedenen Zeitskalen erfordern.

Eine herkömmliche Hartmann-Maske ist eine Anordnung von Löchern in einem undurchsichtigen Material. Bei der Anwendung in einer Röntgenanlage wirft die Maske einen Schatten auf den Detektor. Die Maskenprojektion wird als Referenz verwendet, um sie mit der durch die Probe gestörten Wellenfront zu vergleichen. Diese Verzerrungen werden quantifiziert und der Abschwächung, der Brechung der Röntgenstrahlen (Phasenverschiebung) oder der Kleinwinkelstreuung in der Probe zugeschrieben. Drei Kontrastmodalitäten (Absorptions-, Phasen- und Streukontrast) können komplementär genutzt werden, um auf zerstörungsfreie Weise auf die Struktur der Probe zu schließen. Die Wellenfrontabtastung mit Hartmann-Masken ist ein echter Single-Shot-Ansatz, da sie kein Scannen von Probe und Maske oder Dithering erfordert.

Neben der herkömmlichen Hartmann-Maske ist auch ein umgekehrtes Design möglich - eine Anordnung von absorbierenden Säulen auf einem transparenten Substrat. Ein solches Design bietet eine höhere Flux-Effizienz aufgrund einer geringeren Absorption im optischen Element und eine größere Fläche der Probe, die mit den Röntgenstrahlen wechselwirkt. Beide Maskendesigns können mit hochverfügbarer UV-Lithographie in Kombination mit Metallgalvanik hergestellt werden. Im Rahmen dieser Arbeit wurde ein Herstellungsverfahren für beide Maskendesigns auf Silizium- und Graphitsubstraten entwickelt. Die Masken können auf die endgültige Anwendung der zerstörungsfreien Charakterisierung in Wissenschaft und Industrie zugeschnitten werden.

Ein wesentlicher Aspekt bei der Herstellung von Optiken ist die Rückkopplung von Charakterisierungs- und Qualitätsbewertungsmethoden für eine rationelle Optikentwicklung und -optimierung. In dieser Arbeit wird ein Charakterisierungsansatz vorgeschlagen, der auf den relativen Absorptionshistogrammen basiert, um die Wellenfrontmodulation von konventionellen und invertierten Hartmann-Masken zu vergleichen. Die Leistung der Masken wird unter Verwendung von Synchrotronstrahlung und einer Labor-Röntgenröhre untersucht, was die Vorteile des invertierten Hartmann-Maskendesigns für eine höhere Bildqualität und eine geringere Kreuzkorrelation zwischen den verschiedenen Kontrastmodalitäten zeigt.

Die multimodale Röntgenbildgebung mit konventioneller und invertierter Hartmann-Maske ist eine vielseitige und vielversprechende Technik, die auf eine bestimmte Anwendung zugeschnitten werden kann. Die In-situ-Visualisierung chemischer Reaktionen und die Darstellung des schnellen Laserabtragungsprozesses bestätigen die breite Anwendbarkeit dieser Bildgebungstechnik auf verschiedenen Zeitskalen - von Sekunden bis Mikrosekunden. Die angestrebte Zeitauflösung für die multimodale Röntgenbildgebung mit Hartmann-Masken wird in erster Linie durch die Eigenschaften des Detektors (z. B. die Bildaufnahmerate) und die Brillanz der Quelle bestimmt, ist aber nicht durch das Verfahren selbst begrenzt. Bei Verwendung einer

geeigneten Quelle und eines geeigneten Detektors können sogar schnellere Prozesse mit drei Kontrastmodi sichtbar gemacht werden.

In dieser Arbeit wird die Nutzung der Streuungsinformationen, die im Rahmen der multimodalen Bildgebung mit Hartmann-Masken gewonnen werden, näher erläutert. Aufgrund der Vielseitigkeit des Aufbaus ist es möglich, eine Feinabtastung der Autokorrelationsfunktion der Elektronendichte durchzuführen. Dies ermöglicht die Schätzung quantitativer Strukturparameter wie Größe und räumliche Organisation von Probenmerkmalen im sub-µm-Bereich, der weit unter der Auflösung des Bildgebungssystems liegt. Für einen Graphit mit feinen Poren konnten die durchschnittliche Porengröße, der relative Porenbruch und der Wert des Hurst-Exponenten bestimmt werden, der das Raumfüllungsvermögen der Struktur charakterisiert. Eine derart vielseitige und einfache Technik kann sich auf die Forschung auswirken, die sich mit der Untersuchung komplexer Strukturen wie poröser Materialien, Kolloide oder Pulver befasst. Abgesehen vom unmittelbaren Nutzen für die Entwicklung und Charakterisierung poröser katalytischer Materialien können zahlreiche medizinische Anwendungen im Zusammenhang mit der Krebsfrühdiagnostik und Lungenkrankheiten von den Informationen über Morphologie und fraktale Dimensionen komplexer, miteinander verbundener Strukturen profitieren.

Abstract

Multimodal X-ray imaging with Hartmann masks is a non-interferometric single-shot technique. It utilizes customized optical components, Hartmann masks, to achieve absorption, differential phase, and scattering contrast modalities from a single projection image. This imaging method can be implemented within a robust radiographic setup; it can operate with broadband radiation, allows for relaxed setup requirements, and considerable versatility, which is crucial for characterizing dynamic processes. Despite its limitations in terms of spatial resolution, this method is promising for applications requiring dynamic measurements at different time scales.

A conventional Hartmann mask is an array of holes in an opaque material. When applied in a radiographic setup, the mask casts a shadow on the detector. Mask projection is used as a reference to compare with the wavefront disturbed by the sample. These distortions are quantified and attributed to the attenuation, refraction of X-rays (phase shift), or small-angle scattering in the specimen. Three contrast modalities (absorption, phase, and scattering contrasts) can be used complementary to infer the sample's bulk structure in a non-destructive way. The wavefront sensing with Hartmann masks is a truly single-shot approach, as it requires no sample/mask scanning or dithering.

Apart from the conventional Hartmann mask, an inverted design is possible - an array of absorbing pillars on a transparent substrate. Such design provides higher flux efficiency due to lower absorption in the optical element and offers a larger area of the sample to interact with the X-rays. Both mask designs can be fabricated with highly available UV lithography combined with metal electroplating. This work established a fabrication process for both mask designs on silicon and graphite substrates. The masks can be tailored to the final application of non-destructive characterization in science and industry.

An essential aspect of optics manufacturing is feedback from characterization and quality assessment methods for a rational optics design and optimization. This thesis proposes a characterization approach based on the relative absorption histograms to compare the wavefront modulation offered by the conventional and the inverted Hartmann mask designs. The performance of the masks is accessed using synchrotron radiation and laboratory X-ray tube, which shows the advantages of the inverted Hartmann mask design for higher quality images and reduced cross-correlation between different contrast modalities.

Multimodal X-ray imaging with conventional and inverted Hartmann masks is a versatile and promising technique, which can be tailored towards a specific application. *In situ* chemical reaction visualization and imaging of the fast laser ablation process confirm the vast applicability of this imaging technique at different time scales- from seconds to microseconds. The targeted time resolution for multimodal X-ray imaging with Hartmann masks is primarily defined by the characteristics of the detector (e.g., frame acquisition rate) and the brilliance of the source, but is not limited by the approach itself. Even faster processes can be visualized with three contrast modes given an appropriate source and a detector are used.

This work elaborates in greater detail on the use of the scattering information obtained within the multimodal imaging with Hartmann masks. Previous landmark work investigated the relations between the autocorrelation function of electron density and the scattering signal available in other imaging techniques; however, most of them lacked setup simplicity or offered a poor sampling rate. Due to the versatility of the setup,

it is possible to perform a fine scanning of the autocorrelation function of electron density. It enables the estimation of quantitative structure parameters such as sizes and spatial organization of sample features at sub-µm scale, which is well below the resolution of the imaging system. For graphite with a wide range of pore sizes (from tens of nm to several µm) several bulk microstructure characteristics have been estimated. It was possible to determine the average pore size, relative pore fracture, and the Hurst exponent value, which characterizes the space-filling capacity of the structure. Many research areas devoted to studying complex microstructures, including *in situ* and *operando* measurements, can directly profit from the setup's simplicity and relaxed requirements on the optical element and beam coherence.

Acknowledgement

Many people have supported me throughout my Ph.D. journey, and I would like to express my gratitude here to some of them, Without whom this work would not have been possible.

I am grateful to my doctoral supervisor Prof. Dr. Uli Lemmer, who was always supportive and friendly, and helped me every time I needed it. Thank you for the opportunity to do my Ph.D. under your supervision! I also thank Dr. habil. Anton Plech for being a co-referent for this thesis, for his deep knowledge and thoughtful comments.

I want to express immense gratitude to my immediate supervisor, Dr. Danays Kunka, for supporting me professionally and privately through many challenges that I have faced during this time. Thank you for believing in me; I hope to always keep in touch with you.

Big thanks to our research group and many other fellow Ph.D. students at the IMT. Special thanks to Andrey Mikhaylov and Vitor Vlnieska for our fun times in the office and at the Schmidt's Katze. Thanks to Heike Fornasier I learned many things in the cleanroom, including always staying positive and having a good laugh when things go sideways. Big thanks to Alexandra Moritz for always being positive and cheerful, and doing amazing work in the IMT workshop. I owe many thanks to all KNMFi and IMT staff for multiple training they gave me and for answers to my many questions. Thanks to Dr. Stefan Reich for providing his scripts and prompt and thoughtful feedback to paper drafts. I am also grateful to Prof. Dr. Sergio Pezzin for the excellent work together and the opportunity to gain teaching experience when giving lectures to students at UDESC. I thank Sabine Bremer and Marcus Zuber for our beamtimes at Topo-Tomo and in CT-lab.

I am grateful to Karlsruhe School of Optics and Photonics (KSOP) and Karlsruhe House of Young Scientists (KHYS) for the funding of my Ph.D., as well as friendly and straightforward communication. Thank you for your multiple initiatives to support and foster the development of Ph.D. students at KIT!

I have the deepest gratitude to all the doctors who saved my life, both in Russia and Germany. Special thanks to Dr. med. Michael Schatz from ViDia Kliniken Karlsruhe and Prof. Dr. med. Mark Ringhoffer and his team from Städtisches Klinikum Karlsruhe for their expertise and professionalism. From my journey I have learned about the most immediate impact of science on saving peoples lives, which gave me motivation to continue devoting my life to it.

I want to thank my university friends: we shared many conversations and exchanged our academic experiences as women scientists, which helped me a lot and gave perspective.Thanks to my oldest friends: Katya, Ira, and Lyuda. I hope our friendship that started at High School will surpass all the distances and time zones.

I am deeply grateful to my sister and my parents, who were always by my side even when many kilometers away. To my mother, who is and always will be an inspiration for being strong and never withdraw in the face of injustice. To my father, who was the source of my interest to physics and books. I love you, and I will always miss you. Thank you both for always helping me to pursue my dreams. And very special thanks to my husband Nicolás, you are always my support and motivation; your optimism and strength kept me going through the most challenging times and made the happy moments brighter.

Contents

1 Introduction

Multimodal X-ray imaging is a non-destructive technique, which offers complementary information on the inner structure of objects and augments the conventional radiography based on absorption contrast [1, 2]. Multimodal (or multi-contrast) X-ray imaging methods enable the detection of X-rays refraction and scattering, which occurs when X-rays are passing through the object under investigation. The methods benefit from the wave properties of X-rays. When the propagating wave encounters an interface, it changes its direction of propagation (gets refracted), which results in the phase shift relative to the incident wave. When these changes are detected, they form a phase-contrast image. If the X-rays encounter an isolated small obstacle, they get scattered, which leads to the decrease in final image contrast and forms dark-field, or scattering, contrast.

The first contrast modality to be introduced in addition to the conventional absorption was phase contrast [3]. The refraction angles of X-rays for the high radiation energy (typically 10-30 keV for X-ray imaging) are extremely small, making their detection a challenging task. Despite significant progress in X-ray detection technology, the available pixel size is limited, making it challenging to achieve phase contrast within a compact imaging setup. One needs to combine state-of-the-art X-ray optics with novel data handling and contrast retrieval algorithms to overcome this limitation. Advances in optics manufacturing and data analysis led to many successful applications of multimodal X-ray imaging in medicine [4, 5], materials science [6, 7], and industrial quality control [8, 9].

Another essential feature of multimodal X-ray imaging is the availability of scattering information. It arises from the scattering of the X-rays on micro and nanostructures smaller than the resolution available within the setup. It produces fringes which the X-ray camera cannot directly resolve. Even though the accuracy of such measurements cannot be compared to the actual small-angle X-ray scattering measurement (SAXS), certain scattering signals can be extracted even within a simple setup along with absorption and phase-contrast images. Due to the size-sensitivity of the scattering signal, it potentially allows for selective imaging and discrimination between nano-sized scattering centers in a qualitative manner [10, 11, 12]. It is important to note that the signal-to-noise ratio for the scattering channel in this modality is low due to the high noise levels as the detector records attenuated beam, which has contributions from absorption and scattering together.

The first implementations of phase-sensitive imaging have been attributed to the various ways of utilizing interferometric effects to quantify phase shifts. There are several interferometric approaches, e.g., single crystal interferometry, analyzer-based interferometry, grating-based interferometry [5, 13], etc. Interferometric methods initially have strong requirements on the wavefront coherence, and bandpass: only strongly collimated monochromatic beams can be applied, provided by the synchrotron facilities. For grating-based interferometry, additional transmission gratings enable imaging with polychromatic cone beams provided by X-ray tubes. Such imaging geometry is called Talbot-Lau interferometry [14].

Grating-based interferometry is one of the most common approaches to achieve phase and scattering contrasts and to extend the applications of multimodal X-ray imaging to laboratory sources [4]. Albeit, it comes at the cost of the simplicity of the imaging setup. A complicated image acquisition system with challenging to manufacture high aspect-ratio optics allows for relaxing wavefront requirements but makes the setup highly prone to mechanical instabilities due to the required precision movements at the scale of microns. This

limits the versatility of the setup and complicates the introduction of any rearrangements. High absorption in the optical elements also limits the photon statistics, which can be crucial for time-resolved measurements. Non-interferometric approaches, such as edge-illumination methods [15, 16], use less challenging optical elements and can be used for single-shot imaging (beam-tracking approach [17]). However, this technique was so far implemented only with sample scanning or dithering [17, 18] due to the limited grating area available.

Despite the remarkable results in imaging achieved by these techniques, there is still an open question of whether it is possible further to optimize the stability of the setup, acquisition time and flux efficiency [19]. From this perspective, one of the most promising approaches is utilizing a single optical element in a single-shot configuration [20, 21]. Implementing only one optical component in the beam path relaxes alignment requirements, increases the mechanical stability and versatility of the setup, and significantly reduces the attenuation introduced by the optical element. Single-shot acquisition of imaging information in its turn substantially shortens the total exposure time, simplifies the experimental procedure, and reduces the total amount of data to be processed.

This approach can operate with broadband radiation and generally allow for relaxed setup requirements, and considerable versatility [20, 21, 22]. It does not necessitate scanning the optical elements unless a high-resolution image is required. Moreover, single-exposure multimodal X-ray imaging methods are compatible with two-dimensional optical elements. One-dimensional gratings conventionally used in grating-based phase-contrast imaging allow only for the orientation-dependent analysis of structures because they offer sensitivity only in the direction perpendicular to the grating lamellas [23]. On the contrary, two-dimensional gratings provide enhanced information on the material structure in several directions [20, 23, 24, 25, 25].

When combined with two-dimensional absorption grating, the single-exposure imaging method provides a tool that allows for measuring phase shifts in two directions within a simple, robust setup. In this case, two-dimensional grating serves as a Hartmann mask [26], which is a wavefront sensor consisting of an array of apertures introducing spatial beam modulation. Each beamlet produced by the apertures gets displaced proportionally to the gradient of the phase shift. This concept is widely used in optical metrology and astronomy but can be extended towards X-ray imaging provided suitable materials are used to cast a shadow on the detector.

Hartmann masks are represented by a matrix with periodically alternating opaque and transparent structures. When X-ray radiation is incident on the mask, it is partially transmitted by the substrate (ideally transparent for X-rays). In contrast, radiation incident on the opaque structures is predominantly absorbed. Diffraction on the multiple apertures occurs, but its effect is feeble due to the low absolute cross-section for short wavelength of X-rays. The mask converts X-ray tube radiation into multiple coherent sources; the wavefront is sampled to create a pattern inverse to the mask design. Alternatively, the inverted design - an array of free-standing absorbing pillars - can be used.

Another optical element with a similar working principle is a Shack-Hartmann sensor [27, 28, 29], which is a two-dimensional array of compound refractive X-ray lenses. An array of microlenses improves flux efficiency through the focusing of the beam instead of using an array of obstructions to block parts of it. However, such sensors are difficult to manufacture and are intrinsically chromatic due to the focusing nature of beamlet formation. The application of such sensors for the white beam radiation is limited, while Hartmann masks do not impose any coherence requirements on the beam. Another practical advantage of the Hartmann masks is that they are much easier to manufacture and scale to cover a large field of view (FoV). Shack-Hartmann sensors for hard X-rays have been manufactured using three-dimensional direct laser writing system [27, 28] (achieved FoV = 2 mm x 2 mm), an embossing process of polyimide foils [29] (FoV

= 6.5 mm x 6.5 mm), and deep X-ray lithography (FoV = 1.87 mm × 1.87 mm). In this work, Hartmann masks with areas up to 25 cm$^(2)$ are routinely achieved within an accessible manufacturing procedure.

The robustness and rapidity of imaging with Hartmann masks come at the cost of reduced spatial resolution of the final images. This can be compensated by a sub-pixel resolution approach when the optical component is scanned in the lateral direction [28]. It makes high-resolution measurements more time-consuming than single-shot imaging, but such an option can be introduced within this method when required by the application. Although all three contrast modalities can be obtained for each shot, the retrieved image quality for the contrast of particular interest can be improved by adjusting the setup and optical component towards the chosen application. For instance, high-resolution absorption and phase contrast images require a small mask period, while imaging of scattering structures might require larger periods to access a certain correlation length [30, 31].

The aim of this thesis is to investigate the capabilities of the multimodal X-ray imaging with conventional and inverted Hartmann masks. For this, the customized Hartmann masks were developed using highly available UV lithography and metal electroplating. The advantages of this fabrication approach is that many important structural and performance features of the optical components can be tuned: mask size (available field of view), period (structural size of features), visibility (low absorbing substrates in combination with high absorbing structures), uniformity of the pattern (periodicity, defect-free pattern), etc.

Hartmann mask characterization method aimed to guide and enhance the fabrication process is proposed in this work. It allows to evaluate the wavefront modulation offered by the mask in terms of the relative absorption histograms. After a comparison of the conventional and inverted Hartmann mask designs using synchrotron and laboratory sources, it is established that the inverted design is advantageous in terms of achieved image quality and the diminished cross-talk between contrast channels. The inverted Hartmann masks are further applied for visualization of dynamic processes at different time scales: from real-time monitoring to fast imaging.

Scattering contrast modality available within the multimodal X-ray imaging exhibits dependence on setup parameters. Versatility of the imaging setup with Hartmann masks allows for a fine scanning of the correlation length by moving the mask along the optical axes. Scattering intensity measured through the dampening of mask contrasts provides an insight to the sub-µm bulk structure of the object. Evaluating scattering intensity at different probed correlation lengths provides a tool for quantitative characterization of structures well below the resolution of the imaging setup.

Following the Introduction, Chapter 2 addresses the basics of the interaction of X-rays with matter relevant to X-ray imaging. It elaborates on phase and scattering contrast modalities and which physical phenomena they represent.

Chapter 3 covers the development and characterization of conventional and inverted Hartmann masks with UV lithography and electroplating on silicon and graphite substrates. This chapter is based on the following publications:

M. Zakharova, V. Vlnieska, H. Fornasier, M. Börner, TdS Rolo, J. Mohr, D. Kunka. Development and Characterization of Two-Dimensional Gratings for Single-Shot X-ray Phase-Contrast Imaging. Applied Sciences. 2018; 8(3):468;

M. Zakharova, S. Reich, A. Mikhaylov, V. Vlnieska, M. Zuber, S. Engelhardt, T. Baumbach, D. Kunka, "A comparison of customized Hartmann and newly introduced inverted Hartmann masks for single-shot phase-contrast X-ray imaging," Proc. SPIE 11032, EUV and X-ray Optics: Synergy between Laboratory and Space VI, 110320U (26 April 2019).

Chapter 4 includes a performance comparison for the conventional and inverted Hartmann masks in a laboratory setup. It demonstrates the application of the inverted Hartmann masks for time-resolved imaging at different time scales: from real-time monitoring to visualization of fast dynamic processes in three contrast channels. This chapter builds on the following publications:

M. Zakharova, S. Reich, A. Mikhaylov, V. Vlnieska, TdS. Rolo, A. Plech, D. Kunka. Inverted Hartmann mask for single-shot phase-contrast x-ray imaging of dynamic processes. Optics Letters. 2019; 44 (9):2306-2309;

M. Zakharova, A. Mikhaylov, V. Vlnieska, D. Kunka. Single-Shot Multicontrast X-ray Imaging for In Situ Visualization of Chemical Reaction Products. Journal of Imaging. 2021; 7 (11):221.

Chapter 5 dives deeper into the quantitative interpretation of scattering (dark-field) contrast, its relation to structure size and organization. It demonstrates how this type of contrast is related to the small-angle scattering and can be used to characterize structures at the sub-micron scale. Parts of this chapter related to analyzing scattering intensity via the standard visibility will be published in:

M. Zakharova, A. Mikhaylov, S. Reich, A. Plech, D. Kunka. Bulk morphology of porous materials at sub-micrometer scale studied by dark-field X-ray imaging with Hartmann masks.

2 Theoretical background

2.1 Basics of the interaction of X-rays with matter

When an X-ray photon interacts with an atom, it can be either absorbed or scattered, i.e., change its direction of propagation. In the photoelectric absorption process, an X-ray photon is absorbed by the atom. The excess of energy is transferred to an electron, which leaves the shell. Thus, the ionization process occurs. Suppose we treat the matter as a continuous medium and X-rays as an electromagnetic wave. In that case, the change of direction of propagation at the interface between the different media is equivalent to refraction. For the X-rays, the refractive index of materials is slightly less than 1 (refractive index for vacuum) and can be expressed as:

$$n = 1 - \delta + i\beta, \tag{2.1}$$

where δ is of order 10^{-5} for solids, and β is about 10^{-8} - much smaller than δ. Small angular deviations due to refraction are directly proportional to the gradient of phase for the refracted beam. The group of methods that exploit refractive properties of materials are called phase-contrast imaging.

For the range of energies typically employed in X-ray imaging (10-60 keV), the interaction of X-rays with matter can be described by the phenomena of photoelectric absorption, the elastic collisions described by the classical Thomson model, and the inelastic collisions described by the Compton model. The elastic scattering is related purely to the change of direction of propagation, and no change in the kinetic energy occurs. The classical approximation is valid when the photon momentum is taken up by the by atom and the lattice, which predominantly occurs at the lower energies (e.g., below 20 keV for carbon, see Figure 2.1), then decreasing dramatically for higher energies. In the inelastic scattering, the portion of the photon energy is transferred to the electron, and thus the energy of the scattered wave is reduced. Inelastic scattering is predominant for higher energies and larger scattering angles; it is incoherent and varies slowly with scattering angle [32].

2.2 Multimodal X-ray imaging

When the radiation passes through the sample, the wave field gets affected by the sample's structure. By analyzing the wave-field alterations induced by the object through the intensity measurements, one can infer the object's internal structure. The wave field, being a complex entity, has the magnitude and phase component related to the intensity of the X-rays and the direction of their propagation, respectively. The intensity of the X-rays can be recorded by the X-ray detector, which is commonly represented by a CCD camera coupled with a scintillator. The direction of the wave field, or its phase, cannot be directly measured unless sufficient propagation distance is introduced to resolve the changes in intensity distribution induced by refraction in the sample. To implement phase-contrast imaging within a compact setup, one could prefer other near-field approaches.

Generally, multimodal X-ray imaging methods can be represented by an imaging setup with optical elements before and/or after the sample under investigation, as can be seen in Figure 2.2. The projections of the

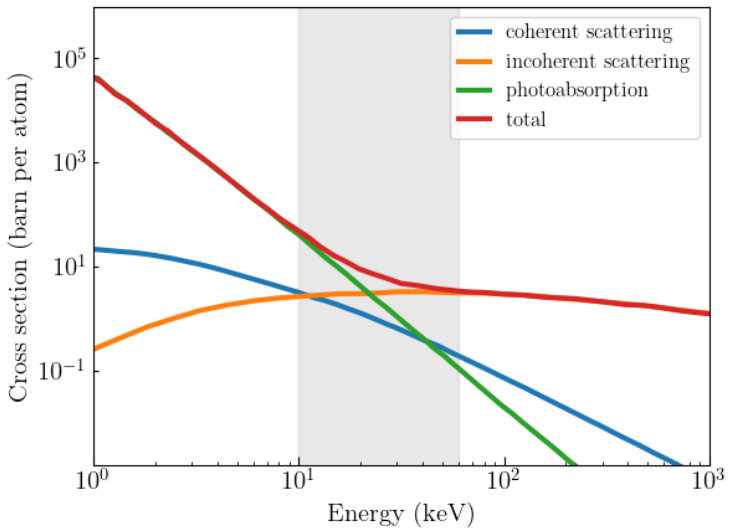

Figure 2.1: Atomic cross sections of neutral carbon for photoabsorption, elastic and inelastic scattering (based on [33]). Shaded area indicated the energy range typically applied in X-ray imaging.

object and the wavefront modulation offered by the optical elements are recorded by the detector and then compared to the reference projection with only the optics in the beam path. By analyzing the differences in the wavefront caused by the presence of the object, one can retrieve three contrast modalities. Absorption contrast is evaluated as a general decrease in transmitted intensity, phase contrast as a shift in the wavefront modulation (distortions of the wavefront), and scattering (also called dark-field) contrast through the decrease in image sharpness (e.g., visibility reduction for gratings).

Several methods are used to achieve phase contrast in a compact imaging setup, each having relative strengths and limitations. For example, there have been significant advances in Talbot-Lau interferometry (TLI), which usually employs three one-dimensional gratings: source grating, phase grating, and absorption grating. The gratings are precisely aligned, and by moving the phase and absorption grating relative to each other, one obtains a stepping curve for each pixel of the system from several projections (at least three). This curve can then be used to evaluate three contrast modalities: absorption contrast, phase contrast, and dark-field (or scattering) contrast. The multimodality of the obtained contrast attracted a lot of attention and interest to the method, especially considering its relaxed requirements on the beam coherence, bandwidth, and large sample sizes compared to other phase and scattering sensitive techniques. These advantages enable the extension of the phase imaging towards laboratory sources and pave the way for more comprehensive medical imaging and industrial material characterization.

While being a promising approach, TLI has several limitations related to the complexity and mechanical instability of the setup. The need for high-quality, high aspect ration gratings and their precise alignment complicates the applicability of the method, and the presence of multiple highly absorbing optical elements limits the flux efficiency and photon statistics at the detector. This creates a bottleneck for studying dynamic processes or reducing exposure dose for medical applications. There have been several successful optimizations of the method aimed to extend it to a single-shot approach. However, they either require a certain movement [19, 34, 35] or a complicated and very precise absorption grating with shifted linear structures [36]. The same applies to the edge-illumination methods, which require dithering [18] or a complicated asymmetrical mask [37].

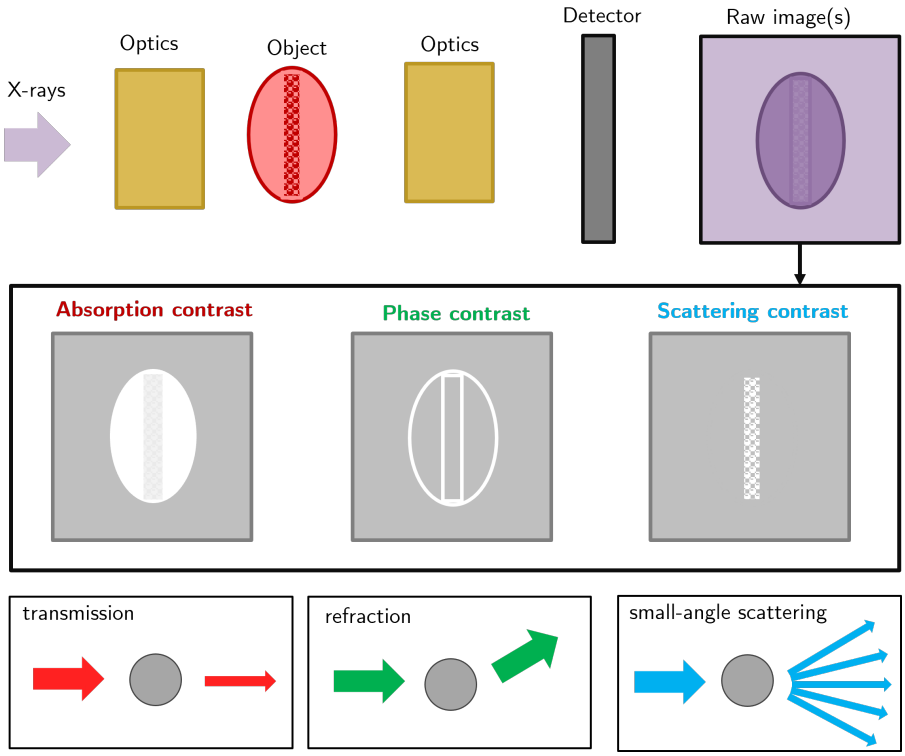

Figure 2.2: Schematic of the generalized multimodal X-ray imaging setup: The X-rays transverse the optical element (or a set thereof), then pass through the sample, and the second set of optical elements (if present). The position-sensitive detector captures the intensity of the exit field of the system, which is a raw image or a set of raw images. These data are used to retrieve three contrast modalities: absorption, phase, and scattering contrast.

In response to the growing interest in multimodal imaging methods, another phase-sensitive method has been extended towards imaging. Based on Hartmann and Shack-Hartmann sensors, wavefront sensing was actively applied in wavefront metrology as it provides a straightforward way to evaluate the phase shifts. The main idea of wavefront sensing with the Hartmann mask is that the known (usually periodic) pattern is projected onto the detector. The absorbing array casts a shadow on the sensor, which is recorded prior to the measurements with the sample of interest and is further used as a reference. When the specimen is placed in the setup, it distorts the wavefront: the beam intensity decreases due to absorption, and the direction of the rays changes as they refract and diffract on the inhomogeneities of the sample (its electron density). By analyzing these distortions in terms of intensity decrease, displacement, and broadening of the beamlets, one can evaluate the absorption, phase, and scattering contrast, respectively.

Conventional Hartmann mask is represented by an array of holes in the absorbing material, which creates a structured illumination: an array of beamlets. However, the inverted Hartmann mask design can also be applied within the same approach. Such design can be beneficial for increasing photon statistics at the detector as it provides higher flux-efficiency: more photons interact with the object, which leads to a higher signal-to-noise ratio in the final images. The advantage of X-ray imaging with Hartmann masks is that all three contrast modalities can be retrieved from a single overlapped mask-object image, which makes the measurements faster and the delivered dose lower. Besides, since the Hartmann mask is two-dimensional, the phase shift in two orthogonal directions is detected. These directional images can help to retrieve the phase map from a single projection.

Along with the advantages mentioned above, imaging with Hartmann masks has inherent limitations. Quick and straightforward measurements come at the cost of the decreased resolution: the final image pixel is defined by the mask period, as the values of intensity, shift, and broadening are obtained within the unit cell

of the mask. This limitation can be addressed by a sub-pixel resolution approach [28] where the single-shot nature of measurements is not crucial. Moreover, having a larger mask period also provides a larger angular width for the detection of the scattering contrast. As this Chapter and Chapter 5 will further discuss, it might be advantageous to sacrifice the resolution of the final image to access small correlation lengths which are related to larger scattering angles.

2.3 Absorption contrast

A famous image of Röntgen's wife's hand has started an era of X-ray imaging in 1895 [38]. In this famous picture, the bones and the wedding ring are clearly distinguishable: it is caused by the significant difference between the absorption coefficient of the bone, metal, and the surrounding tissue of the hand. Due to the low value of the absorption coefficient for soft tissues, the skin and muscles of the hand are barely visible. On the contrary, the absorption coefficient is high for the metal and bone: heavier elements absorb many photons. Thus, the contrast between the areas with many and few photons is acquired. The X-rays passing through the soft tissues, mainly consisting of light elements such as carbon, do not get sufficiently absorbed to be distinguishable from the air on the film (detector plane). If the X-rays with initial intensity I_0 are passing through the object along the z axis, the intensity at the detection plane $I(x, y)$ in case of contact region can be described according to the Beer-Lambert law [32]

$$I(x, y) = I_0 \exp\left(\int \mu(x, y, z)dz\right), \tag{2.2}$$

where the absorption coefficient μ is assumed to be non-uniform for the real object. Thus, by comparing the initial intensity I_0 with the intensity I, recorded after X-rays passed the object, the projection of the absorption coefficient can be retrieved:

$$\log\left(\frac{I}{I_0} = \int \mu(x, y, z)dz\right) \tag{2.3}$$

Such a direct projection approach is valid only for the contact region free of Fresnel or Fraunhofer diffraction effects. This distance is limited by the condition $L \ll D^2/\lambda$, where D is the structure size, and λ is the X-ray wavelength. The absorption coefficient can be expressed as [32]:

$$\mu = \frac{4\pi}{\lambda}\beta, \tag{2.4}$$

where β is the imaginary part of the refractive index, which denotes absorption. Then the optical density for the material thickness t, which is the input data for the X-ray absorption tomography, is represented by

$$D = -\log\left(\frac{I}{I_0}\right) = \frac{4\pi}{\lambda}\beta t. \tag{2.5}$$

Later in this chapter, some specific algorithms for absorption contrast retrieval will be addressed. Usually, the setup conventional for X-ray imaging based on absorption is quite simple and consists of the X-ray source and the detector, between which the object is placed. Thus the resolution of the final image is defined by the resolution of the detecting system.

2.4 Phase contrast

Phase contrast arises from the refraction of the rays passing through the object. As a phenomenon, it can be observed for various wave fields, e.g., visible light, electrons, neutrons, and X-rays. Phase-contrast imaging is applied for visualization of the otherwise transparent structures - usually composed of low-absorbing material. There are many ways to achieve phase contrast: free-space propagation, interference, holography, Zernike phase contrast, etc. This work will discuss the phase-contrast X-ray imaging obtained within non-interferometric methods based on wavefront sensing with a reference pattern.

Phase-contrast image shows the angular distribution of X-rays introduced to the wave after passing the object with refractive index variations. The angular distribution is directly proportional to the gradient of the phase $\phi(\vec{r}) = \vec{k'} \cdot \vec{r}$ of the refracted beam. The direction of the refracted beam is $\vec{k'}/k' = (\lambda/2\pi)\nabla\phi(\vec{r})$, then the angular distribution as a function of the coordinates (x, y) in plane perpendicular to the direction of propagation of the beam is

$$\alpha_x = \frac{\lambda}{2\pi}\frac{\partial\phi(x,y)}{\partial x} \text{ and } \alpha_y = \frac{\lambda}{2\pi}\frac{\partial\phi(x,y)}{\partial y}. \tag{2.6}$$

As have been discussed above, the refractive index of X-rays depends on the electron density distribution in the object, which defines the refractive index $n = 1 - \delta + i\beta$. The refractive index decrement δ and the imaginary part β can be expressed as

$$\delta = \frac{2\pi r_0}{k^2}\rho_e \text{ and } \beta = \frac{\mu}{2k}, \tag{2.7}$$

where ρ_e is the electron density, r_0 classical electron radius, μ is the absorption coefficient, and $k = 2\pi/\lambda$ is the wave vector.

The macroscopic variations of electron density (and thus, δ) that the imaging detector resolves contribute to the formation of phase contrast. However, as will be discussed below, the fine structures that are well below the resolution of the imaging setup contribute to the final image by decreasing the contrast of the resolved structures. This dampening of the contrast can be quantified and attributed to the scattering contrast, which has been reported under many names (coherent scattering in the sample, visibility reduction contrast, diffraction, dark-field contrast, etc.). It will be further referred to as scattering contrast.

2.5 Scattering contrast

In multimodal imaging techniques, scattering contrast have been predominantly attributed to the ultra-small angle scattering (USAXS) in the sample [12, 39], which arises from the structures (electron density variations) which are below the resolution limit of the imaging setup [12, 40]. It depends on the shape, size, and spatial distribution of the scatterers.

Although this type of contrast has attracted a lot of attention in recent years, it remains a point of discussion on how to interpret obtained scattering intensity quantitatively for different scattering structures, define possible contributions to it, and separate it from the noise. Depending on specific sample characteristics (e.g., thickness, absorption cross-section, packaging density, etc.) or the setup implementation (e.g., X-ray energy range, X-ray source, chosen technique), it can contain various contributions in addition to classical SAXS. Scattering contrast depends on the position of the borders of microstructures, and thus the statistical deviations for this type of contrast are significantly larger than for absorption signal [41].

It becomes essential to consider various contributions to the scattering contrast formation when the extension to the laboratory sources is in question, as strong spurious and system-specific inputs have been reported. It has been experimentally demonstrated that for large geometric magnifications (thus, increased spatial resolution), scattering contrast transforms into a differential phase contrast [42].

Thus, the contributions to the scattering signal in multimodal X-ray imaging include but are not limited to:

- contributions of unresolved electron density (refractive index) changes due to randomly distributed microstructures [11, 12, 31];
- unresolvable sharp edges (phase fluctuations) [42, 43];
- structure factor for densely packed particles [39, 44];
- contributions of the polychromatic source, especially in the methods based on the change of visibility due to beam hardening [45, 46];
- contribution of inelastic scattering [44];
- second order derivative of the phase [47];
- local curvatures of the wavefront [48].

To eliminate the inputs to scattering contrast caused by the prevalence of experimental conditions, I will address a low-absorbing single material porous specimen that will be studied using quasi-monochromatic synchrotron radiation in paraxial approximation (parallel-beam geometry). For such densely packed materials, it has been demonstrated that the influence of structure factor leads to a decrease in the scattering signal [39, 44].

The analytical frameworks for quantification of scattering contrast have been derived through wave optics propagation [12, 31] and analysis used in spin-echo small-angle neutron scattering [11, 49, 50]. Both interpretations can be linked and used complementary, as will be discussed in detail in Chapter 5.

2.6 X-ray imaging with Hartmann masks

Hartmann introduced the concept of the Hartmann mask in 1900 in the field of optical metrology of telescope lenses [26]. The idea was used to focus the telescope: the opaque plate with multiple holes was covering the telescope's aperture. When the telescope is pointed towards a light source and is out of focus, multiple secondary light sources can be seen through the apertures. However, only a single image can be seen when the apparatus is focused due to the overlap.

The concept of the Hartmann mask has been later adapted to optical wavefront sensing in different fields ranging from ophthalmology to astronomy. Hartmann wavefront sensor consists of an array of apertures paired with a camera. Usually, a charge-coupled device (CCD), mounted at a distance from the mask (Figure 2.3). The incident wave coming from the source travels along the z-axis. The wavefront is modulated by its aperture pattern when passing through the mask: the incoming beam is divided into an array of small sub-beams. The principle is based on the geometric optical determination of the local slopes of the wavefront (i.e., it's derivative). The camera records the spot distribution yielding the precise position of the beamlets. The wavefront reconstruction is performed by comparing the yielded distribution with the positions of the spots for a reference input beam.

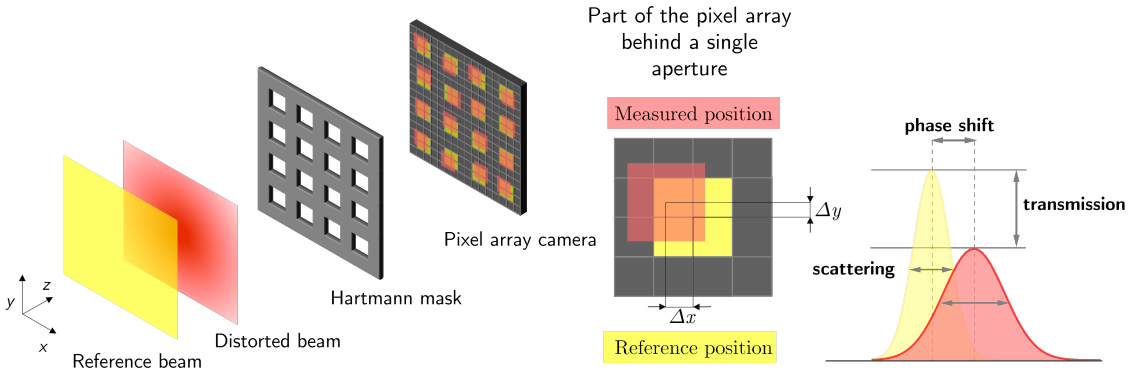

Figure 2.3: The illustration of the Hartmann wavefront sensor operating principle. An imperfect incident wavefront of interest is traveling along the z-axis illuminates a Hartmann mask (aperture array). The mask modulates the beam profile, creating the array of beamlets projected onto the CCD camera. These beamlets' positions are different compared to the reference beam pattern. These displacements can be qualified to provide wavefront reconstruction.

The application of Hartmann sensors for metrological purposes can be extended to X-rays, provided the suitable Hartmann mask with small apertures are fabricated. While Hartmann masks do not provide sensitivity to high spatial frequencies as interferometry does, these sensors have better flexibility and can be integrated into closed-loop adaptive optical systems [51]. The principle has been adapted for X-ray imaging, where the image of the object obtained by the sensor is compared to the flat image of the Hartmann mask. Such comparison yields the distortions of the wavefront introduced by the object, thus providing insight into its internal structure due to the high penetration capabilities of the X-rays. The changes of the projected mask pattern can be classified as changes in the beamlets' positions, a decrease in beamlet intensity, and an increase in its width.

The displacement of the beamlet's position about the ideal mask projection is caused by the refraction phenomena arising at the borders of interfaces inside the object and its borders. The values of this displacement along two axes (δx and δy) divided by the distance from the object to the detector yield the tangent of the refraction angle θ. Since the refraction angles for X-rays are incredibly small (milliradians), we can assume small-angle approximation $\tan(\theta) \approx \theta$. The absorption of X-rays by the imaging object predominantly causes the decrease of intensity. The width of the beamlets is increased due to the small-angle scattering. There are several approaches to analyze the distortion and dispositions of the beamlets, including but not limited to the calculation of respective centroids (first moment of distribution), Fourier analysis, and Gaussian fitting.

Analogous to the time domain heterodyning in radio electronics [52], the presence of the mask adjacent to the object can be understood as spatial heterodyning of phase, and absorption spatial harmonics induced by the object [21]. Under a paraxial beam approximation, the complex amplitude of the wave at the detector plane can be described by the Kirchhoff-Fresnel integral [53]:

$$E(x) = \left(\frac{i}{\lambda z}\right)^{\frac{1}{2}} \exp(-ikz) \int q_{HM}(x') q_{obj}(x') \exp\left[-\frac{i\pi(x-x')^2}{\lambda z}\right] \mathrm{d}x', \tag{2.8}$$

where λ is the wavelength, $k = 2\pi/\lambda$ is the wave vector, q_{HM} and $q_{obj} = \exp[-\mu(x) + i\phi(x)]$ are the transmission functions of the mask and the object, respectively.

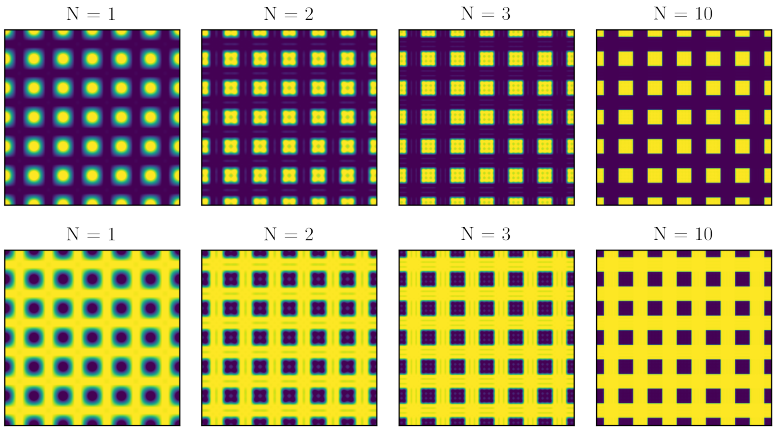

Figure 2.4: The transmission function of the Hartmann and inverted Hartmann masks with different values of N (Eq. 2.9).

Transmission of the ideal Hartmann masks $q_{HM}(x)$ of period P can be represented as a square-wave function that varies from zero to infinity [24]. Then the Fourier expansion of this function gives

$$q_{HM}(x) = \frac{1}{2} + \frac{2}{\pi}\sum_{j=1}^{N}\frac{(-1)^{j-1}}{(2j-1)}\cos\left[(2j-1)\frac{2\pi x}{P}\right], \tag{2.9}$$

where $N \to \infty$. Although, for practical simulations a simplified expression at $N = 1$ can be used:

$$q_{HM}(x) \approx \frac{1}{2} + \frac{2}{\pi}\cos\frac{2\pi x}{P}. \tag{2.10}$$

The illustration of the transmission function for different N is presented in Figure 2.4.

The complex amplitude of the wave after passing through the sample and the mask with the transmission function $q_{HM}(x)$ (Eq. 2.10) can be expressed as

$$\tilde{E}(x) = \frac{1}{2}E(x) + \frac{1}{\pi}\exp\left(\frac{i\lambda z}{P^2}\right)\cdot\left[E(x-\frac{\lambda z}{P})\exp\left(-i\frac{2\pi x}{P}\right) + E(x+\frac{\lambda z}{P})\exp\left(i\frac{2\pi x}{P}\right)\right], \tag{2.11}$$

where $E(x)$ is the complex amplitude of the wave for the object without the presence of the mask (Kirchhoff-Fresnel integral for $q_{obj} = \exp[-\mu(x) + i\phi(x)]$). The distribution of intensity in the final overlapped mask-object projection will be $|\tilde{E}(x)|^2$ can be evaluated numerically using Eq. 2.11.

2.6.1 Conventional and inverted Hartmann mask designs

Besides a conventional Hartmann mask design – an array of regularly spaced apertures – an alternative inverted design is possible: an array of free-standing absorbing pillars, forming a periodic pattern. Such a design could be advantageous because it makes measurement more flux-efficient due to less absorption in the optical component. Increased photon statistics can be crucial for imaging of fast processes or implementation of sophisticated detecting approaches such as sub-pixel resolution with hybrid pixel detectors [18].

Figure 2.5 illustrates the two designs and the intensity profiles they create. As one can see, the conventional Hartmann mask creates an array of beamlets, each creating multiple Gaussian-like distributions of intensity at the detector. The inverted Hartmann mask creates a mesh-like intensity profile, which is the inversed intensity distribution compared to the conventional mask. Babinet's complementarity principle states that

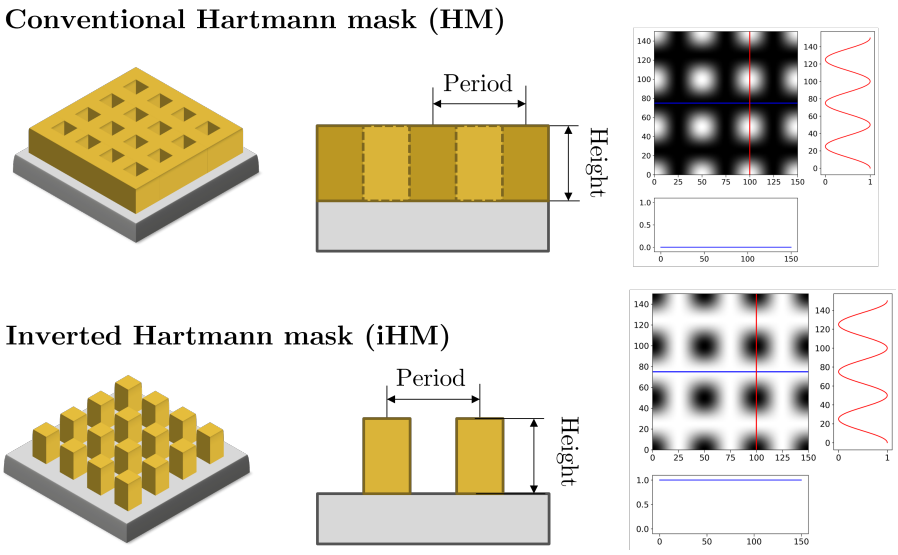

Figure 2.5: An illustration of the two Hartmann masks designs: conventional and inverted. The conventional design is an array of holes in high-absorbing material, and the inverted design is an array of high-absorbing pillars. Both masks cast a periodic shadow onto the detector, either an array of beamlets or a mesh-like intensity profile. The intensity profiles are inversed to each other, making the data analysis approaches directly transferable to X-ray imaging with the inverted Hartmann mask.

the optical response from an aperture is identical to that of a body of the same size and shape except for the overall forward beam intensity. This means that the data analysis approaches developed for analyzing the disturbances in the array of beamlets are directly transferable to X-ray imaging with the inverted Hartmann mask design. The critical difference between the two will be the forward beam intensity and the amount of radiation that has interacted with the object under investigation and has reached the detector. Both masks offer an identical spatial and angular resolution. However, the sensitivity and the signal-to-noise ratio can differ.

The differences in signal-to-noise ratio and the performance of both mask designs will be discussed in the following chapters. It is worth mentioning that the choice of the mask can be motivated by the application. For example, suppose there is a need to decrease the heat load or radiation-induced damage imposed on the specimen during the measurement. In that case, it might be advantageous to use the conventional mask design with a mask placed before the sample.

2.6.2 Relation between scattering contrast and SAXS

The scattering contrast obtained in multimodal X-ray imaging with Hartmann masks has some similarities with the small-angle X-ray scattering (SAXS) method, where the actual scattering curves are obtained. The sampling in single-shot methods is not sufficient to offer a detailed distribution of the scattering intensity. In such a setting, the scattering induced by the object's micro and nanostructure results in broadening of the beamlets or dampening of the projected mask pattern (Figure 2.6). This effect is evaluated for each mask's unit cell (period), and thus the sampling of the scattering curve is limited by the number of pixels per mask period (Figure 2.6). Therefore, such measurements can only be interpreted as a multiplexing of many SAXS measurements performed at once with poor sampling and consequently losing the precision of the results. Despite this drawback, scattering contrast has the advantage of simultaneous macroscopic imaging, which can provide an overview of the scattering distribution in the whole sample in real space [12, 54]. It has relaxed requirements for the setup, which can be advantageous for many applications. Moreover, the poor sampling offered by a single-shot implementation of the method can be compensated by scanning the

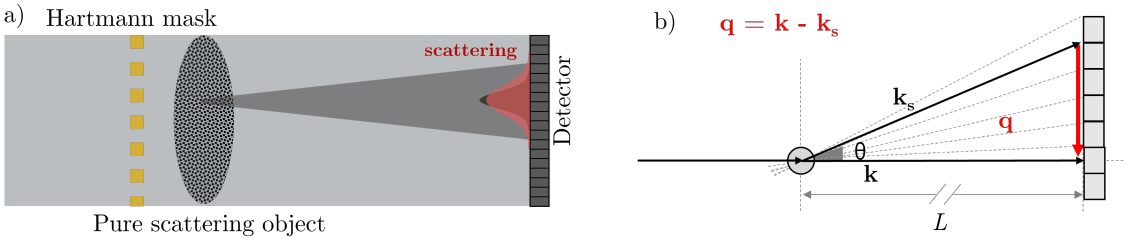

Figure 2.6: An illustration of the scattering phenomena occurring in the sample. a) Coherent scattering causes angular divergence of the beam, making the projected intensity distribution wider and decreasing the contrast in the final image. b) The ray is scattered to the scattering angle θ which reaches detector placed at distance L. The scattering vector $\boldsymbol{q}$ is the difference of wave vectors $\boldsymbol{k}$ before and after scattering. The sampling of the scattering signal is low and represented by the number of pixels per mask period.

correlation length related to the scattering vector $\vec{q}$ measured in SAXS. Such measurements can emulate the SAXS process and provide valuable structural information for large sample volumes.

Scattering intensity $I(q)$, or the differential scattering cross-section $d\sigma(q)/d\Omega$, is physically described as the number of scattered photons per unit time, unit solid angle $d\Omega$ and the unit volume dV of the sample normalized by the incident photon flux.

$$I(\boldsymbol{q}) \sim \left| \int_V f \rho_{avg} e^{i\boldsymbol{qr}} dV \right|^2, \tag{2.12}$$

where f is the atomic scattering length, ρ_{avg} average electron density. The magnitude of the scattering vector q is given by

$$q = \frac{4\pi}{\lambda} \sin(\theta/2) \approx \frac{2\pi}{\lambda}\theta, \tag{2.13}$$

where θ is a half of the scattering angle 2θ. Here we consider the small-angle scattering approximation such that $\sin(\theta) \approx \theta$.

In Figure 2.6 one can see a graphic representation of the X-ray scattering in the multimodal X-ray imaging setup with Hartmann mask, where the mask is placed before the object. Monochromatic X-rays with wave vector $\vec{k}$, where $|\vec{k}| = 2\pi/\lambda$, is incident on the scatterer. If we consider the scattering of X-rays to be elastic, then the wave vector after the scattering event is $\vec{k_s}$, such that $|\vec{k_s}| = |\vec{k}|$. The scattering vector $\vec{q}$, indicated in Figure 2.7 is the resulting scattering vector that defines the probed correlation length scale.

As mentioned above, the obtained contrast can be considered as multiple small-angle X-ray scattering measurements performed for each beamlet at once, but with poor sampling rate defined by the number of pixels per period of the modulation N_{pix}. As one can see in Figure 2.7, in such geometry the range of the scattering angles detected in the setup depends on the object-detector distance L, pixel size PS and the period P, such that

$$\theta_{max} \approx \frac{P}{L} \text{ and } \theta_{min} \approx \frac{PS}{L}. \tag{2.14}$$

Then, the range of scattering vectors is

$$q_{max} \approx 2\pi\frac{P}{\lambda L} \text{ and } q_{min} \approx 2\pi\frac{PS}{\lambda L}. \tag{2.15}$$

The correlation length for scattering imaging setup has been reported to be [31, 55]

$$\xi = \frac{\lambda L}{P}, \tag{2.16}$$

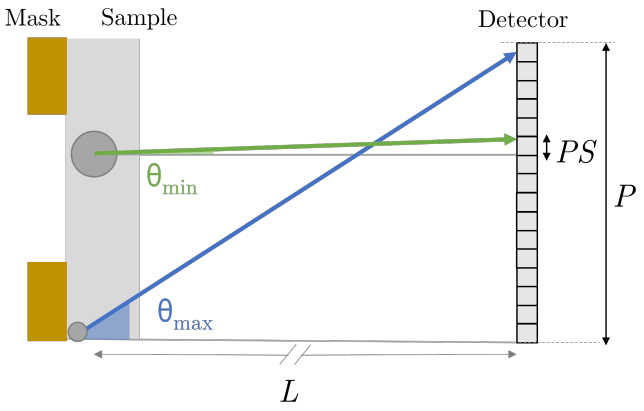

Figure 2.7: The estimation of the maximum and minimum scattering angles θ, contributing to formation of scattering contrast. The range of the angles is defined by the pixel size (PS), mask period P and propagation distance L. Note that here for generality a certain degree of transmission by gold is assumed.

which shows the relation between the maximum scattering vector and the correlation length

$$q = \frac{2\pi}{\xi}. \tag{2.17}$$

From this, one can see that ξ is equivalent to the size of the density fluctuations in the sample (the diameter of the so-called q-window). The range of the probed correlation lengths in a particular setup can be estimated as $\lambda L/P \leq \xi \leq \lambda L/PS$.

Note that for single-shot multimodal X-ray imaging, the requirement for sufficient spatial resolution of the projected mask period is $P \geq 3 \cdot PS$, as follows from the sampling theorem [56] (PS is the effective pixel size of the imaging system). Here, the plane wave is considered, but the same requirements can be formulated for the projected mask period and for cone-beam setup. However, for retrieval of scattering information in multimodal X-ray imaging a higher sampling can be preferred.

Multimodal X-ray imaging is usually performed in the near field, while typical SAXS measurement are measuring the far-field intensity distribution. The link between the scattering intensity measured in SAXS and the autocorrelation observed in the near field has been shown to be

$$\mu_d = (2\pi r_e)^2 \left[\hat{I}(r=0) - \hat{I}(r=\xi)\right], \tag{2.18}$$

where $\hat{I}$ is the Fourier transform of I [39].

2.7 Spatial Harmonic analysis

As have been shown in Section 2.6.1, the projection of the conventional and inverted Hartmann mask is a spatially periodic intensity pattern. The introduction of the object into the beam distorts the projected pattern. Discrete Fourier transformation can help to quantify the small changes introduced to the mask projection without the need for a precise alignment of the mask with the detector pixels [20, 30]. Such approach is also referred as Spatial Harmonic imaging [30, 57] or Spatial Heterodyne imaging [21]. The gist of the method is utilizing Fourier analysis and algebraic manipulations to retrieve absorption, differential phase, and scattering signals by comparing the modulated images, including the sample, to the pristine modulation (Figure 2.8).

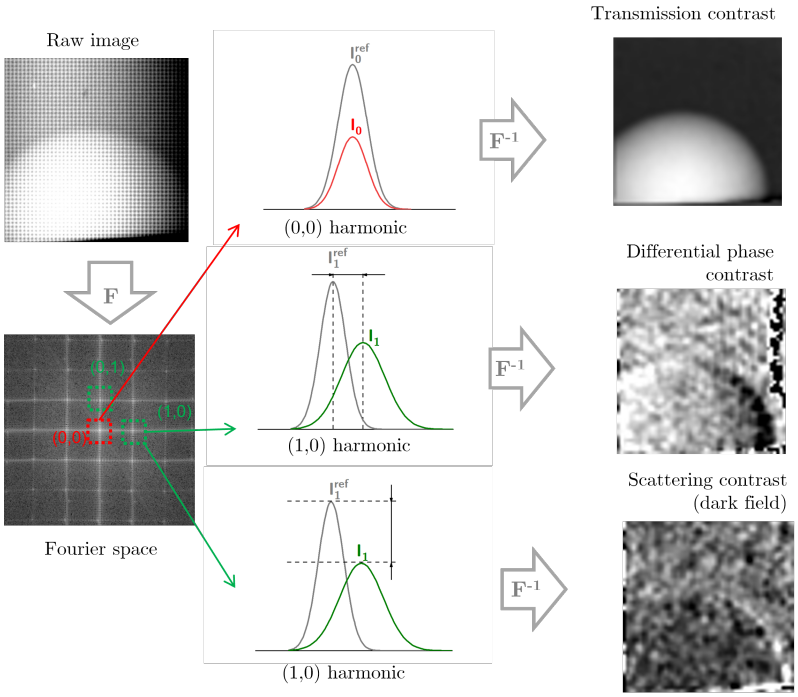

Figure 2.8: Image processing for obtaining transmission, differential phase, and scattering contrasts from a raw image of ablation bubble (see Section 4.3 of Chapter 4). The recorded projection image is Fourier transformed into the spatial frequency domain. The harmonics in the Fourier space are analyzed separately: the central (0,0) harmonic is associated with pure attenuation, and the (0,1) and (1,0) harmonics are affected by phase shift and scattering of X-rays. The regions around the harmonics are cropped and inversed Fourier transformed to obtain transmission, differential phase and scattering images. Note that phase shift and scattering is available in two perpendicular directions. F and F^{-1} indicated forward and inversed Fourier transform, respectively.

The Hartmann mask acts as a frequency modulator: it periodically samples the wavefront distorted by the sample, which results in sharp periodic peaks in the frequency domain (Figure 2.8). It is essential to record the reference projection (also called flat image) to be able to separate absorption and scattering inputs. When the mask and object overlapped projection is recorded, the periodic modulation of the mask creates a series of harmonics in the Fourier space in two dimensions. These harmonics $I_{m,n}$ are placed at coordinates $\left[\frac{2\pi m}{P}, \frac{2\pi n}{P}\right]$, where the orders m, n are integers. For illustration, Figure 2.9 shows the one-dimensional case and indicates the relative positions of the central harmonic I_0 and the first-order harmonic I_1 and how the presence of the object induced distortions might change the harmonics.

The central harmonic ($m = 0, n = 0$) contains pure attenuation signal such that the transmission contrast T can be defined as

$$T = \frac{\mathcal{F}^{-1}\{I_{0,0}\}}{\mathcal{F}^{-1}\{I_{0,0}^{ref}\}}, \tag{2.19}$$

where $\mathcal{F}^{-1}$ denotes the inverse Fast Fourier Transform of the spatial harmonic, $I_{0,0}$ is the central harmonic of the mask-object image and $I_{0,0}^{ref}$ the central harmonic of the mask-only image (reference measurement).

The phase contrast $\mathrm{d}\Phi$ is retrieved from the phase shifts of the vertical and horizontal harmonics $I_{0,1}$ and $I_{1,0}$. It can be evaluated through change in complex angle of the inverse transformed first order harmonics:

$$\mathrm{d}\Phi = \angle\mathcal{F}^{-1}\{I_{m,n}\} - \angle\mathcal{F}^{-1}\{I_{m,n}^{ref}\}, \tag{2.20}$$

where orders (m, n) are either (0,1) or (1,0).

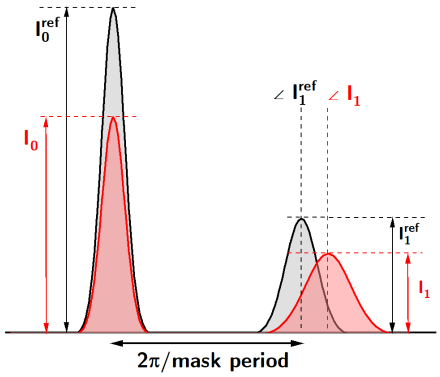

Figure 2.9: Schematic representation of how the Fourier analysis of mask projection is done and which parameters are derived. As the first order harmonic is affected by both scattering and absorption, this method always requires the reference measurement to separate absorption from scattering.

The higher-order harmonics $I_{m,n}$ contain information on both transmission and scattering and thus need to be corrected by the central harmonic image to separate scattering from the transmission. The scattering signal $S_{m,n}$ is linearized to the thickness of the sample as follows:

$$S_{m,n} = -\ln\left[\frac{\mathcal{F}^{-1}\{I_{m,n}\}/\mathcal{F}^{-1}(I_{m,n}^{ref})}{T}\right], \tag{2.21}$$

where $\mathcal{F}^{-1}$ denotes the inverse Fast Fourier Transform of the spatial harmonic $I_{m,n}$.

Usually, only the zeros and the first harmonics are analyzed to retrieve three contrast modalities in practical applications. Various sources of noise and the distortions of the wavefront by the sample influence the intensity of the harmonics in the Fourier domain; higher-order harmonics usually have a quite low signal-to-noise ratio (SNR). Setup parameters such as detector area and mask density (amount of spots created in the projection) can significantly decrease the number of harmonics with significant SNR.

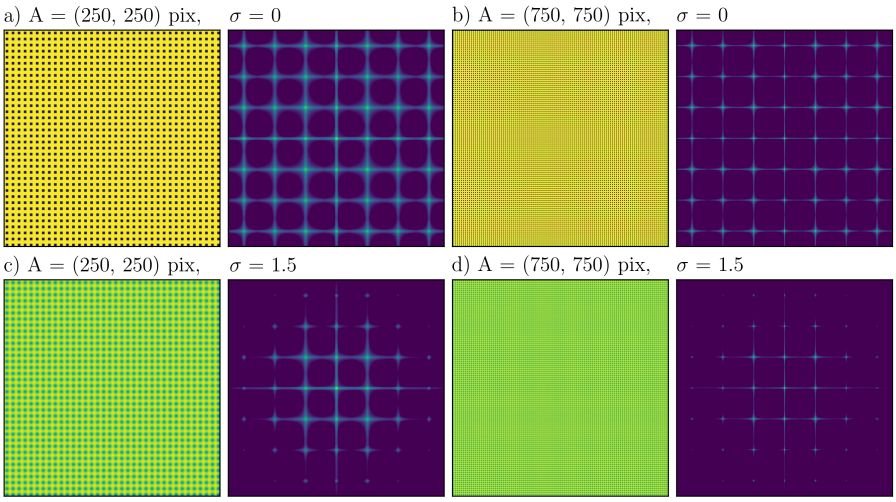

Figure 2.10: The simulated projections (HMs and iHMs) with period 25 µm and pixel size 5 µm in real and in Fourier space: a) ideal projection with detector area A = 250 x 250 pixels and standard deviation for the Gaussian filter with standard deviation for Gaussian kernel σ = 0 (no blur), b) ideal projection with detector area A = 750 x 750 pixels (no blur), c) blurred projection with detector area A = 250 x 250 pixels and standard deviation for the Gaussian filter σ = 1.5, d) blurred projection with detector area A = 750 x 750 pixels and standard deviation for the Gaussian filter σ = 1.5.

The illustration of this effect is shown in Figure 2.10, where the ideal projections for the inverted Hartmann mask are simulated (period of 25 µm and pixel size of 5 µm). With pixel size and mask period held constant, one can see how the changes in the detector area and blurring (introduced by Gaussian filter of the simulated ideal projection) can change the amplitude of the harmonics in the Fourier domain. One can see that increasing the detector area (number of spots in the region of interest, or mask density) makes the harmonics sharper and better separated (Figure 2.10a) and b)). The introduction of blur significantly lowers the signal intensity and thus, results in lower SNR. In Figure 2.10c) and d), one can see that for blur with standard deviation for Gaussian kernel $\sigma = 1.5$, the third-order harmonics are not distinguishable.

3 Development of conventional and inverted Hartmann masks

3.1 Requirements on the Hartmann masks

Although the requirements on the Hartmann mask imposed by the multimodal X-ray imaging approach are reduced compared to interferometric methods (see Chapter 2), using patterns of higher quality may increase the efficiency of sampling of Fourier spectra and simplify image processing [24]. It can also streamline other contrast retrieval algorithms and high-resolution image acquisition modes. For example, dithered acquisition mode requires the acquisition of several frames while moving the sample over the distance of a single mask period (e.g., [18, 28]). Therefore it is necessary to remove or at least reduce the number of pattern irregularities, which can influence the final image quality and lead to image artifacts.

The essential parameter which defines the final resolution of the imaging setup is the mask's period [24, 30]. A general rule of thumb is that it should be as small as possible to ensure sufficient final image resolution but large enough to meet the setup limitations (source and pixel size). As follows from the Nyquist sampling theorem [56], there should be at least three pixels per projected mask period to avoid overlapping the harmonics. However, in practice having only three pixels per mask period sometimes does not provide sufficient mask visibility for its pattern to be distinguishable in the projection image. Thus, the optimal mask period is an open question and should be addressed for a predefined setup taking into account the available X-ray camera and X-ray source, as well as the object of interest.

Different applications can impose requirements on the mask area, such as high mechanical and radiation stability of the substrate. To evaluate the mask's applicability before its testing in the imaging setup, one has to consider mask parameters that impact the wavefront modulation. Amongst those parameters are: the period of the mask, the height of absorbing structures, the transmittance of the supporting substrate, and the homogeneity of the mask structures in thickness and periodicity. The main requirements on the Hartmann mask are summarized in Table 3.1.

3.2 Wavefront modulation and mask visibility map

The sensitivity of the discussed single-shot imaging method scales with the period of the mask [20]. To sufficiently resolve the mask pattern, the camera pixel size should be equal to or less than one-third of the projected mask period [57]. The detector's resolution sets the lower limit for the mask period. To achieve the highest possible resolution within a specific setup, the use of customized masks is superior to the off-the-shelf grids. As it was reported previously [24], the masks with greater symmetry may increase the efficiency of wavefront sampling. A higher degree of periodicity of the mask structures improves the quality of the final image.

Another point to draw attention to is the profile of the mask structures. Due to the limitations imposed by the fabrication technique in use, usually, it is not a rectangular function. A possible slope of mask sidewalls

Table 3.1: Main requirements on Hartmann masks imposed by the available imaging setup and intended application.

Parameter	**Criteria**	**Requirement**
Period (P)	Final image resolution	As small as possible but at least 3 times larger than the pixel size and larger than the blur introduced by the source.
	Probed correlation length ξ (scattering contrast)	Should provide projected pattern of required period according to $\xi = \lambda L/P$, where λ is the wavelength and L is the distance from the detector to the mask or the object (depending on the setup organization).
Height of absorbing structures	X-ray energy	The structures should be tall enough to absorb at least 50 % of incident radiation and produce a distinct radiation pattern on the detector. For cone beam setups, one should keep in mind shadowing artefacts.
Substrate	X-ray energy, required mechanical stability of the mask	The substrate should transmit sufficient amount of radiation for projected mask pattern to be distinct (depends on a beam intensity provided by the source).
Mask area	Required field of view (sample size or the region of interest)	Should be sufficiently large to cover the object area (or region of interest).

can introduce different absorption levels resulting in a blurring of the image, in addition to the blurring by the X-ray tube focal spot size and point spread function of the camera. Thus, improving the mask's periodicity and shape can enhance the quality of the final image and possibly diminish the X-ray tube and camera requirements.

Particular attention should be paid to the parameters impacting the wavefront modulation (WFM) introduced by the mask. Here, by the efficiency of wavefront modulation (WFM), we mean the intensity variation between opaque and transparent mask areas. In an ideal case, the absorbing structures should stop 100 % of incident X-ray radiation. The supporting carrier (substrate) has complete transparency for the wavelengths of interest (thus, it has an absorption of 0 % at the typical energy range of 10-60 keV). The pattern should be regular within the whole mask area.

The efficiency of wavefront modulation is a characteristic that directly influences the contrast of the image acquired by the detector. It can be expressed similarly to the visibility characteristic used in the interferometric methods [58]:

$$WFM = \frac{I_t - I_{op}}{I_t + I_{op}}, \tag{3.1}$$

where I_t – intensity, transmitted by the transparent structure, I_{op} – intensity, transmitted by the opaque structure. The difference of WFM to the visibility characteristic used in imaging is that WFM is a theoretical value and represents the ideal (absolute maximum) value of visibility, which can be achieved with the mask. WFM can be estimated for the mask before its testing in the setup, only knowing the X-ray energy to be used, the materials of the mask and their thicknesses.

It is important to note that the values of I_t and I_{op} vary significantly with X-ray energy; the same mask will perform differently at the different radiation energy. Moreover, as conventional sources, such as X-ray tubes,

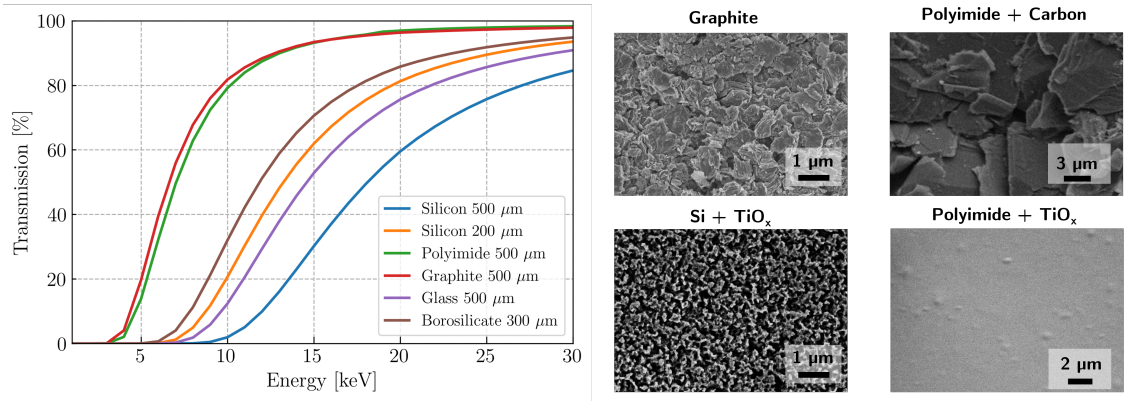

Figure 3.1: X-ray transmission of typical substrate materials and SEM images of sufraces of some of the possible substrates.

are not monochromatic and emit energy in a certain spectrum, the ideal case of WFM = 1 is not possible to attain in reality. Single-shot X-ray imaging has been demonstrated even with $WFM < 0.5$ [59, 60]; however, increasing efficiency of wavefront sampling can enhance the quality of the final image.

Different periodic structures have already been used before for single-shot imaging applications such as various commercially available metal meshes: Bucky grid (lead and aluminum) [22], Nickel wire mesh [19, 20] and stainless steel mesh [17], tungsten plates with holes made by laser ablation [18]. There were examples where the gold mask pattern of 30 µm height electroplated on 100 µm glass substrate to be utilized at the energy of 50 keV for subpixel resolution analysis of intensity distribution [25]. Gold absorbs X-rays much more efficiently than nickel, stainless steel, or even tungsten. Still, the height of 30 µm only stops about 35 % of incident radiation, leading to the WFM of about 0.2. This results in the decreased contrast of the final images. Thus it is always advantageous to have higher gold structures for such X-ray energies.

The same can happen if the substrate in use is highly absorbing at the utilized energy range. For example, widely used conventional silicon substrates with 500 µm thickness have low transmission at the energy range from 1 to 15 keV (Figure 3.1). For excellent imaging quality at these energies, it is crucial to choose more X-ray transparent substrates composed of low atomic number materials, for example, polyimide and graphite. However, the choice of the substrate is not solely based on the high X-ray transmission value but also its mechanical, thermal, structural, chemical, electrical, and even biological properties such as toxicity.

The relative value of wavefront modulation can serve as a benchmarking measure for a particular mask with the defined source and detector setup. To explore the possibilities of the single-shot imaging approach, one should achieve the highest wavefront modulation keeping a high degree of periodicity for the masks in use. In this regard, this work aims to develop high-quality Hartmann masks of various periods for customized materials science and medical applications at energies up to 25 keV, both for imaging with synchrotron radiation and a laboratory X-ray tube.

3.3 Fabrication with UV lithography

UV lithography is one of the most available and widely used microstructure fabrication techniques to pattern periodic structures over a large area. It can provide Hartmann masks with high quality if the technological process is optimized for the required structure size regarding the diffraction limit of the resolution [61]. Each step of the manufacturing process requires optimization to eliminate the distortions of the predetermined pattern due to various phenomena, but greater attention must be paid to the fine-tuning of the exposure dose, which is directly related to the number of cross-linking reactions occurring in the photopolymer (photoresist)

layer. Cross-linked areas form an intended pattern shape, which is subsequently used to serve as a mask for electroforming. Properties of the pattern, such as mechanical stability, homogeneity, and uniformity of the design (height and periodicity), directly depend on photoresist performance during and after exposure. In the case of the negative photoresist, the exposure dose should be high enough to generate the cross-linking along with the photoresist depth sufficient to adhere it to the substrate carrier and to avoid structure deflection followed by the pattern collapse due to insufficient stiffness. Overexposure, in its turn, can result in significant distortion of the pattern shape due to diffusion of the photoactive components. Furthermore, overexposure can lead to cracking of the cross-linked areas due to photoresist shrinkage. Photoresist sensitivity curves can help with the optimization of exposure dose and characterization of photoresist response to irradiation.

Various substrates can be used for patterning structures with UV lithography (e.g., the substrates materials shown in Figure 3.1). The standard substrate material used in UV lithography is silicon. For that reason the first Hartmann masks were fabricated using silicon substrate with TiOx coating, as it ensures high adhesion of photoresist and provides a conductive layer for electroplating of high-absorbing structures like gold. The processing steps were further adapted for the fabrication of Hartmann masks on graphite substrate, which is more challenging due to the porous structure of graphite, as will be addressed later in this chapter.

3.3.1 Sensitivity curve for photoresist

The proper exposure parameters were determined using the sensitivity (contrast) curve procedure, which assesses the lithographic performance of photoresist [58]. A set of samples was prepared to carry out a sensitivity curve procedure to determine the proper exposure parameters. A thin (few nm) layer of hexamethyldisilazane was deposited on silicon wafers with a thickness of 525 µm during substrate pretreat with heating up to 150 °C for 30 minutes to increase the adhesion of the photoresist to the wafer. Using different regimes to achieve layer thicknesses of 10 µm, 15 µm, and 20 µm, the epoxy-based negative mr-X 10 photoresist (micro resist technology GmbH, Berlin) was spin-coated on the wafers. Thicknesses higher than 20 µm were not used for sensitivity curve procedure, as in this case, the dose is not uniformly distributed along with the photoresist thickness due to absorption; the ratio of bottom and the top dose is not close to unity, which violates the basic assumption of the approach [58].

The soft bake was performed using a hot plate at the temperature of 95 °C for 10 minutes. Exposure was carried out with a mercury UV lamp. The total incident radiation power stability and distribution were controlled by Karl Suss UV intensity meter model 1000. The intensity value was 15 mW/cm^2 with 1 mW/cm^2 deviation from the center to the edge, the measurements were performed for i-line of the mercury spectrum (λ = 365 nm). The exposure was done using double mask geometry: the lower mask was a Cr-Quartz mask with alternating dark and light tone regions with a pattern of structure sizes from 2 up to 50 µm; the upper mask was a slit that allowed dividing the exposure area into 15 sectors which received different dose with a constant step. The dose was tuned within a determined range by changing the exposure time. The exposure was carried out using vacuum contact alignment to eliminate diffraction effects: the wafer and the mask were placed in the vacuum chamber to ensure the absence of a gap between the mask and the photoresist layer.

The exposed samples were subjected to post-exposure bake (PEB) in the oven for 4 hours with the temperature changing from 70 up to 90 °C and subsequent cooling down to room temperature. A wet development of the exposed photoresist layers was carried out in propylene glycol monomethyl ether acetate in order to dissolve the unexposed area of mr-X 10 photoresist layers, and then the samples were rinsed in isopropanol alcohol. After development, the samples were air-dried in a convection oven at 30 °C, and then the height of the

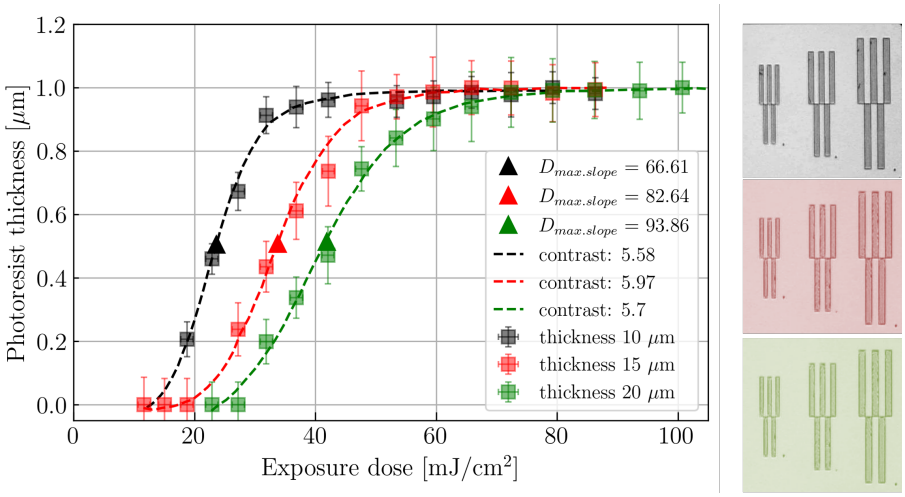

Figure 3.2: Sensitivity curves obtained for mr-X 10 photoresist layers of thickness: 10 µm (black), 15 µm (red), 20 µm (green) and respective colored patterns overview for 10 µm (gray), 15 µm (red) and 20 µm (green). The curves were plotted using the approach reported in [58]. In the figure, contrast values for different curves are defined according to Eq. 3.2. Dose at the maximum slope serves as a quantitative value for a comparison of curves shift.

formed micropattern was measured with a long scan profiler Tencor P-2 with an instrumental accuracy of 25 Å.

The results of the sensitivity curve measurements, which describe the remaining photoresist fraction as a logarithm function of applied exposure dose, are shown in Figure 3.2. To approximate the data, we used a generalized logistic function fit according to the approach reported previously [58]. As one can see, the sensitivity curves for 15 and 20 µm photoresist layers are shifted towards higher exposure doses. This is due to the absorption introduced by the photoresist layer, which decreases the delivered bottom dose. All curves exhibited a similar slope, which can be associated with photoresist contrast. The contrast value is defined by

$$\gamma = \left[\log_{10}\left(\frac{D_2}{D_1}\right)\right]^{-1} \tag{3.2}$$

where D_1 is the dose for which the remaining photoresist height is 10 % of the original value, and D_2 is the dose for which the remaining photoresist height is 90 % of the original value. The value of the contrast generally represents the response of the photoresist to radiation [58]. From the fabrication point of view, the most valuable information for a given patterning photoresist material is the optimal dose. By optimal dose, we mean the value that is sufficient to obtain a full cross-link of the photoresist. Optimal values were estimated from the sensitivity curve plateau, taking into account the pattern quality evaluated with an optical microscope Figure 3.2. Defect-free patterns were obtained at optimal dose value, which also confirmed properly adjusted PEB and development time conditions. As it was noted previously, the thicknesses higher than 20 µm could not be subjected to sensitivity curve procedure; thus, the optimal values for such thicknesses were extrapolated from the data for lower thicknesses.

3.3.2 Masks on silicon

UV LIGA for the manufacturing of Hartmann masks was carried out using the process chain similar to the contrast curve samples preparation but with several application-related changes. The main overview of the process is shown in Figure 3.3. Thinner silicon wafers were used for mask fabrication in order to achieve

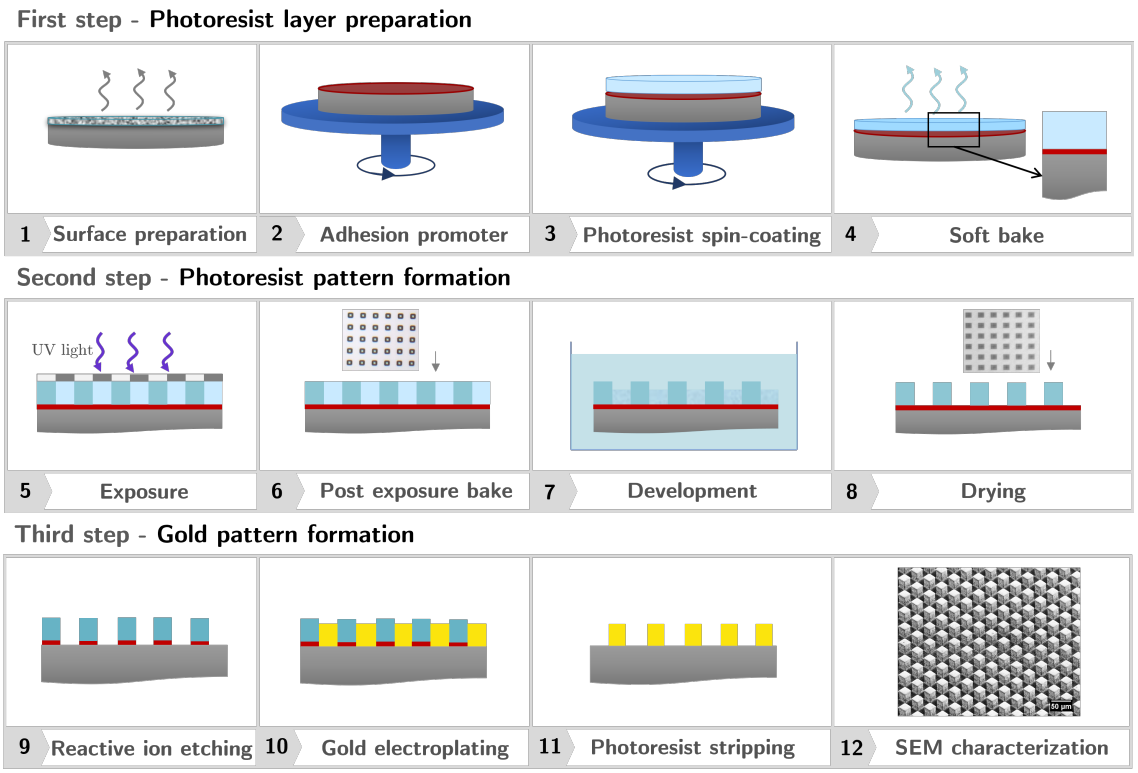

Figure 3.3: Fabrication process steps of UV LIGA: substrate preparation consisting of cleaning of the surface and applying the photoresist; photoresist pattern formation with exposure and development; gold pattern formation by electroplating and stripping of the photoresist.

higher wavefront modulation. The substrates were 200 µm silicon wafers with few nanometers of Ti and TiOx to create a conductive contact layer for the concluding electroplating.

1. Photoresist layer preparation.

Substrate cleaning was performed to guarantee that it was free of impurities and moisture. Oxygen plasma cleaning was employed with subsequent baking at 120 °C and cooling down to room temperature immediately before coating. Spin-coating of TI PRIME adhesion promoter was performed before photoresist application. After solvent evaporation, TI PRIME forms a physically bonded sub-monolayer of the active compound. A subsequent baking step of the primed substrate at 120 °C chemically activated the adhesion promoter, thus creating the desired hydrophobic surface allowing subsequent photoresist coating with improved wetting and adhesion between the TiOx and the photoresist. Immediately after the primed substrate baking was finished, spin-coating of negative mr-X 10 photoresist was performed to achieve layers of 10 µm, 20 µm, 30 µm, and 40 µm thickness. A soft bake to remove the solvent content from the sample was carried out at 95 °C on the hot plates for time periods from 10 to 20 minutes, depending on the photoresist layer thickness.

2. Photoresist pattern formation.

The exposure of photoresist layers was performed using EVG mask aligner with 2.85 mW/cm^2 radiation intensity (0.15 mW/cm^2 deviation) using the filter for wavelengths shorter than 365 nm. The photomask for exposure was a 5-inch Cr-Quartz mask purchased from Compugraphics (Jena, Germany) with four regions of different periods and shapes; the area of each region was 1 cm^2. The exposure was carried out with soft contact mode (no vacuum) to prevent the photoresist layer from sticking to the mask. The exposure dose values are listed in Table 3.2. Theoretically, the optimal dose depends on the photoresist thickness, solvent, UV sensitivity, absorption in the exposure spectrum, power, and coherence of the UV lamp. For fabrication

Table 3.2: Main characteristics of the masks fabricated on silicon substrate.

PR thickness (μm)	**Mask period** (μm)	**Shape**	**Dose** (mJ/cm^2)	**Gold thickness** (μm)
10	50	square	550	5
10	25	square	550	5
10	10	square	550	5
10	50	round	550	5
20	50	square	610	15
20	25	square	610	15
20	10	square	610	9
20	50	round	610	15
30	50	square	630	22
30	25	square	630	22
30	10	square	630	(-)[1]
30	50	round	630	22
40	50	square	650	28
40	25	square	650	28
40	10	square	650	(-)[1]
40	50	round	650	28

[1] No structures

purposes, the initial exposure dose range was empirically estimated using the data from sensitivity curve method (see Section 3.3.1). Then, the exposure parameters were adjusted taking into account the difference in the radiation intensity for the used UV lamps. The final optimal dose was defined by evaluating the quality of the pattern achieved for different doses.

Post-exposure bake and development steps were the same as for the contrast curve sample set. Development times were adjusted according to the thickness of the photoresist layer. Optical microscope images of the gratings were obtained to perform a preliminary quality assessment of periodicity and homogeneity of the pattern. A sharp definition of the structures and a high degree of periodicity was observed for all periods for photoresist thickness up to 20 µm. However, for a photoresist thickness of 30 µm and thicker, structures with a period of 10 µm undergo undesirable crosslinking caused by the diffraction effect, which made square structures appear round. This resulted in structure size loss, as the final structures were electroplated using a structured photoresist layer as a mask for the conductive wafer surface.

Gold pattern formation.

The photoresist mask formed by means of UV lithography was filled with gold in an electroforming step after development. Electroplating current density and voltage were fixed, and duration time defines the amount of gold that should be plated on the wafer. This amount of gold was determined by the height of designed structures, which is usually 75 % - 80 % of photoresist layer thickness, and the area that should be electroplated. Gold electroforming was performed using a standard gold-sulfite electroplating bath for microstructures fabrication at the temperature of 55 °C. After electroplating, the photoresist was stripped using oxygen plasma.

The manufactured masks and their main characteristics are listed in Table 3.2. Each mask has an area of 1 cm x 1 cm. However, larger areas (up to 5 cm x 5 cm) can be obtained within the same process chain if a larger Cr-Quartz exposure mask layout is used.

3.3.3 Masks on graphite

Another type of a promising substrate material for Hartmann masks is low-absorbing graphite substrates, which can also be used for UV lithography. Graphite enables an excellent adhesion of the mask features to the substrate. Due to better adhesion graphite is well suited for fabrication of both arrays of gold pillars (inverted Hartmann masks) and gold meshes (Hartmann masks). The conventional Hartmann mask design requires the formation of an array of photoresist pillars, which are then used to create the gold mesh after electroplating. The photoresist than is stripped away, and the resulting mask is an array of holes in gold layer.

Table 3.3: Processing steps and parameters for graphite mask patterning with UV lithography and gold electroplating.

Processing step	**Parameters**
Cleaning	rinsing with distilled water and drying at 200 °C for 5 min
Preprocessing	soaking with photoresist
Spin-coating	Spinning time - Acceleration - Spin speed 30 sec - 300 rpm/s - 500 rpm* 60 sec - 1500 rpm/s - 0 rpm 60 sec - 300 rpm/s - 1900 rpm
Soft bake	30 min at 90 °C
Photoresist thickness control	36 µm
UV exposure	650 mJ/cm^2
Post Exposure Bake	temperature changing from 70 °C to 90 °C for 4 hours and subsequent cooling to room temperature
Development	wet development with PGMEA
Gold electroplating	gold-sulfite electroplating bath at a temperature of 55 °C

The lithography-based fabrication process, like for the masks on silicon, consisted of several sequential steps: photoresist spin-coating, exposure, post-exposure bake, development, and gold electroplating. The process starts with the photoresist layer application. In our case, it was a SU-8 based, chemically amplified negative photoresist mr-L 50 (micro resist technology GmbH, Berlin, Germany). Spin-coating of a liquid photoresist is challenging due to the penetration of photopolymer into the pores of the graphite. To ensure a homogeneous photoresist layer on top of the wafer, we preprocessed the wafers by soaking them with photoresist before the spin-coating. After photoresist spin-coating, the layer was exposed to i-line UV light using a Cr mask. Due to the photosensitivity of the photoresist, UV exposure initiates a cross-linking process in the photoresist, resulting in a solid pattern. The processing steps are summarized in Table 3.3.

The final structures were two-dimensional arrays with an area of 1 cm^2. The area was scaled up to 5 cm x 5 cm within the same fabrication approach for the inverted Hartmann mask with 50 µm period. The periods of the 1 cm x 1 cm masks were 30, 40, 60, and 80 µm. The thickness of the gold (pillars or meshes) was 30 µm for all masks.

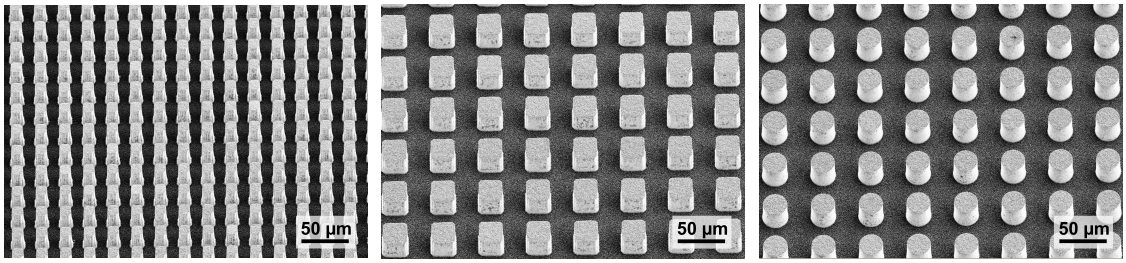

(a) P = 25 µm **(b)** P = 50 µm **(c)** P = 50 µm

Figure 3.4: SEM overview images of the inverted Hartmann masks with 28 µm gold height: (a) 25 µm period pattern; (b) 50 µm period square shape pattern; (c) 50 µm period round shape pattern.

3.4 Characterization and quality assessment

3.4.1 Masks on silicon

The mask quality evaluation was first performed with optical and scanning electron microscopes (Figure 3.4 and Figure 3.5). The main quality control points were the uniformity of the mask pattern, the sharpness of structures edges, sidewalls geometry, and quantitative characterization of mask height, period, and duty cycle. The duty cycle (DC) in grating fabrication represents the ratio of the structure width to the period of the pattern. For the gold height from 5 µm to 15 µm, it was possible to obtain reproducible structures with periods down to 10 µm; however, the shape of the structures was affected by diffraction in the corners of the square pillars. For gold structures higher than 20 µm, the electroplating of structures with a period of 10 µm was not possible due to excessive cross-linking of the photoresist and significant distortion of the initial pattern shape.

An example of the inverted Hartmann mask of 25 µm period and 28 µm gold height with stripped photoresist is shown in Figure 3.4(a). One can see that the mask pattern is clear and uniform; no structures are collapsed or detached. Each pillar of the mask is wider at the bottom and smaller on the top (Figure 3.5(a)), which is due to the interplay of a negative photoresist response, absorption, and diffraction effects occurring in the UV lithography. The duty cycle of the mask at the top and on the bottom is slightly different from the intended value. Analysis of SEM images has shown that for the top of the mask, the duty cycle is 0.47 and for the bottom 0.58. Thus, the average duty cycle is 0.52 ± 0.05. It is important to note that the analyzed mask is with the highest aspect ratio (height 28 µm, structure size 12.5 µm) among fabricated masks with sufficient quality; the distortions observed for such structures are much less for the other fabricated masks. From the application side, such a distorted sidewall shape of the structures might slightly decrease the efficiency of wavefront modulation. Still, on the other hand, it provides structures with additional mechanical stability. The granular surface of the structures (see Figure 3.5) does not affect significantly the quality of the wavefront modulation, as associated deviations in the height are very small and the masks are to be used as absorption masks with minimal gold transmission.

As mentioned before, different shapes of the structures were tested to compare their final quality. The inverted Hartmann masks of the 50 µm period and 28 µm gold heights are presented in Figure 3.4(b-c). As one can see, the mask patterns of both shapes are precise and uniform, the structures are well-defined and exhibit a high degree of periodicity. Single pillars of the square and round shapes are shown in Figure 3.5 (b-c). Both have a broader foundation and narrower top, but the deviation is smaller than the one presented in Figure 3.4(a). For the square pillars, the top duty cycle is 0.49, and the bottom DC is 0.53, which gives the average DC = 0.51 ± 0.02. For the round pillar, the top duty cycle is 0.50 and for the bottom is 0.52, which gives the average DC = 0.51 ± 0.02. The variation of the top and bottom sizes of the pillars is different for

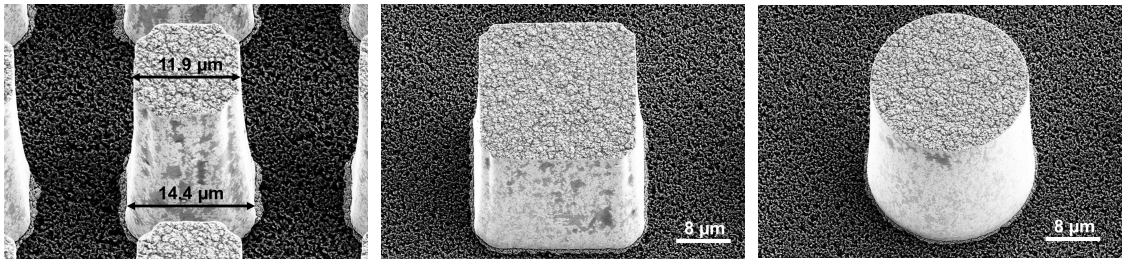

(a) P = 25 µm **(b)** P = 50 µm **(c)** P = 50 µm

Figure 3.5: Close-up SEM images of the inverted Hartmann masks of 28 µm gold height: (a) the square shape mask of 25 µm period; (b) the square shape mask of 50 µm period; (c) round shape pillar of 50 µm period.

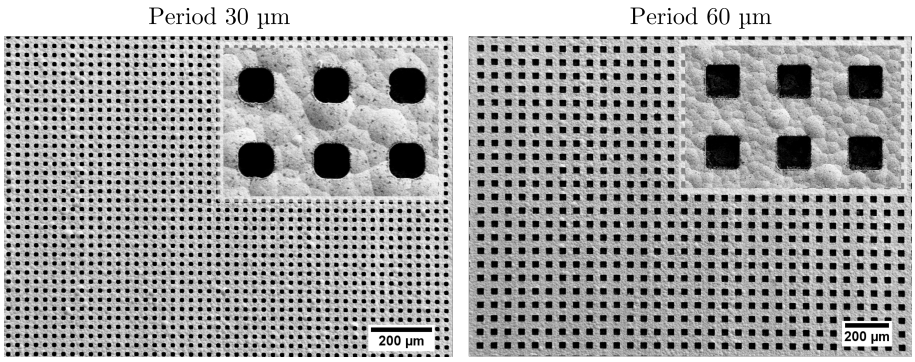

Figure 3.6: SEM images of Hartmann masks of period 30 µm (a) and 60 µm (b). Gray areas are gold and black areas are wholes.

square and round shapes, but the average duty cycle remains the same. No period variation was observed in the SEM images. The values of DC for square and round structures imply that one can profit from the decreased influence of diffraction in the patterning of round structures for smaller periods.

3.4.2 Masks on graphite

The SEM images of two Hartmann masks of period 30 µm and 60 µm made on graphite are illustrated in Figure 3.6. The patterns are clear and periodic, none of the array of holes in gold is closed. It means that the array of the photoresist pillars formed on graphite had good adhesion and every pillar stayed intact. Note that the shape of the mask with smaller period in Figure 3.6(a) is rounded due to the diffraction effects occurring during UV exposure; the initial pattern design was intended to be square-shaped. However, this does not change the approach for data analysis as the key feature of the mask is periodicity. As one can see

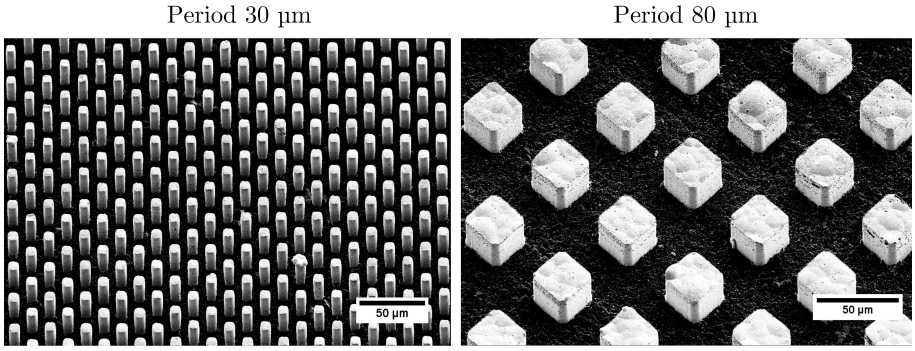

Figure 3.7: SEM images of inverted Hartmann masks of period 30 µm (a) and 80 µm (b). Gray areas are gold.

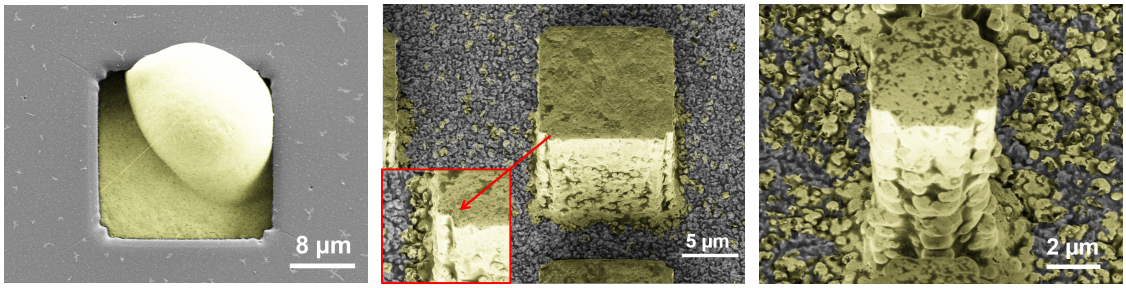

(a) overplating **(b)** diffraction **(c)** impurity

Figure 3.8: SEM images of the inverted Hartmann masks chosen to test the robustness of the characterization algorithm by radiographic projection analysis: (a) the illustration of the gold overplating (mask before photoresist stripping); (b) illustration of pattern impurity and shape distortion caused by diffraction limit; (c) large particle formation during electroplating.

in the inset in Figure 3.6, the surface of the gold is rough, which could be due to the inherent roughness of the graphite substrate.

An example of the inverted Hartmann masks of period 30 µm and 80 µm is shown in Figure 3.7. The pillars of gold are regularly spaced, and the patterns are clear from impurities. In general, all obtained masks exhibit regularity of the pattern, high periodicity, and the absence of substantial defects. For the inverted Hartmann patterns of smaller periods, a partial collapse of the structures was observed at the edge of the mask after mask handling. However, it does not affect the quality of the final images as this area is usually out of the field of view of the imaging setup. Slight deviations of the gold height have been found in SEM images, but they did not exceed 2 µm. Such variations will not substantially influence the image quality if the mask is utilized at the appropriate X-ray energy (such that the absorber height of the mask is sufficient to stop about 80% of the radiation).

3.5 Mask performance in a radiographic setup

3.5.1 Masks on silicon

We tested the developed inverted Hartmann masks using a radiographic setup at TOPO-TOMO beamline of the Karlsruhe synchrotron radiation facility (Karlsruhe, Germany). The measurements were performed at the energy of 8.5 keV utilizing an optical system to introduce 9x effective magnification. The detector was a Camera Andor Neo sCMOS with an effective pixel size of 0.72 µm and a field of view of 2560 x 2140 pixels. The mask was placed at 8 cm from the detector. The tested masks were gold square pillars of 15 µm height with 10 µm, 25 µm, 50 µm periods in both vertical and horizontal directions, manufactured on the same 200-µm-thick silicon substrate with an oxidized titanium layer. The average WFM introduced by the masks according to the Eq. 3.1 was 0.88.

The robustness of the analysis algorithm was tested by the masks with several technologically-driven defects, which imposed challenges to the data interpretation. We intended to explore the possibility of decoupling typical fabrication issues using the data obtained from the projection image. The specimen has several defects in the photoresist pattern due to the local adhesion issues, which were eliminated for other specimens by careful cleaning. As a consequence, the final pattern suffered from the overplating of gold on top of the photoresist layer as shown in Figure 3.8(a), diffraction-induced shape distortion as represented in Figure 3.8(b), the impurity of the inter-structure areas and particle formation during electroplating, which can be seen in Figure 3.8(c).

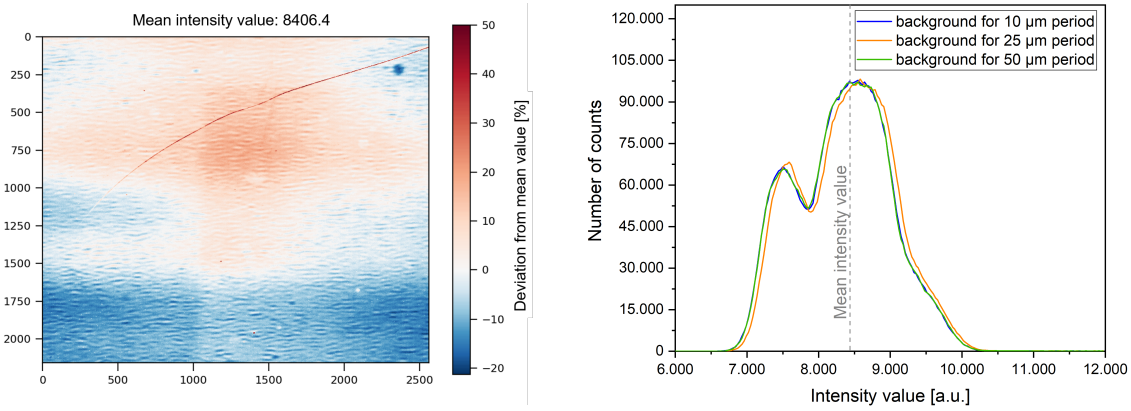

(a) flat-field

(b) recorded intensity

Figure 3.9: Radiographic image analysis: (a) flat-field image illustrating the deviation from the mean intensity value for the background; (b) illustration of the detector signal (recorded intensity) splitting in two Gaussians.

Radiographic images were obtained with only the masks in the beam path. The fragments of the images are shown in Figure 3.10. Flat-field images without the masks were obtained to correct the resulting image considering the beam shape and estimated detector noise. The exposure time for all acquired images was the same. As one can see in Figure 3.9, there is a strong deviation of the background from the mean value.

Moreover, it has a highly inhomogeneous distribution over the whole detector area. The detector signal (recorded intensity) was composed of two Gaussians as shown in Figure 3.9(b), which means that the illuminated detector area has two main intensity values (around 7500 a.u. and 8500 a.u.). The mean value for the whole distribution was around 8400 a.u. Such an effect could be either due to a non-uniform beam or detector response. Special attention was paid to the normalization of the data due to the inhomogeneity of the background. For each mask projection, the respective flat-field image was subtracted from the data, and further correction by the absorption of the substrate was applied.

Relative absorption signal histograms (i.e., the number of counts associated with a certain absorption level) were plotted, applying 3 x 3 median filters for pixel-noise removal to characterize the intensity modulation introduced by the masks qualitatively. As one can see in Figure 3.10, the intensity distribution peaks for masks of periods 50 µm and 25 µm are clearly separated. However, the absorption signal peak splits around 400 a.u. for the 25 µm period mask and around 430 a.u. for the 50 µm period mask. For a 10 µm period, there was no clear separation of peaks observed, but somewhat overlapping of at least three Gaussians centered at 0 a.u., 110 a.u., and 250 a.u. By comparing quantitative data about the height of gold structures obtained from the SEM images with absorption signal distributions, one can correlate the height of gold with the respective peak on the histogram.

A local effect present at the characterized masks is pattern impurity due to partial gold deposition between the structures, leading to a decrease in transmission, thus reducing the intensity and additional broadening of the zero-centered peak. Decomposition of real data histogram profiles into several Gaussian-shaped signals has been performed. Examples for 10 µm and 50 µm period masks are shown in Figure 3.11. It is evident in Figure 3.11a) that an additional contribution of the signal at approximately 30 a.u. is present corresponding to the gold height of about 1 µm. This signal is attributed to the impurity of the pattern and contributed to the broadening of the zero-centered peak. The impurity of the pattern for the tested mask might be due to a slight undercut of the photoresist layer during reactive ion etching before electroplating. The effect was more substantial for smaller periods, as observed with SEM (Figure 3.8(b-c)); in this case, the gold nucleation points were placed closer to each other, and undesirable diffusion of Au+ between the structures in the undercut area occurred. In its turn, the contrast between absorbing and non-absorbing areas on the projected

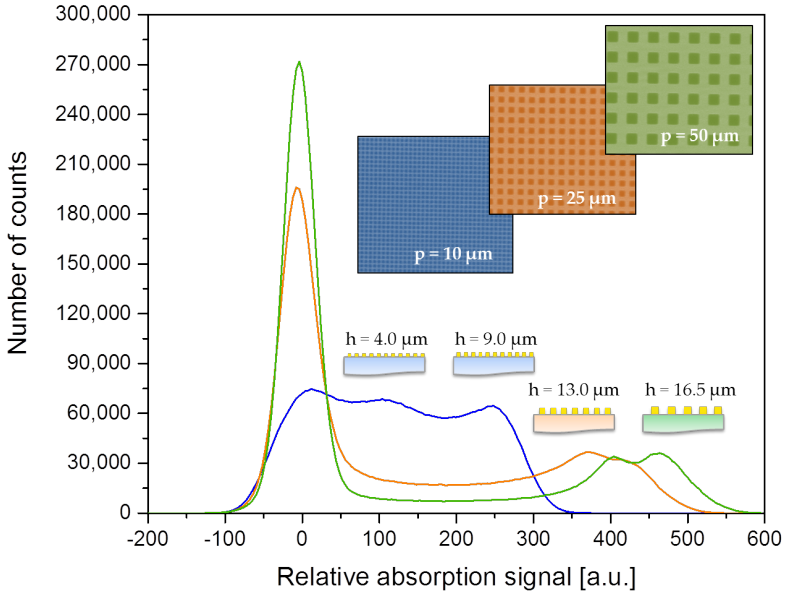

Figure 3.10: Histogram of the relative absorption signal after subtraction of the background with cropped radiographic projection images for 10 µm (blue), 25 µm (orange), and 50 µm (green) period square structures for visual representation.

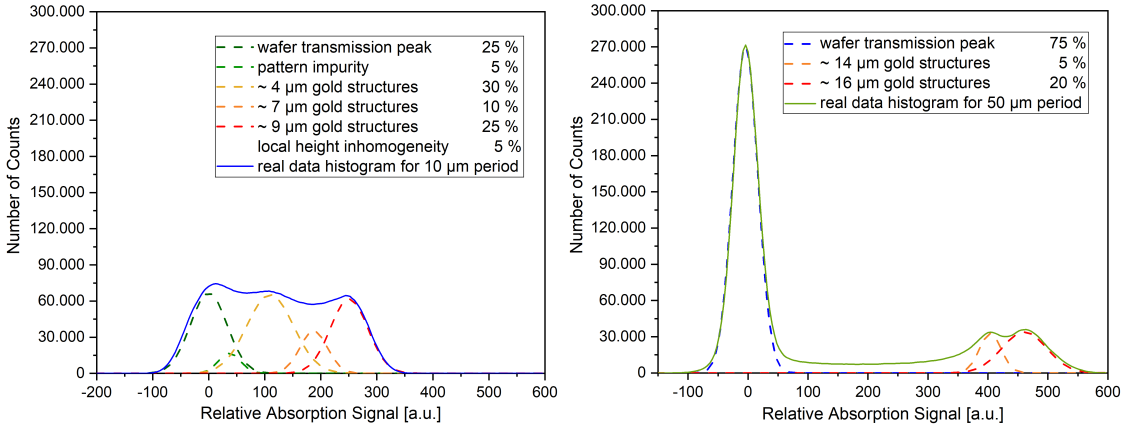

(a) P = 10 µm **(b)** P = 50 µm

Figure 3.11: Real data absorption signal histogram decomposed into several Gaussian shape signals correlated to the different height of gold structures: (a) for a 10 µm period mask (small Gaussians were treated as a local gold height inhomogeneity as their content in the entire profile was less than 2 % each); and (b) for a 50 µm period mask. In the legends the percentage of the contribution to the signal was calculated from the areas of the Gaussians used for the approximation of the real data profiles.

images was decreased by this effect strongly for smaller periods. For example, for the 10 µm period mask, the highest pillars were about 9 µm (see the pillar in Figure 3.8(c)); thus, approximately 5 % of radiation was transmitted through such structures, and the transmission of the wafer carrier was reduced by the impurities of the pattern, resulting in a decreased intensity modulation.

However, not only impurities contributed to the overlapping of the peaks on the histogram for a 10 µm period. As it was mentioned above, there is a third Gaussian centered at approximately 110 a.u (yellow dashed line in Figure 3.11(a)), which can be correlated with the gold height of about 4 µm using information obtained with SEM. This implies that gold height is not homogeneous, and pillars of different heights were obtained during the electroplating. However, for a 50 µm period mask, the intensity modulation was highly efficient, resulting in clearly separated signals from gold structures and the transparent areas with a ratio of 1:3. Nonetheless, a splitting of the signal in two Gaussians is present, attributing to 14 µm and 16 µm height. Another defect that could cause changes in the distribution of the absorption signal is the diffraction-caused shape distortion, which is prevailing for the 10 µm period mask. This effect can be diminished by using a circular-shaped mask for UV lithography, as such a shape is less sensitive to diffraction effects.

3.5.2 Masks on graphite

Conventional and inverted Hartmann masks were tested at the TOPO-TOMO beamline of the IPS imaging cluster of the KIT synchrotron facility. A quasi-monochromatic beam with the energy of 17 keV with a bandwidth of 2% was used for the measurements. Detection of the X-rays was performed by the Andor Neo 5.5 X-ray camera coupled with lenses (magnification of 2.73) to achieve an effective pixel size of 2.4 µm. X-rays were incident on the Hartmann (or inverted Hartmann) mask, which was placed on a stage 9.5 cm away from the detector.

The relative absorption histogram analysis was performed for the acquired projections of masks. In Figure 3.12(a), one can see the histograms for the conventional Hartmann masks with periods 60 and 80 (HM60 and HM80). The histograms exhibit three peaks: zero centered peak corresponding to the intensity transmitted by the substrate (holes in the mask) and the highest peak at the relative absorption level of 350 a.u. Two other peaks are located at the relative absorption levels of 210 and 270 a.u. The peaks locations are the same for both masks, which indicates the inhomogeneous gold mesh thickness formed during electroplating. Assuming that the highest peak corresponds to the intended gold height of 30 µm, the additional peaks are coming from the gold thicknesses of about 18 and 23 µm.

Figure 3.12(b) shows the histograms for the inverted masks (iHM60 and iHM80). The histograms have a big zero-centered peak which indicates the counts of transmitted intensity by the graphite substrate. The peak corresponding to the gold height is located at about 390 a.u. for iHM60 and at 430 a.u. for iHM80. The peaks are not as clearly separated as for the masks on silicon (see Figure 3.10). It can be due to the scattering introduced by the graphite substrates, which results in a stronger blurring of the mask projection.

3.5.3 Simulations

To understand the data obtained from the measurements and evaluate the quality of the microstructure patterns over a large area, we correlated mask defects and flaws with respective projection image distortions for the inverted Hartmann masks made on silicon substrate. The ideal data arrays were simulated in order to investigate possible generalized imperfections of the mask and its alignment in the setup. The arrays had dimensions and intensity (counts) corresponding to the actual projections acquired with the inverted Hartmann masks on silicon with periods 10, 25, and 50 µm. The changes such as rotation and blurring

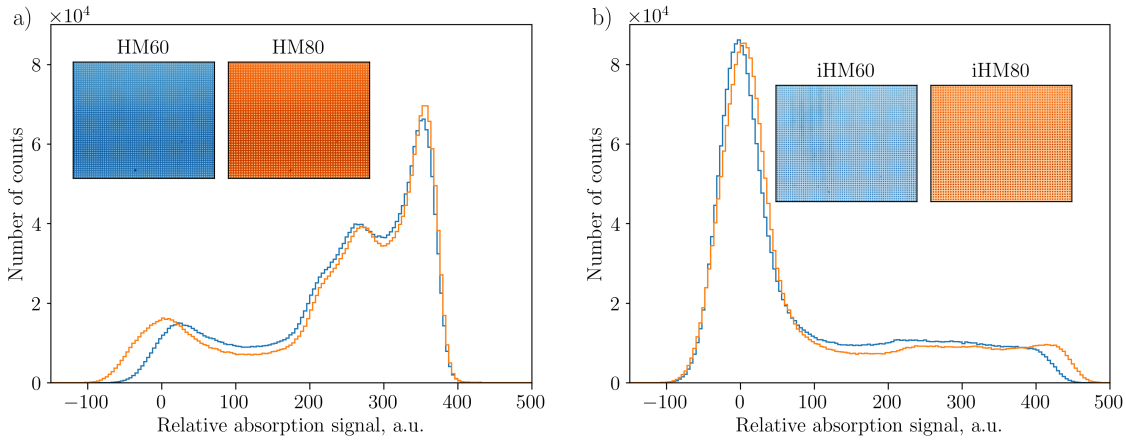

Figure 3.12: Real data absorption signal histogram for the conventional (a) and the inverted (b) Hartmann masks made on graphite substrate. The insets show the projections of the masks.

were introduced to the ideal arrays and associated with the changes in the absorption signal histograms. It is important to note that the proposed quality evaluation algorithm gives valuable information only for intrinsically periodic structures such as gratings or Hartmann masks.

The main idea of the mask quality evaluation algorithm was to test the mask in a radiographic setup and compare the intensity distribution obtained on the detector plane with the simulated intensity map from an ideal mask. According to a simplified empirical model, a perfect mask was represented by a two-dimensional array of data with the same dimension as the digital image obtained from the actual data, considering the magnification. The array was filled with a constant value, and an intensity distribution histogram was obtained. This gave a discrete spectrum consisting of two peaks at absorption signals for the wafer (if normalized by the absorption level of the wafer, this peak is centered at zero) and the gold structures (Figure 3.13a). The ratio of peaks is 1:3 as the gold structures cover one-third of the illuminated mask area in the simulated experiment. By modifying the simulated ideal arrays, one can estimate the intensity modulation quantitatively and characterize structural changes in the real mask. The code to simulate an ideal projection for the conventional and inverted mask designs can be found in Appendix A.

When the arrays and associated intensity distribution histograms were obtained, the real mask projection was approximated by adding a background function representing noises introduced by the experimental setup. This was done by introducing random fluctuations around the central value as detector noise (Gaussian distribution). The intensity distribution in the beam was accounted for using the actual signal recorded by the detector in the experiment as a background. The intensity distribution histogram with added noise and real background is shown in Figure 3.13b). As the silicon substrate supported the mask structures, it introduced a certain absorption, which decreased the signal-to-noise ratio and could also be treated as a contribution to the background. The detector noise was further estimated together with the contribution of 200-µm-thick silicon absorption. Thus, the histogram peaks were shifted so that the zero position corresponds to the radiation passing between the mask structures. The second peak was placed at the absorption level of gold structures, which was determined by the gold height.

However, in reality, the detector noise decreases the efficiency of intensity modulation and blurring caused by the not perfectly steep profile of structure sidewalls. Note that this manufacturing-driven blurring is independent of the blurring of the projected mask edges by the source focal spot size (focal spot size in case of an X-ray tube or lens focusing spot for a lens system). Despite the different origin both result in blurring of the projected image, which is stronger for smaller periods: one can see that for the simulated mask with 10 µm period, the intensity distribution is not discrete anymore, and peaks associated with absorption of

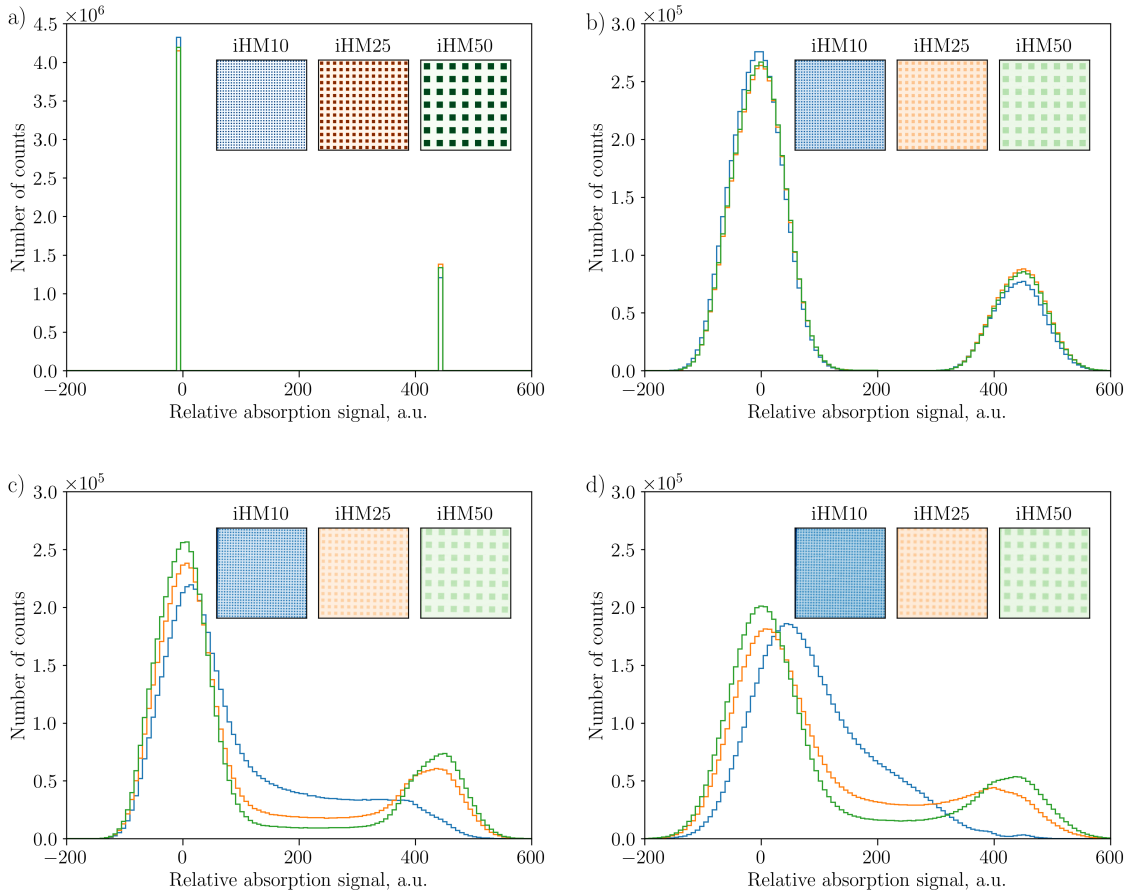

Figure 3.13: Relative absorption histograms for the simulated inverted Hartmann mask projections with periods of 50 µm (green), 25 µm (orange), and 10 µm (blue): a) without noise or blur and with uniform background (mean value 8400 counts); b) with added detector noise (standard deviation 25) and real background; c) with added detector noise (standard deviation 25), real background, tilted to -0.6 and blurred (sigma = 1.5); d) with added detector noise (standard deviation 45), real background, tilted to -0.6 and blurred (sigma = 2.5). The insets indicate the cropped simulated data arrays. The simulation represented the influence of generalized pattern defects and decoupled them from the impact of local imperfections.

the wafer and the structures are merged and not clearly distinguished as can be seen in Figure 3.13(d). The histogram shown in Figure 3.13(c) has been obtained by varying the input parameters such as in-plane rotation of the mask and blurring of the image to match the experimental conditions and decouple the influence of generalized pattern defects from local imperfections. As one can see from the projection images shown in Figure 3.10, there was a slight in-plane rotation of the mask present when the mask was placed in the holder. The simplified empirical model included the rotation angle of 0.6 degrees to represent the acquired images better and account for smoothening out of the ripples in the histogram.

It is important to emphasize that simulated data only included general distortions uniformly applied to the entire pattern, and no local defect impact was considered. By comparison of the histogram obtained from experimental data (Figure 3.10) and simulated one (Figure 3.13), it is clear that only pattern blurring cannot explain the distribution obtained for the masks. In particular, the splitting of the peaks corresponding to gold absorption, especially evident for the 10 µm period mask (Figure 3.11a), cannot be attributed to uniform effects present in the pattern, but rather local defects of mainly random and rare appearance. One kind of such effect is gold overplating, which causes the appearance of higher absorption levels. However, at the designed X-ray energy, the gold structures with an average height of 15 µm transmit only 0.5 % of the incoming radiation [62]. This means that the gold structures higher than 14 µm will not have a considerable effect on the intensity modulation. Overplated structures which contribute to the gold pillars higher than 20

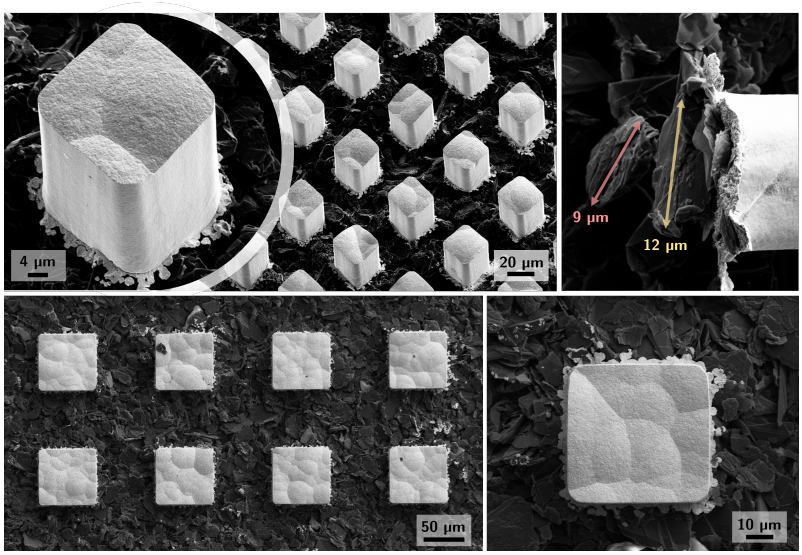

Figure 3.14: Inverted Hartmann mask manufactured on the substrate based on polyimide (Vespel) with carbon coating. The coated carbon has large grain size (around 10 µm), which results in the poor abhesion of the golden pillars.

µm will not make any impact on the absorption signal histograms obtained from the measurements at the energy of 8.5 keV.

3.6 Other possible substrates

Other combinations of substrates and conductive coatings are compatible with UV lithography. A popular choice of the low-absorbing substrate in X-ray lithography is a polyimide substrate (e.g., DuPont Vespel^{TM}), coated with a CrAu (10/70 nm) conductive layer. Unfortunately, due to the high reflectivity of gold surface in the UV region, such substrates cannot be routinely used with UV lithography. Even the use of standard anti-reflective coating does not form a stable photoresist pattern and results in photoresist lift-off. However, a different conductive coating can profit from polyimide thermal and mechanical stability and low absorption in the X-ray region. For example, a thin carbon layer can be deposited on the polyimide (usually on both sides to prevent substrate bending). The substrate can be further processed with the same parameters as a graphite substrate. An example of a Hartmann mask fabricated on such substrate (after photoresist stripping) is shown in Figure 3.14.

Another alternative is to deposit a smoother coating that will not form flake-like structures such as graphite and would withstand stripping with plasma. An attempt to create Hartmann masks on a polyimide substrate with titanium coating demonstrated low adhesion both between the titanium and polyimide and between titanium and the photoresist (Figure 3.15).

Multiple issues with titanium coating delamination during oxidation and the photoresist lift-off could not provide sufficient quality of the photoresist pattern to be used for gold electroplating. However, such substrates perform well in terms of the smoothness of photoresist sidewalls and the height of the photoresist pattern achieved. Perhaps the optimization of titanium deposition and careful tuning of oxidation and exposure parameters can result in successful fabrication of Hartmann mask, albeit of the limited area due to adhesion problems and reduced reproducibility of the manufactured pattern.

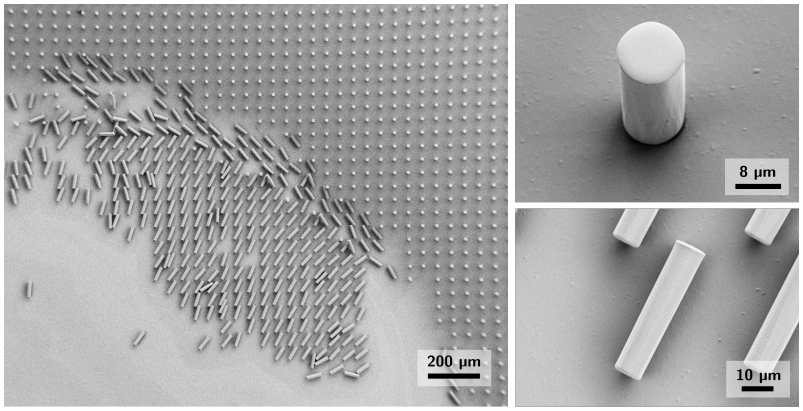

Figure 3.15: Photoresist pillars manufactured on the Vespel substrate with oxidized titanium coating. The smooth surface of the titanium does not provide sufficient adhesion.

3.7 Conclusions

In this chapter, the technological process for the fabrication of conventional and inverted Hartmann masks was described. The fabrication process is based on UV lithography and gold electroplating and is compatible with silicon and graphite substrates. The inverted Hartmann masks represented by periodic free-standing gold pillars with lateral structure sizes from 5 µm to 25 µm and heights from 5 µm to 28 µm have been manufactured on silicon substrate. The masks have shown a high degree of periodicity and defect-free patterns, which enables their application for single-shot X-ray phase-contrast imaging. Both conventional and inverted Hartmann masks were fabricated on the graphite substrate, following the processing steps established for silicon with slight adjustments of substrate pretreat. Gold meshes and arrays of pillars with periods from 30 to 80 µm with gold height of 30 µm were manufactured. The gold height achieved in the manufacturing process (28 and 30 µm) absorbs more than 90 % of X-ray radiation at the energy of 25 keV. Taking into account the transmission of the 200-µm-thick silicon substrate at this energy, the WFM of the mask is about 0.8. For 500-µm-thick graphite substrate the WFM is 0.84, which implies that the manufactured masks can be used for single-shot imaging at the energies up to 25 keV.

An algorithm allowing the qualitative and quantitative characterization of homogeneity and uniformity of the micropattern over a large active area involved in the imaging measurement was developed. The simulated images include general effects like blurring, detector resolution limitations, noise, and misalignments. However, they do not include any information on local defects such as diffraction-induced shape distortion, overplating, pattern impurity, mask defects transferred to the final grating, etc. Such defects are becoming critical for small periods like 10 µm, as can be seen comparing the real data histograms with the simulated data, while larger periods are less affected by the abovementioned defects and exhibit clear intensity modulation. The evaluation of the Hartmann masks in the radiographic setup shows that the masks with periods 50 µm and 25 µm exhibit clear patterns and can be used for single-shot X-ray phase-contrast imaging at energies up to 25 keV. The masks with a 10 µm period have multiple manufacturing-driven defects and require further quality improvement, for example, by using deep X-ray lithography or improved photoresist formulations. The evaluation of the mask quality can also be further enhanced, most probably by introducing an image pattern recognition algorithm to be sensitive to minor localized defects.

The findings reported in this chapter can be used to improve image quality and broaden applications for X-ray phase-contrast single-shot imaging towards materials characterization and medical imaging. The developed algorithm could also provide additional information on the mask quality by utilizing a single projection for more straightforward data interpretation during measurements of various objects.

Table 3.4: Overview on several substrate options for Hartmann masks.

Substrate	Advantages	Limitations	Applicability
Silicon with titanium oxide (200 and 500 μm)	Highly compatible with lithography, fine rough surface ensures good absorption of both photoresist and gold.	High (more than 40%) absorption for X-rays below 20 keV for thickness of 500 μm. Thinner substrates (200 μm) are brittle but have lower absorption, although it is still substantial for energies below 15 keV.	X-ray imaging with energies higher than 15 keV for setups with high SNR (e.g. white synchrotron radiation).
Graphite (500 μm)	Low absorption, high adhesion for photoresist and gold, mechanical stability and electrical conductivity without additional coatings.	Soaking of photoresist results in inhomogeneous thickness and non-flat surface which reduces precision for contact exposure mode, underplating of gold, high scattering of structures over wide range of sizes.	Phase-contrast imaging with lower energies, when scattering contrast is not a priority or scattering structures are larger than 1 μm. To increase the visibility and lower the graphite scattering impact the mask can be placed close to the detector.
Polyimide (Vespel) with carbon coating	Low abosoprion, high mechanical stability, less scattering compared to the graphite substrate.	Flaky surface still scatters, so the disadvantages of the graphite substrate are shred to some extend. Stripping of the resist has to be done carefully, as the gold pillars are not connected to the main carrier surface.	Can be used in a similar manner as the graphite substrate but with reduced impact from scattering.
Polyimide (Vespel) with titanium coating	Low absorption, mechanical stability, no substrate-induced scattering.	Complicated and unreliable manufacturing due to the poor adhesion between polyimide, titanium and photoresist. This can restrict the reproducibility or limit the area of the mask. Oxidation can result in delamination of the titanium layer.	No limitations on applicability imposed by the substrate.
Polyimide (Vespel) with Cr/Au coating	Low absorption, mechanical stability, no substrate-induced scattering.	Not compatible with UV lithography due to the high reflectivity of the gold layer. Deep X-ray lithography has to be applied which is not covered in this work.	No limitations on applicability imposed by the substrate.

4 X-ray phase-contrast imaging with Hartmann masks

X-ray phase-sensitive imaging is a powerful tool for non-destructive characterization of materials with low absorption contrast. Phase contrast imaging is associated with the refraction of X-rays in the object under investigation. The possibility to detect phase shift of X-rays in the materials is available via a number of techniques [1]. One of them, the Hartmann mask, is a wavefront sensing approach, extended from visible light to the X-ray radiation. This approach has many advantages such as high robustness, relaxed requirements to the beam coherence and monochromaticity, simplicity and flexibility of the setup. Unfortunately, these advantages come at the cost of a high spatial resolution of the final image.

In this method, regularly spaced apertures are used to introduce a periodic modulation to the incident beam in the form of periodic spots. In the presence of the investigated sample, this modulation is distorted due to X-ray refraction and scattering. There are several approaches on analyzing these distortions, including direct tracking of the spot displacement [63], Gaussian fitting of the individual spots [64] and Fourier analysis of the periodically modulated image [30]. Due to the fact that the sampling of the wavefront is periodic, Fourier analysis can be effectively applied to quantify the distortions and retrieve differential phase shifts in horizontal and vertical directions [20].

Besides a conventional Hartmann mask design – an array of regularly spaced apertures – an alternative inverted design is possible: an array of absorbing pillars, which forms a periodic pattern, as have been discussed in Chapter 3. Such a design could be potentially advantageous because it makes measurement more flux-efficient due to less absorption in the optical component.

In this section, I will compare the performance of Hartmann masks and inverted Hartmann masks of different periods for phase-sensitive X-ray imaging. I will compare the customized Hartmann and inverted Hartmann mask designs for phase contrast X-ray imaging, and demonstrate the applications of the inverted Hartmann mask to the time-resolved imaging of dynamic processes at different time scales.

4.1 Testing the inverted and conventional Hartmann masks with synchrotron radiation

Conventional and inverted Hartmann masks have been tested in a radiographic setup using synchrotron radiation. The mask's performance was compared at the beamlines of the IPS imaging cluster of the KIT synchrotron facility. For the measurements, a quasi-monochromatic beam with the energy of 17 keV was used (bandwidth 2%). Detection of the X-rays was performed by the Andor Neo 5.5 X-ray camera coupled with lenses (magnification of 2.73) to achieve an effective pixel size of 2.4 µm. The conventional and inverted masks with period of 40 µm made on graphite substrate were used. The masks were placed at 43.5 cm from the detector (Figure 4.1). The experiment aimed to compare the phase-contrast imaging capabilities of two masks in an identical setup. For the comparison, a prism made of PMMA was used as a pure phase object. The prism was longer in y-direction, it was placed directly behind the mask.

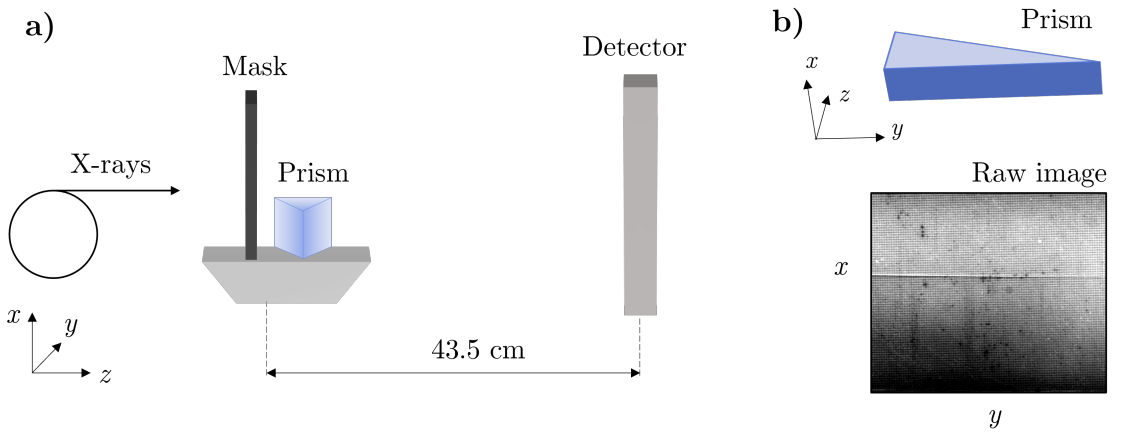

Figure 4.1: a) A schematic of the experimental setup for X-ray phase-contrast imaging of a PMMA prism using synchrotron radiation. The X-rays are incident on the mask (Hartmann or inverted Hartmann design), and the prism is placed on a stage directly behind it. The distance between the stage and the detector is 43.5 cm. b) The prism is elongated in y-direction. The raw image recorded by the detector for the inverted mask design is shown below the prism.

The refraction at the edge of the prism shifts the projected spot array proportionally to the phase gradient. As analyzed by the Spatial Harmonic analysis (see Section 2.7), this shift will be manifested in the phase-contrast image as an increased signal at the border of the prism. While the phase in this case is a step function, the phase gradient that is measured is a peak function. The height of the peak and the background noise (standard deviation of the signal) are important for the estimation of the sensitivity.

In Figure 4.2 one can see the absorption, scattering, and phase-contrast images for the PMMA prism, acquired with the conventional and inverted Hartmann mask designs. One can see that the absorption image for the inverted Hartmann mask exhibits a slightly higher contrast between the prism and the air. The scattering image contains some signal from the border of the prism, indicating the refraction at angles below the phase-detection limit. The phase detection limit can be defined as the angular resolution for a shift of one pixel. It is affected by the noise level in the image and the geometric properties of the setup [27]:

$$\alpha_{min} = \frac{PS}{L} \cdot I_{noise}, \tag{4.1}$$

where α_{min} is the minimum detectable refraction angle, PS is the detector pixel size, L is the distance between the object and the detector, and I_{noise} is the standard deviation of the signal in the background (area outside the sample) for differential phase contrast images. The phase detection limit was 2.7 µrad in this setup for both masks.

In both differential phase-contrast images, one can see the edge of the prism. The image acquired with the inverted Hartmann mask has lower noise and a higher relative signal from the refracting border (Figure 4.2). The strength of the signal changes along the edge of the prism. Quantitative comparison was done using the peak signal-to-noise ratio, which was calculated as the ratio of the peak height (phase signal at the prism edge) over the standard deviation value of the noise floor (area outside the prism):

$$SNR = \frac{peak}{SD}, \tag{4.2}$$

where $peak$ is the maximum signal, corresponding to the height of the peak, and SD is the standard deviation of the signal outside of the prism. The SNR for the image from the inverted Hartmann mask is 68, while the image from the conventional Hartmann mask has a SNR of 47. The difference in the SNR is due to a higher signal at the edge of the prism for the inverted Hartmann mask ($peak$ = 4.52) compared to the image

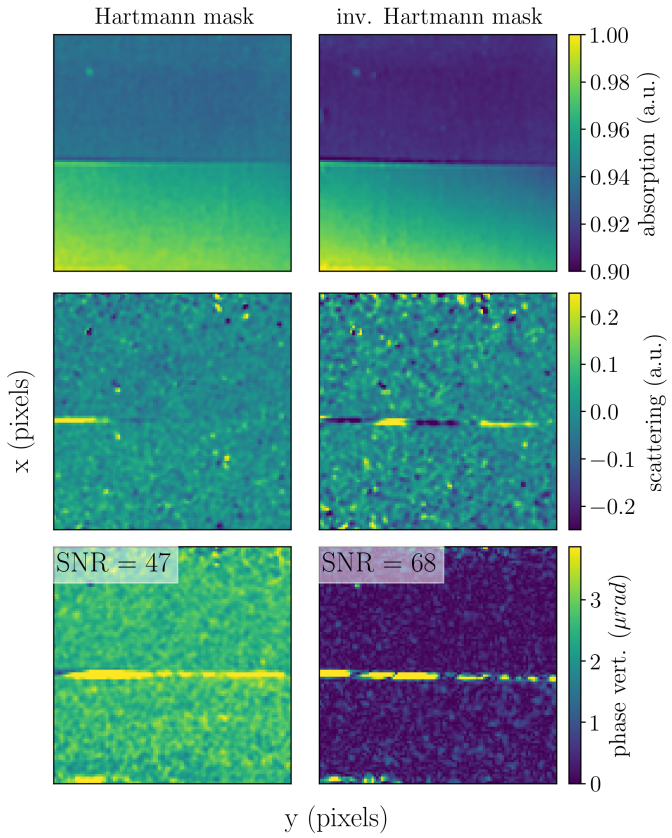

Figure 4.2: A comparison of conventional (left column) and inverted (right column) Hartmann mask performances in a radiographic setup with synchrotron radiation at 17 keV. Absorption, scattering, and phase contrast images (in vertical direction) for the PMMA prism. The SNRs are calculated according to Eq. 4.2.

obtained with conventional one ($peak$ = 2.37). The standard deviation SD for images with conventional and inverted masks was 0.05 and 0.07, respectively. Both masks provide sufficient contrast to see the edge of the prism, but the inverted mask design ensures superior image quality.

4.2 Testing the the inverted and conventional Hartmann masks with laboratory source

To further confirm the results of comparing the conventional and inverted Hartmann mask designs with monochromatic synchrotron radiation, the imaging of test samples in a laboratory setting was performed.

Phase-contrast imaging measurements were carried out at the Computed Lamiography/Computed Tomography Lab of the Institute for Photon Science and Synchrotron Radiation (IPS) at the Karlsruhe Institute of Technology (KIT). The X-ray tube (X-RAY WorX) was operated at 40 kVp providing peak energy of about 24 keV. The focal spot size of the X-ray tube was 15 µm. The X-rays were detected with a Medipix3RX detector system featuring a 500 µm thick silicon sensor with a pixel size of 55 µm. The detector consisted of 12 chips stitched together to form 8.4 cm x 2.7 cm detector area. The exposure time was 10 seconds for one frame with averaging over 20 frames.

The object for study was a plastic vial, which was placed 5 cm (D_1) away from the source (see Figure 4.3). The mask (either conventional or inverted) with period 30 µm was located downstream the object at the

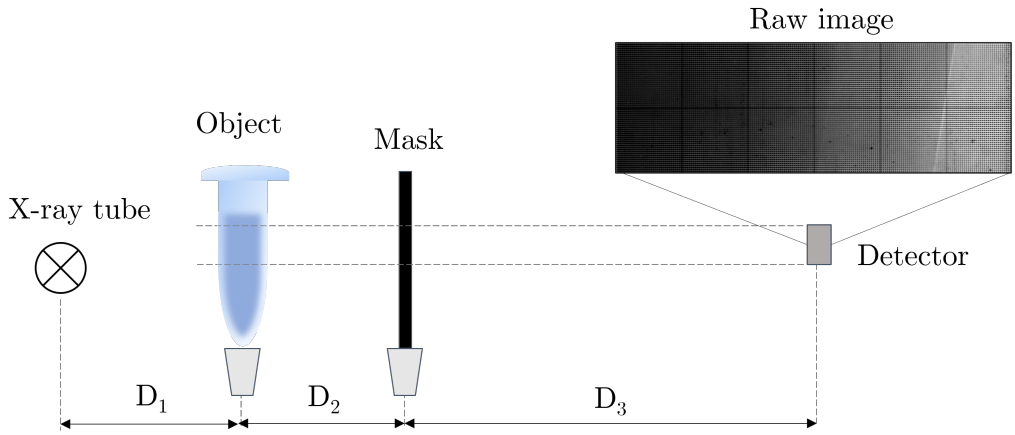

Figure 4.3: A schematic of the experimental setup for phase-contrast imaging of a plastic vial with a laboratory source. The object is placed close to the X-ray source (distance D_1) and the Hartmann mask (inverted or conventional) is located downstream of the object (at the distance D_2). The detector is an array of 12 chips stitched together, it is placed at the distance D_3 from the mask.

distance 10 cm (D_2). The mask-to-detector distance (D_3) was 130 cm. The distances were chosen to satisfy the following criteria to minimize artifacts [57]:

$$E_1 = \frac{s}{P} \cdot \frac{D_3}{D_1 + D_2 + D_3} << 1 \tag{4.3a}$$

$$E_2 = \frac{s}{P} \cdot \frac{(D_1 + D_2)(D_2 + D_3)}{D_1(D_1 + D_2 + D_3)} > 1 \tag{4.3b}$$

where s – focal spot size of the X-ray tube, P – period of the mask (physical, not projected), D_1 – distance from the source to the object, D_2 – distance from the object to the mask, D_3 – distance from the mask to the detector (see Figure 4.3). The image reconstruction was done according to *Reich et al.* [29, 65].

The spatial resolution of the setup is defined as the period of the mask projected onto the object under investigation. The phase detection limit in such setup can be estimated from the setup parameters and noise level in differential phase contrast images as follows:

$$\alpha_{min} = \frac{PS \cdot D_1}{(D_2 + D_3)(D_1 + D_2 + D_3)} \cdot I_{noise}, \tag{4.4}$$

where α_{min} is the minimum detectable refraction angle, PS is the pixel size (physical), D_1, D_2 and D_3 are the distances in the setup (see Figure 4.3), and I_{noise} is defined as the standard deviation of the signal in the background (area outside the sample) for differential phase contrast images. Following the sampling theorem, the angular resolution can be defined as $3 \times \alpha_{min}$.

In Figure 4.4 one can see the edge of the vial, which refracts X-rays in horizontal direction, and thus can be observed in phase contrast images. Due to the fact that the chips of the detector were stitched together, the borders of the chips are visible in phase-contrast images, albeit less for the images obtained with the inverted Hartmann mask. This indicates that such mask design can be more robust against detector imperfections.

In order to analyze the whole area of the detector, the retrieval of contrast have also been performed for the area of each individual chip and then stitched together to form the full field of view of the detector such that one can compare the phase contrast images in terms of the signal-to-noise ratio. In Figure 4.5 one can see absorption and the normalized horizontal differential phase contrast signal for the measurements with the

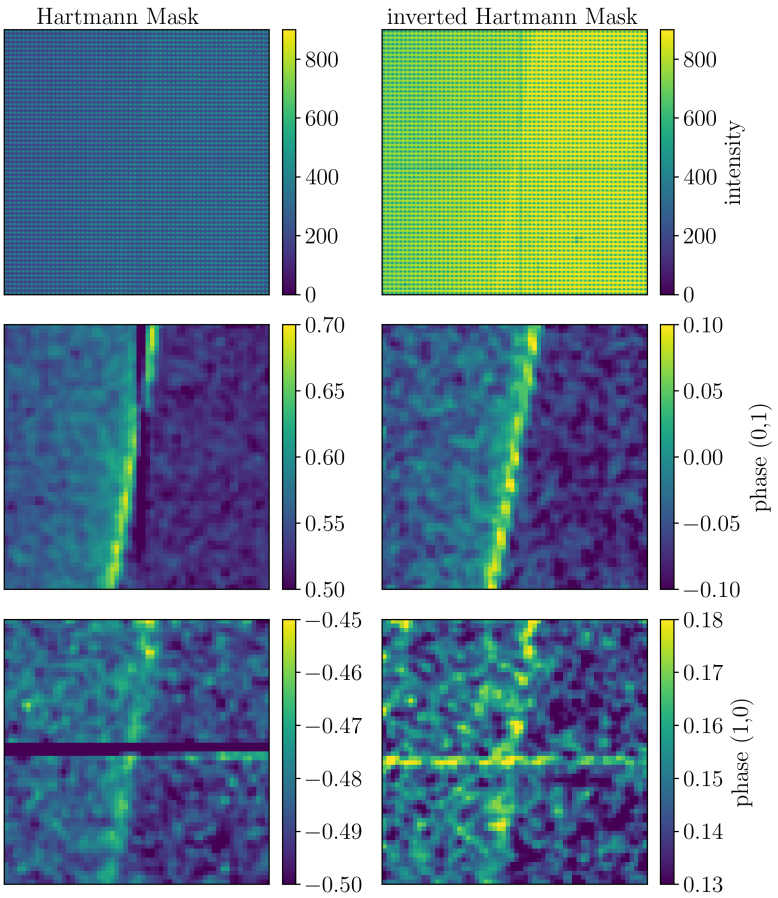

Figure 4.4: The raw projections (upper graphs), differential phase in the horizontal (0,1) and vertical (1,0) directions for the measurements with conventional and inverted Hartmann masks. The stripes in the images are corresponding to the borders of the detector's chips. The images shows one third of the total detector area (6 x 2 chips).

conventional an the inverted Hartmann masks. For the line profile obtained from the phase contrast images signal strength was accessed using SNR calculated according to Eq. 4.2. As one can see in the lower graphs in Figure 4.5, the differential phase contrast image obtained with inverted Hartmann mask has a slightly higher SNR, although the values for both masks are very close and the images look very similar. Angular resolution of 1.4 µrad have been achieved for both masks in this setting.

Another important contrast modality, which was obtained in the measurements, is scattering contrast. It has demonstrated very different values for the measurements, although the sample and the setup was not change. Both masks were fabricated on the same wafer so no changes in the scattering and transmission of the wafer carrier is expected. In Figure 4.6 one can see that the absorption contrast for conventional Hartmann mask is lower than for the inverted, while the scattering contrast for the conventional mask is much higher than for the inverted. As there were no strong scatters present in the sample, the scattering contrast was expected to be very low, with weak indications of the inner and outer borders of the vial, as observed for the inverted Hartmann mask. The scattering signal for conventional HM is thus comes from the cross-talk between the absorption and scattering signal, which was reported elsewhere [17, 66]. The lower graphs in Figure 4.6 are the scatter plots of scattering versus absorption which reveal the clear linear cross-correlation between the absorption and scattering for the conventional Hartmann mask with the slope coefficient $k = 2.72$. For the inverted Hartmann mask no such strong cross-correlation is observed: there is a very slight positive slope for the linear fitting curve with $k = 0.6$.

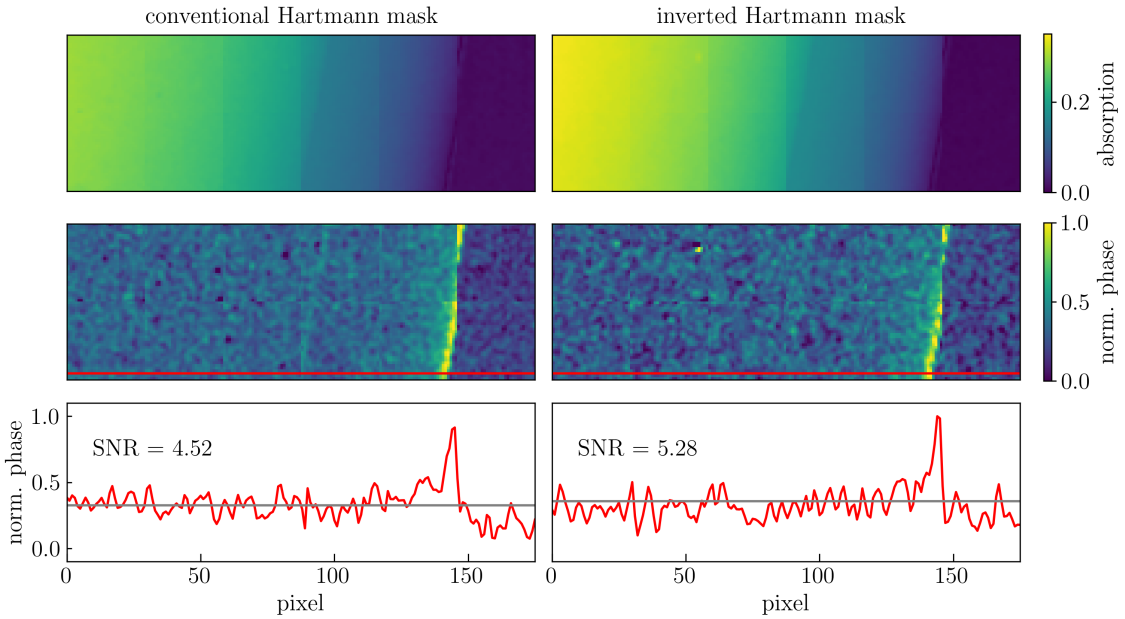

Figure 4.5: Absorption and phase contrast images for the vial (acquired with the conventional and inverted Hartmann masks) for the whole field of view of the detector. The phase contrast images were normalized to facilitate better comparison of the SNR.

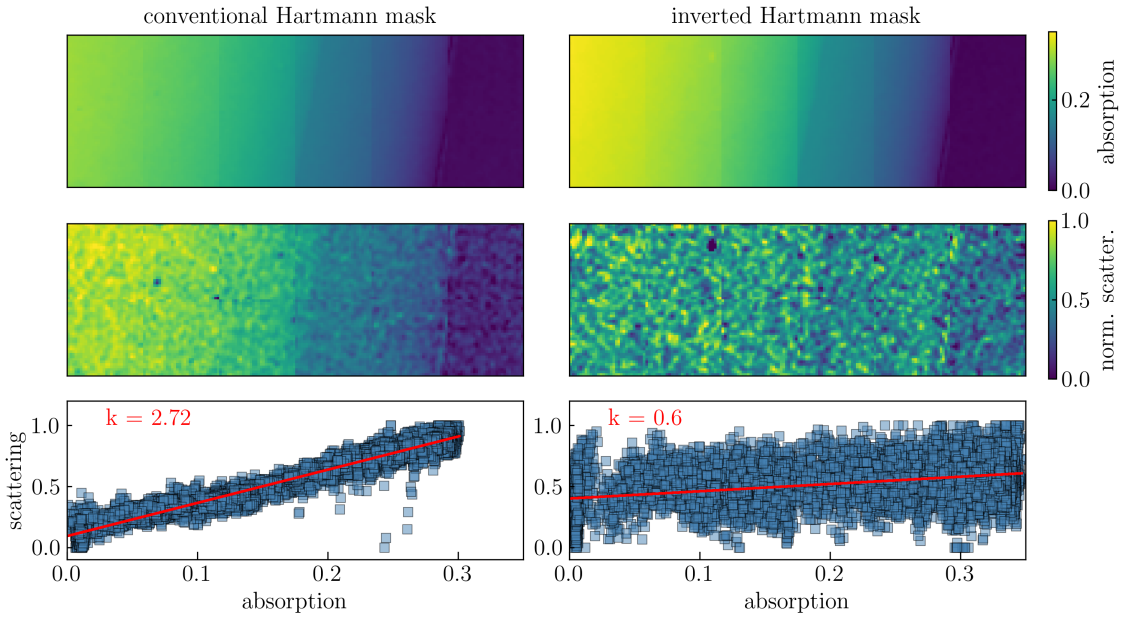

Figure 4.6: Absorption and scattering images for the vial (acquired with the conventional and inverted Hartmann masks). The scatter graphs indicate a significant cross-talk between absorption and scattering for conventional Hartmann mask (left), while the inverted mask design (right) shows a weaker correlation between scattering and absorption.

In this Section, the comparison of the masks have been performed. I have compared conventional and inverted Hartmann masks intended for phase-contrast imaging. Both masks were fabricated by UV lithography on a graphite substrate. From the manufacturing point of view both mask have similar quality: regular periodic patterns with insignificant defects. However, conventional Hartmann masks can be more durable, as gold pillars with aspect ratio higher than 2 (aspect ratio here is a ratio between height and width of the structure) tend to collapse over time due to mask handling.

Phase-contrast imaging revealed that both mask provided similar image quality, with a slightly higher SNR for the inverted design. The angular resolution was identical (1.4 μrad). The measurements with conventional Hartmann mask revealed a significant correlation between the scattering and absorption signals, which resulted in both lowered absorption contrast and falsely increased scattering signal. The use of the inverted mask design did not lead to the formation of spurious signal in scattering images. From this once can conclude that the inverted Hartmann mask has a potential to provide good quality phase images and more accurate contrast retrieval.

The advantages of the inverted Hartmann mask are even more prominent in more challenging measurement environments, such as for time-resolved measurements. In these conditions, it might be even beneficial to use the inverted design in terms of angular resolution due to the higher flux obtained at the detector plane as the absorbing structures area is decreased, and as a consequence lower noise values. Based on the results of this section, the time-resolved measurements were performed with the inverted mask design as it exhibits less cross-talk between the absorption and scattering signals and provides a slightly higher SNR for the phase contrast images.

4.3 Time-resolved imaging with inverted Hartmann masks

4.3.1 Imaging of laser ablation with white beam

In this Section, the application of the inverted Hartmann mask for time-resolved single-shot phase-contrast X-ray imaging is presented. The inverted Hartmann mask is a periodic array of free-standing gold pillars. The array was manufactured by UV lithography and electroplating. Time-resolved measurements have been performed for imaging of pulsed laser ablation in liquids using white beam synchrotron radiation. Image processing was performed following the Fourier analysis approach. The inverted Hartmann mask in combination with single-shot imaging technique provides a sufficient differential phase contrast even at very short exposure times. It can be effectively used for phase-contrast X-ray imaging of fast dynamic processes with a temporal resolution on the millisecond scale.

The results reported in this section have been published in *M. Zakharova, S. Reich, A. Mikhaylov, V. Vlnieska, TdS. Rolo, A. Plech, D. Kunka. Inverted Hartmann mask for single-shot phase-contrast x-ray imaging of dynamic processes. Optics Letters. 2019; 44 (9):2306-2309.*

4.3.1.1 Introduction

Since the discovery of X-ray radiation by Wilhelm Röntgen, X-ray imaging became an analytical instrument for non-destructive characterization in various fields, such as materials science, medicine, security, and industry. Conventional X-ray imaging systems convert the variation of the X-ray absorption cross-section of different materials into variations of intensity at the detector. For weakly absorbing materials, X-ray phase-sensitive imaging emerged as a powerful tool for the visualization of internal structures of materials, where

phase shifts due to changes in the refractive index enhance the visibility of edges and interfaces. A number of techniques for the detection of refraction and scattering of X-rays by the sample were developed in recent years, such as propagation-based [67], grating-based (both interferometric [68] and non-interferometric [30]), analyzer-based [69], speckle-based [70] and edge illumination [15] methods.

Some of those techniques (e.g., grating interferometry) require several sub-images per measurement to quantify phase shifts. For the investigation of fast processes, however, such an approach may be restrictive. Therefore, several research groups have devised novel techniques for single-shot imaging applications [20, 27, 54, 64, 71], where different contrast modalities can be retrieved from a single image. In grating interferometry, a Moiré approach has been developed to circumvent this problem [72], which however only provides differential phase contrast information in one dimension. Recently, an extension of this approach towards two-dimensional fast single-bunch grating interferometry has been proposed for visualization of repeatable processes [73]. Nevertheless, robust and fast phase imaging can be achieved by non-interferometric beamlet techniques [20, 54, 64, 70], such as the Hartmann mask approach [20, 27, 60, 71, 74].

In phase-sensitive X-ray imaging, decreasing exposure time while keeping an acceptable signal to noise ratio (SNR) leads not only to reduced dose deposited in the sample [75], but also to establish high-speed imaging techniques. The phase information of the object under investigation enhances fast measurements: it furnishes additional information on dynamic processes in materials science.

Fast X-ray imaging has also been demonstrated using 2D compound array refractive lenses [29] and a Shack-Hartmann sensor for hard X-rays [27]. The lenslet arrays benefit from the focusing effect and lower absorption increasing the local flux density. However, Hartmann masks are simpler to fabricate, straightforward to scale up to areas of several centimeters, easy to apply at higher X-ray energies and tolerant to defects, imperfections and dispersive chromatic aberrations. This particularly applies to isolated absorptive structures compatible with the LIGA process [76]. Here we show that an inverted Hartmann mask leads to a similar signal formation as the original Hartmann masks or speckle-based approaches due to Babinet's principle.

4.3.1.2 Materials and Methods

The inverted Hartmann mask. The inverted Hartmann mask was fabricated on a Ti/TiOx coated silicon wafer by employing UV lithography and gold electroplating. The lithography process was optimized for fabrication of clean structure arrays out of a thick photopolymer layer. Briefly, the fabrication process consisted of several steps, mainly photoresist spin-coating, exposure, post-exposure bake, development and gold electroplating. In our case, a SU-8 based, chemically amplified negative photoresist mr-x 10 (micro resist technology GmbH, Berlin, Germany) was applied on the substrate. After photoresist spin-coating, the layer was exposed to i-line UV light using a Cr mask. The exposure triggered a cross-linking mechanism in the photoresist, which resulted in the pattern formation. Note that in the case of inverted X-ray Hartmann mask - 2D array of gold micropillars - a large area of photoresist has to be exposed, while preventing small areas from being exposed to UV radiation. Such a case is challenging for lithography, because it usually leads to decreased homogeneity and induced proximity effects. However, careful control of every step and optimization of process parameters for exposure and post-exposure bake can help to overcome these challenges. The details on process optimization and final parameters can be found in [77].

The final structures were two-dimensional arrays with an area of 1 cm^2. The area can easily be scaled within the same fabrication approach, if necessary for the experiment. The period of the structures was 50 µm with the height of the gold pillars being 32 µm. As one can see in Figure 4.7a, the structures exhibit steep vertical sidewalls. The roughness of the gold surface on the sidewalls is associated with the photoresist granular

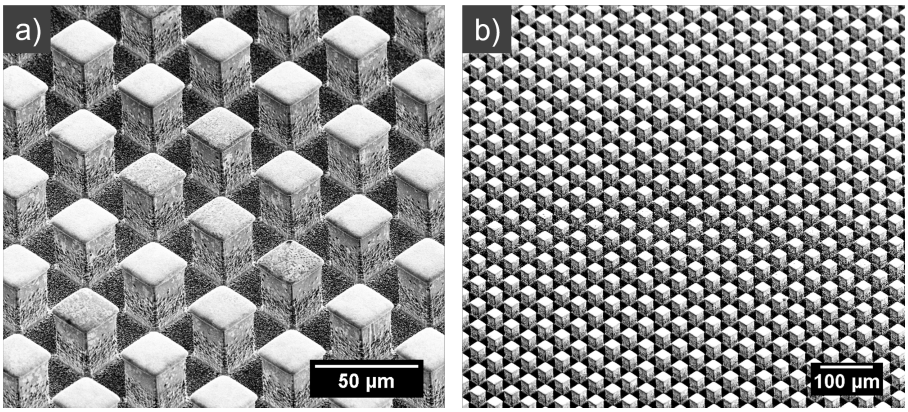

Figure 4.7: SEM images of the inverted Hartmann mask after resist stripping, rotation 45°, tilted to 50° to show the sidewalls and the bottom of the pillars: a) close-up view; b) overview [79].

structure which is the result of polymer molecule agglomeration [78]. Such imperfection does not strongly affect the image quality, as the mask is used for non-interferometric X-ray multicontrast formation. The mask is homogeneously periodic (Figure 4.7b), which ensures uniform beam modulation.

X-ray imaging setup. Dynamic time-resolved imaging of pulsed laser ablation in liquids has been performed at the TOPO-TOMO beamline of the synchrotron facility KARA at KIT (Karlsruhe, Germany). For time-resolved measurements, the white beam from the bending magnet was used, filtered by 0.2 mm Al to obtain a spectral peak at 14 keV. The 0.2 mm Si substrate of the inverted Hartmann mask further hardened the beam, leading to an effective spectral peak at around 17 keV (see Figure 4.8, bottom right). The X-ray detector consisted of a 50 µm LuAg:Ce single crystal scintillator screen, lens-coupled with a magnification of 2.3 to a PCO.dimax CMOS camera, leading to an effective pixel size of 4.8 µm. A frame rate of 10 kHz and an exposure time per frame of 30 µs was used during the experiments. A fourfold interleaving was employed to increase the effective frame rate to 40 kHz. Briefly, the ablation process was performed in a customized flow chamber [80], where the ablation from an immersed silver wire was triggered by a Nd:YAG laser (Continuum Minilite I) with a pulse energy of 10 mJ. Profiting from the repeatability of the process, an average of 49 images were obtained. The ablation process being a fast dynamic phenomenon occurring at the time scale of microseconds (for details see [29, 81]) served as a demonstrative, yet challenging example for the time-resolving capabilities of single-shot X-ray imaging using customized inverted Hartmann masks. Further details on experimental conditions and data processing can be found in [29, 65]. The white X-ray beam, incident on the grating, was spatially modulated by the periodic inverted Hartmann mask. The periodically modulated beam was recorded by the detector placed at a distance of 40 cm downstream of the ablation point. The recorded projections were, therefore, superpositions of grating and object-induced beam perturbations.

The inverted Hartmann mask is customized to the experimental setup by selecting the height of the absorbing structures such that more than 80 % of the incident radiation with central energy of 17 keV is absorbed. While the period of the structures defines the final spatial resolution, the intensity modulations induced by the mask still need to be resolved by the detector, leading to a constraint of 4.8 µm $\leq$ period of mask/3 in our case.

To assess the performance of the inverted Hartmann mask in the white beam, we calculated the visibility of the pattern according to:

$$V = \frac{I_{max} - I_{min}}{I_{max} + I_{min}} \tag{4.5}$$

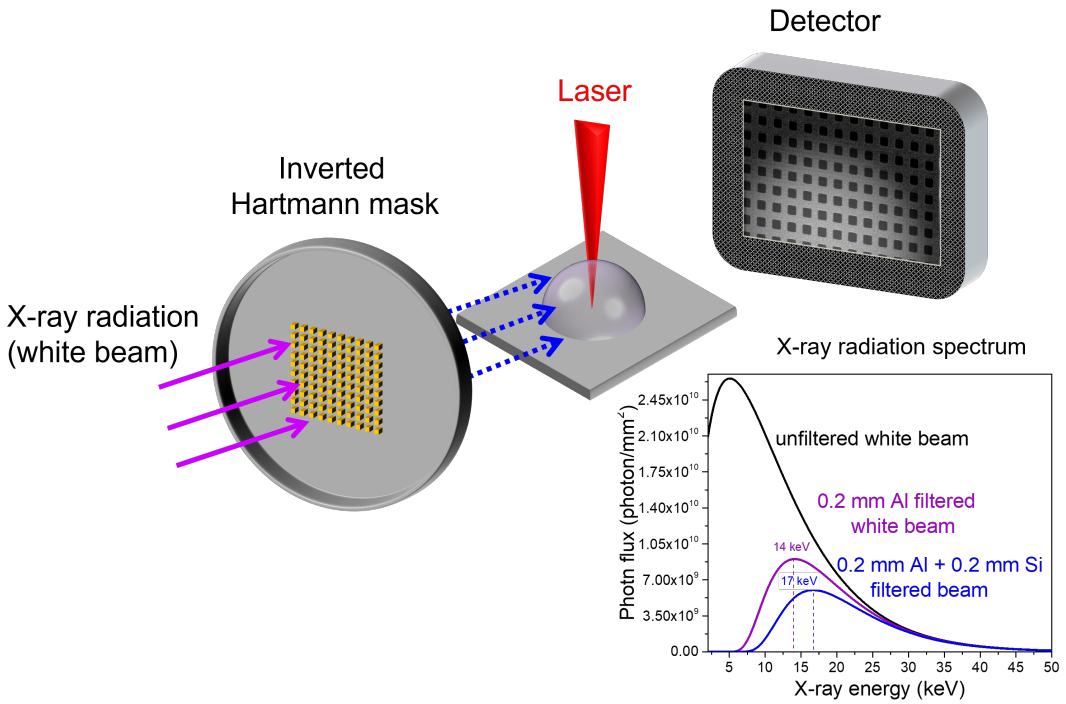

Figure 4.8: Setup for single-shot imaging with inverted Hartmann mask. The X-ray beam is spatially modulated by the absorptive structures of the mask to form a mesh of beamlets. This mesh is distorted by the refraction on the interface of the ablation bubble. On the bottom right, the (calculated) initial spectra from the bending magnet and the filtered spectra at the mask and the sample are plotted [79].

where I_{max} and I_{min} are the maximum and minimum intensities detected in the unit cell of the Hartmann mask.

The visibility for 49 times averaging was 11.7 %, and varied depending on the position from 8 % to 14 % (see Figure 4.9a). The variation might be due to the non-uniform illumination: the intensity decreased by 0.5 within the field of view (Figure 4.9b). The visibility was lower for higher intensities; this effect can be ascribed to the spectral width of the beam. The gold pillars were not high enough to absorb all photons of higher energies (from 20 to 50 keV). In the areas with higher intensities, the transmitted photons were sufficient to introduce an indistinguishable signal at the detector plane (about 6 % of the maximum intensity comes from high energy photons). The transmitted intensity spectrum peaks at 30 keV after passing through a gold pillar (Figure 4.9c). However, the average visibility of 11.7 % is sufficient to clearly observe the projected pattern (Figure 4.10b).

The temporal resolution is determined by the recording capabilities of the camera and the X-ray flux density. If a sufficiently high flux density is provided, the minimal time resolution is mainly dependent on the camera capabilities. In this work the flux density was the limiting factor leading to an exposure time of 30 µs. The SNR of a single exposure was low but since the process is repetitive, an averaging of 49 subsequent shots was performed, leading to a total exposure time of 1.5 ms. However, even averaging over less than 10 exposures (300 µs exposure time) made it possible to distinguish beam refraction caused by the ablation bubble, even with low SNR of around 2.

4.3.1.3 Results

The acquired images were processed in accordance with the procedures first published by *Wen et al.* [30].

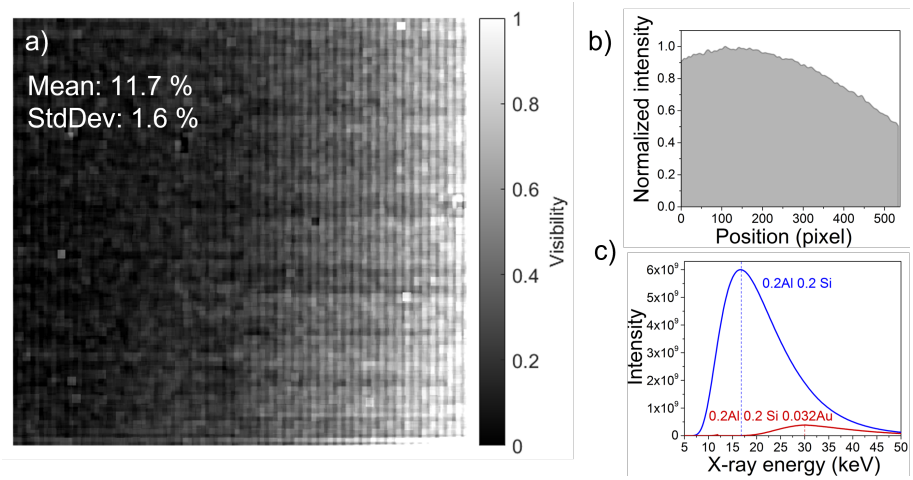

Figure 4.9: Characterization of object illumination: a) visibility map for inverted Hartmann mask in the white beam was calculated according to the Eq. 4.5 (average visibility is 11.7 %); b) normalized beam intensity in the field of view; c) X-ray spectrum of the transmitted radiation: intensity after the filtering with 0.2 mm Al and beam hardening by the 0.2 mm Silicon substrate (0.2Al 0.2Si - blue) and final spectra after the 32 µm high gold pillar (0.2Al 0.2Si 0.032Au - red) [79].

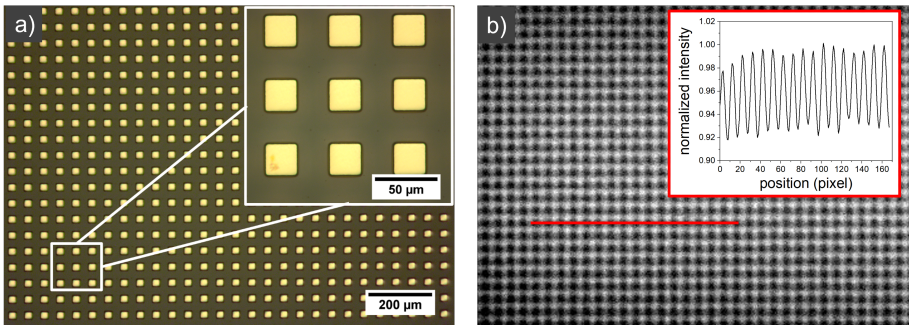

Figure 4.10: Inverted Hartmann mask characterization: a) top microscopic view of the array of gold pillars, b) X-ray transmission map with an intensity line profile as inset [79].

The results of the measurement of transmission and differential phase contrast for the laser ablation process are shown in Figure 4.11. The transmission signal of the first cavitation bubble is shown in Figure 4.11(a), which is followed by the first rebound (Figure 4.11(d)). Figure 4.11(b) and Figure 4.11(c) show the horizontal and vertical differential phase. While the transmission contrast has no additional information compared to normal absorption imaging, the differential phase shows strongly refracting areas in the sample, here the rim of the ablation bubble. The absence of any phase signal inside the ablation bubble shows that there are no resolvable internal structures. Figure 4.11(e) and (f) show the corresponding differential phase images for the first rebound, which has a much more complex structure.

Transmission and differential phase contrast images obtained in this study illustrate that fast dynamic phenomena can be recorded with sufficient signal to noise ratio at sufficiently small exposure times to avoid blurring due to motion, which is a challenge for other phase sensitive techniques. Even at exposure times on the µs scale and 20 shots averaging the phase detection limit was 1.2 µrad and for 49 shots it was 0.8 µrad. The detection limit is defined as the noise level of image areas without beam perturbation due to the ablation bubble. With longer illumination, hence higher counting statistics, an even higher angular sensitivity is possible. X-ray transmission and differential phase contrast information available with this method can be used for comprehensive analysis of phenomena in a complementary way. Apart from transmission and differential phase information, the scattering signal can also be retrieved from the single-exposure images. However, this type of contrast is strongly influenced by crosstalk with the absorption modality [17], highly sensitive to the X-ray spectral width and the signal-to-noise ratio.

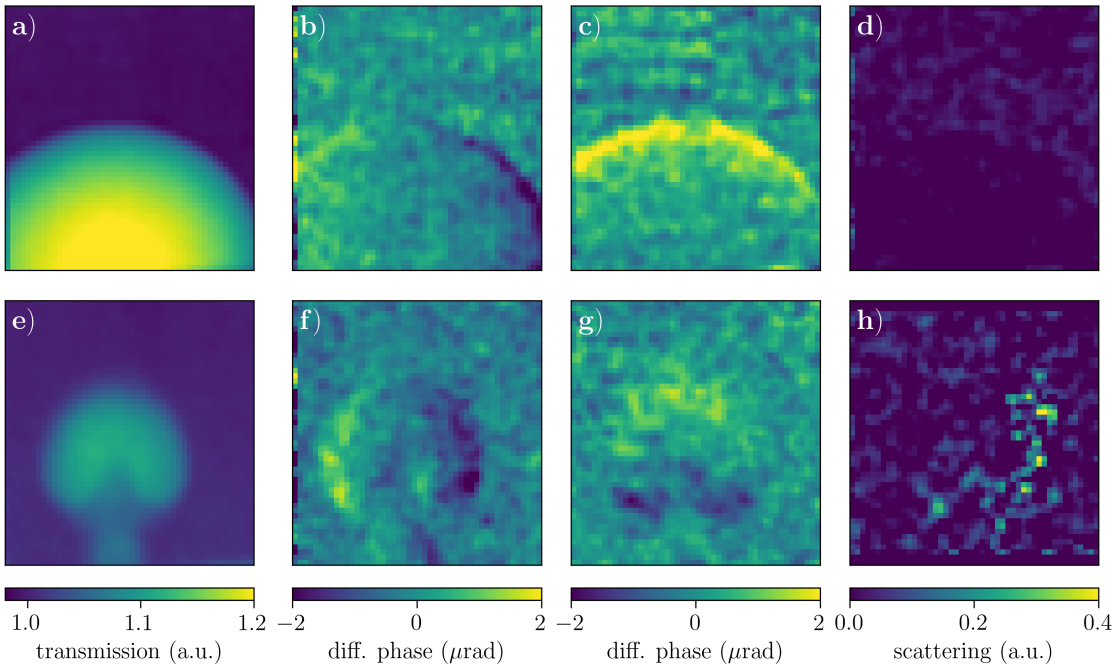

Figure 4.11: X-ray transmission (SNR = 13) (a, e), differential phase contrast in horizontal (b, f) and vertical (c, g) directions (SNR = 5), and scattering signal averaged over first order harmonics (01,10,11) (d,h) for the formation of cavitation bubble (a, b, c, d) and the first rebound (e, f,g,h) for 49 shots averaging (1.5 ms).

We used the absorption grating as an inverted Hartmann mask for fast measurements of the laser ablation process. Profiting from Babinet's principle, such masks act identically to the complementary Hartmann masks while providing higher flux at the detector plane due to the reduced amount of absorbing structures within the unit cell of the grating. For a perfect Hartmann mask, the area fraction in the unit cell which blocks incident radiation is 0.75, while for our inverted Hartmann mask it is only 0.25. The mask was manufactured using an inexpensive and high throughput UV lithography technique. Such masks can be easily scaled up to 5 x 5 cm^2 area with sufficiently large wafers and illumination field of the employed UV lamp. Absorber heights suitable for imaging at energies of up to 30 keV has already been achieved; however, there is a room for improvement by implementing other exposure approaches or highly sensitive photoresist materials. The presented time-resolved phase measurements of the ablation are promising for using inverted Hartmann masks to image dynamic processes.

For future applications we intend to upgrade the Hartmann masks by developing the gratings on low-absorbing substrates. Such optical elements will not result in hardening of the beam or significant loss of intensity for monochromatic radiation. This will lead to either a shortening of the exposure time or an increased sensitivity, depending on the specific application requirements. Several additional adjustments can be made to customize the inverted Hartmann mask for different applications, e.g. tailoring the height of the pillars, changing their duty cycle and shape. We also intend to expand the applicability of the inverted Hartmann mask to laboratory X-ray sources. Imaging of slower processes can be achieved even with low-flux tubes, if customized flux-efficient Hartmann masks unsusceptible to chromatic aberrations and incoherence are introduced.

4.3.2 Imaging of chemical reaction with quasi-monochromatic radiation

In this section, I present the application of single-shot multi-contrast X-ray imaging with inverted Hartmann mask to the time-resolved *in situ* visualization of chemical reaction products. The real-time monitoring of an illustrative chemical reaction indicated the formation of the precipitate by the absorption, differential phase and scattering contrast images obtained from a single projection. Through these contrast channels, the formation of the precipitate along the mixing line of the reagents, the border between the solid and the solution, and the presence of scattering structures of 100-200 nm sizes were observed. The measurements were performed in a flexible and robust setup, which can be tailored to various imaging applications at different time scales.

The results reported in this section have been published in *M. Zakharova, A. Mikhaylov, V. Vlnieska, D. Kunka. Single-Shot Multicontrast X-ray Imaging for In Situ Visualization of Chemical Reaction Products. Journal of Imaging. 2021; 7 (11):221.*

4.3.2.1 Introduction

Single-shot X-ray multicontrast imaging is a helpful tool for the visualization of inner structure evolution. Compared to conventional X-ray radiography, it offers additional contrast modalities such as phase and scattering (so-called dark-field). The phase-contrast image illustrates the wavefront irregularities caused by local differences in the real part of the refractive index [20]. Scattering contrast is obtained as a decrease in visibility of the wavefront modulation. It is attributed to the small-angle scattering caused by the structures well below the resolution of the imaging system [2].

Single-shot X-ray imaging methods based on a single optical element have the advantage of a simple and robust setup and do not require scanning the sample, in contrast to, for example, grating-based interferometry [2]. Various optical elements can be utilized, such as a two-dimensional absorption mask [79], microlens array [27, 28, 29, 81], speckle generating diffuser [82], etc.

Although the single-shot implementation usually comes at the cost of reduced spatial resolution, such imaging modalities have several advantages over widely used grating-based interferometric X-ray imaging [2, 83, 84]. Relaxed requirements on the optical element precision and alignment eliminate the need for high aspect ratio gratings and increase the mechanical stability of the setup and the simplicity of its operation. Moreover, the setup with a single optical element manufactured on the low-absorbing substrate provides higher flux efficiency. Lower absorption in the optical element increases the photon statistics, which is crucial for time-resolved imaging, especially using monochromatic X-ray beams with a limited flux density. Such modalities are straightforward to be utilized for the retrieval of several contrast modalities from a single projection. Thus, it enables multimodal monitoring dynamic systems at different timescales: from real-time imaging [85] to fast imaging at the scale of microseconds [29, 73, 74, 86].

Monitoring the dynamic systems *in situ* is a challenging but essential task aimed to enrich the understanding of the underlying mechanism and to define the timescale of the processes involved. Authors in several works have shown the possibility of performing in situ experiments using phase-contrast imaging (PCI) techniques, such as in-line holography PCI [87], propagation-based PCI [88], ptychography [89], etc.

Inverted Hartmann masks (iHMs) are simple but effective optical components that provide the wavefront modulation required for the subsequent retrieval of phase and scattering contrast modalities. They are represented by the arrays of periodic absorptive structures manufactured on a transmitting substrate. The iHMs provide high visibility when manufactured on low-absorbing materials and are easily scaled to a large

field of view (FoV). They provide an increased photon flux at the detector due to the smaller area of the absorbing structures compared to a conventional mesh-like design. Inverted Hartmann masks manufactured on silicon substrates have already been used for the imaging of dynamic processes with intense white beams [79]. However, for monochromatic beams or laboratory X-ray setups, such masks cannot provide a high signal-to-noise ratio (SNR) due to the substantial absorption in the optical element. The manufacturing of the optical components on low-absorbing material such as graphite has been shown to improve visibility and flux efficiency [90]. The inverted Hartmann masks on graphite substrates have been successfully applied to phase-contrast imaging with an X-ray tube [91].

In this section, the inverted Hartmann mask made on a low-absorbing graphite substrate are applied to the time-resolved *in situ* visualization of chemical reaction products in a single-shot imaging setup. We performed real-time monitoring of copper hydroxide precipitation via the absorption, differential phase, and scattering contrast images obtained from a single projection. Small unresolvable changes in the refractive index were also detected by evaluating the scattering signal.

4.3.2.2 Materials and Methods

Preparation of the reagents. Copper sulfate pentahydrate (99 %) crystallized and sodium hydroxide in pellets (98%) were acquired from Sigma-Aldrich (Darmstadt, Germany). Chemicals were used as received. Copper sulfate pentahydrate solution was prepared as follows. In an Erlenmeyer, 10 ml of deionized water was added, followed by the addition of 2.497 g of copper sulfate pentahydrate (0.35 mol.l^{-1}). The solution was stirred at room temperature until complete dissociation of the copper sulfate pentahydrate. Similarly, the sodium hydroxide solution was obtained by the addition of 0.400 g of sodium hydroxide (1.1 mol/l) to 10 ml of deionized water.

Precipitation of Copper hydroxide. In a small vial (Eppendorf tube), 1 ml of Copper sulfate pentahydrate solution was added. Afterward, the vial was placed in the beam. The Sodium hydroxide solution was connected to a peristaltic pump using a clear flexible tubing with an inner diameter of 190 µm (Tygon®). The other extremity of the tubing was connected to the vial. The chemical reaction was achieved by pumping the aqueous solution of sodium hydroxide into the vial with copper (II) sulfate pentahydrate solution with a flow rate of 10 µl/sec. The products of the reaction were the aqueous solution of sodium sulfate and the copper(II) hydroxide as a precipitate:

$$CuSO_4 * 5H_2O + 2NaOH \rightarrow Na_2SO_4 + Cu(OH)_2 \downarrow +5H_2O \tag{4.6}$$

During the precipitation of Copper hydroxide, X-ray projection were acquired to perform *in situ* X-ray imaging of the chemical reaction.

X-ray Imaging setup. X-ray imaging was performed at the IPS imaging cluster of the KIT synchrotron facility. Quasi-monochromatic X-rays with an energy of 17 keV and the energy bandwidth of 2 % were incident on the inverted Hartmann mask of 50 µm period and the duty cycle of 0.5; the area of the mask was 5 x 5 cm. The mask consisted of an array of square gold pillars with a height of 30 µm. The mask was placed 112 cm away from the detector. An Andor Neo 5.5 camera was imaging an X-ray scintillator (LuAG) by lens coupling (magnification of 2.73). The effective pixel size was 2.4 µm. Exposure time per frame was 0.5 sec with a frame rate of 1.5 Hz. The vial with copper sulfate pentahydrate solution was placed at 7.5 cm from the scintillator and connected to the pumping system located outside the FoV.

The schematic representation of the setup is illustrated in Figure 4.12. The X-rays were were passing through the inverted Hartmann mask, which introduced a periodic modulation to the wavefront. The periodically

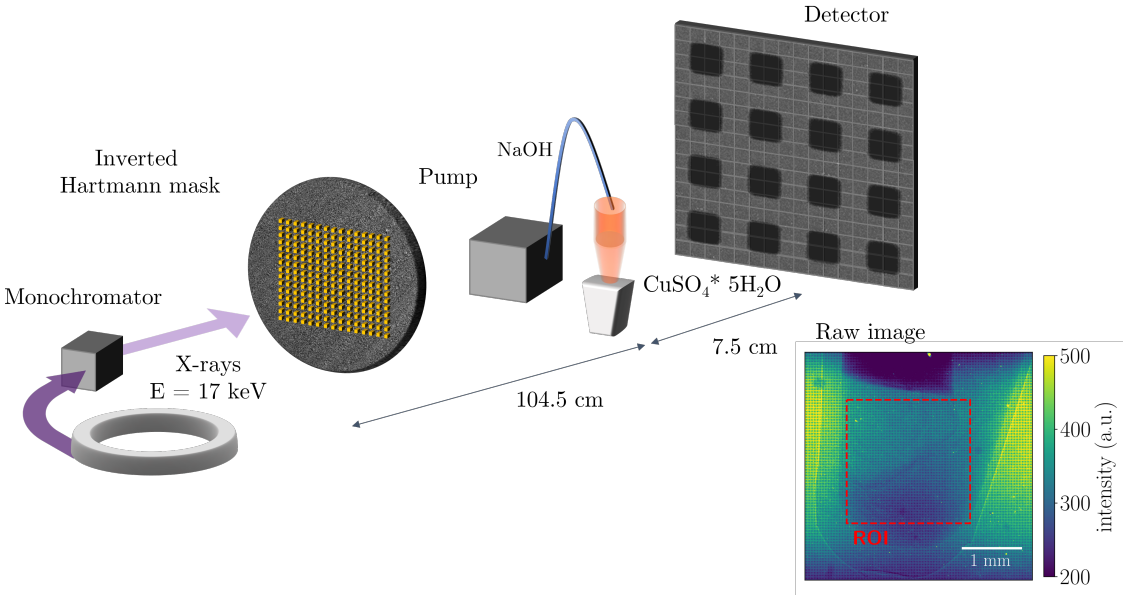

Figure 4.12: Experimental setup for *in situ* imaging of chemical reaction products by single-shot multi-contrast X-ray imaging with the inverted Hartmann mask. After passing through the monochromator with the spectral bandwidth of 2 %, the X-ray radiation had the central energy of 17 keV. The quasi-monochromatic X-rays were incident on the inverted Hartmann mask. A vial with the Copper sulfate pentahydrate solution was placed behind the mask. The Sodium hydroxide solution was injected into the vial using the peristaltic pump connected to it with a tubing.

modulated wavefront was incident on the vial containing Copper sulfate pentahydrate solution with NaOH being pumped into it at µl.sec^{-1} flow rate.

The retrieval of different contrast modalities was performed using the approach proposed by *Wen et al.*[20], which was shown to be robust with noisy data [29]. The data analysis was performed using the SH-WaveRecon wave reconstruction software [92]. The differential phase signals in two orthogonal directions were used to reconstruct the phase maps using the modified Southwell algorithm with ten iterations [93].

4.3.2.3 Results

Absorption contrast. From each snapshot of the overlaying object-mask projection, three contrast modalities were retrieved. The absorption image was obtained as the ratio of the magnitudes of the zero-order (central harmonic) images with and without the sample [20, 94]. The images obtained at measurement times 0, 25, and 113 s are shown in Figure 4.13. The line profiles in the images are on the right side of Figure 4.13. One can see how the absorption signal increases as the solid precipitate forms.

Differential phase contrast. The differential phase contrast (DPC) signal was retrieved by analyzing the shifts of the beam pattern in horizontal and vertical directions via the angle of the complex back-transformed first-order harmonics [29]. The DPC images show how the border from the solid precipitate forms. The profiles along the lines indicated in the images are plotted in Figure 4.14. One can see how the differential phase contrast grows with time in the indicated part of the vial. The formation of the solid precipitate changes the refractive index of the media, increasing the phase shift in the vertical direction. The phase-detection limit was 4 µrad. The angular resolution of the imaging setup can be improved by increasing the sample-to-detector distance.

Scattering contrast. The scattering images were obtained from the decrease in intensity of the first-order harmonic normalized by the central harmonic in the Fourier domain [94]. The scattering contrast shows

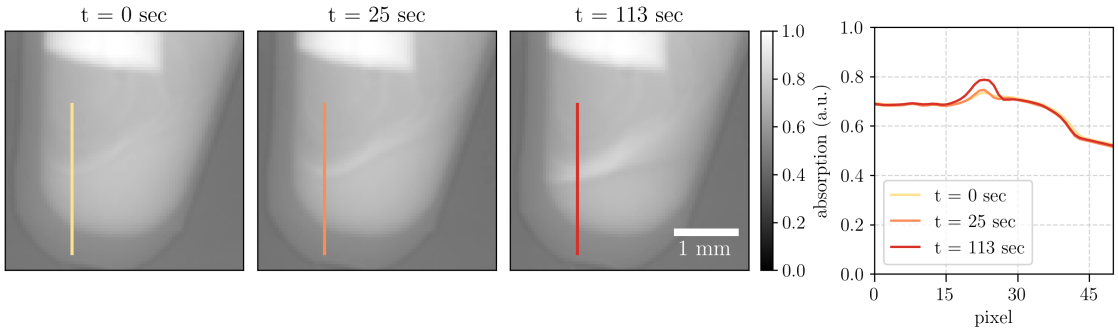

Figure 4.13: Absorption images for the measurement time t = 0, 25, and 113 s with the corresponding profiles along the indicated lines.

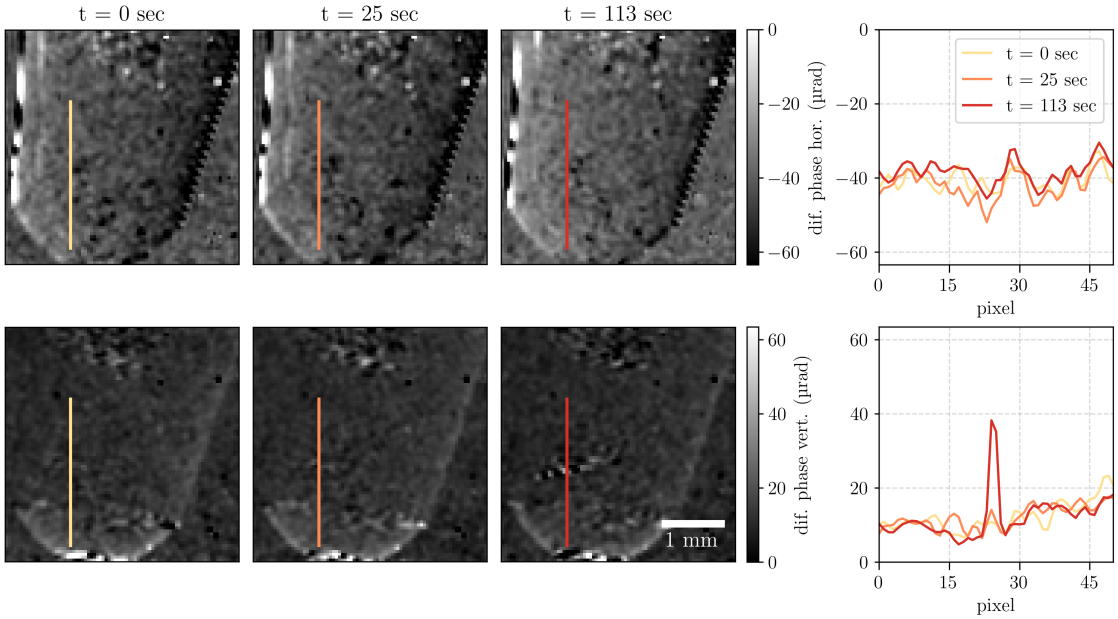

Figure 4.14: Differential phase images in two orthogonal directions for the measurement time t = 0, 25, and 113 s and the corresponding differential phase profiles along the indicated lines.

the signal from the unresolved features to be much smaller than the resolution of the imaging setup [2]. Scattering contrast images in two orthogonal directions are shown in Figure 4.15. The profiles along the lines indicated in the images are shown on the left. One can see that the profiles for scattering images do not change significantly with the measurement time. This might be because the small scatterers were already formed in the first seconds of the reactions that were not captured. Further reaction evolution with the precipitation of copper (II) hydroxide increases the number of pixels with a higher signal but does not significantly change the strength of the signal.

The unresolved absorption signal and the edge scattering can both contribute to the formation of the scattering contrast. The scattering signals obtained using Fourier analysis have been reported to exhibit the crosstalk correlation with the absorption signal due to the beam hardening for polychromatic sources [17] when the specimen exhibits high absorption [66]. This crosstalk can be neglected for the weakly absorbing microstructures; however, as the solid precipitate grows in volume, such signal pollution becomes more pronounced. For that reason, the linear decorrelation of the scattering signal and absorption was performed [29, 65]. After the decorrelation, we did not observe a substantial scattering signal pollution in the vertical direction, the direction of the strongest refraction signal for the formed precipitate. If the object under

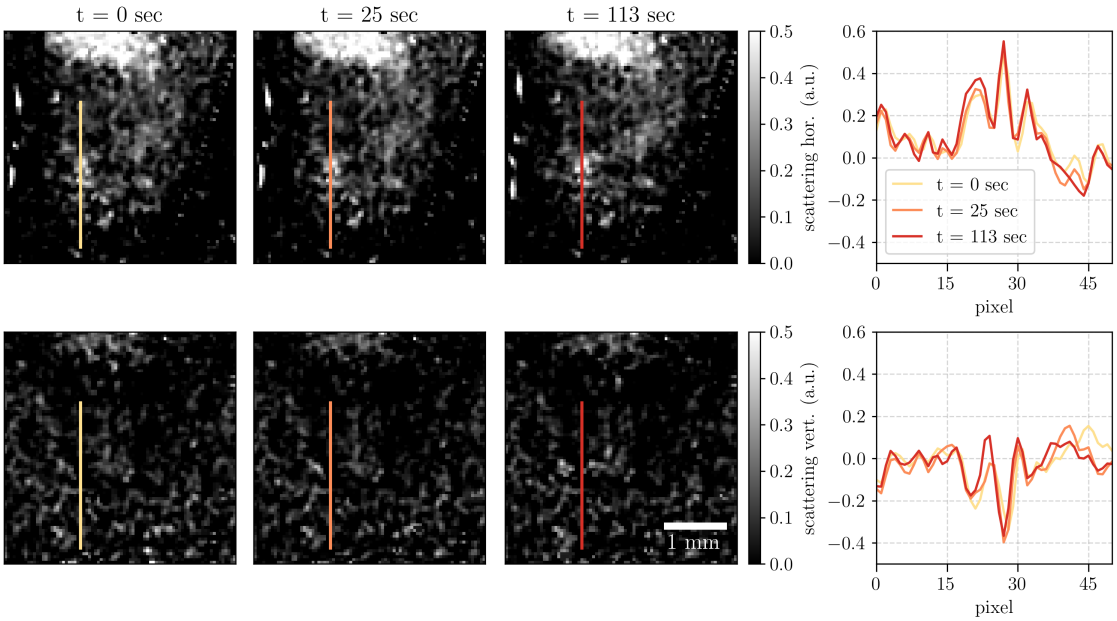

Figure 4.15: Scattering contrast images in two orthogonal directions for the measurement time t = 0, 25, and 113 s and the corresponding profiles along the indicated lines.

study induces strong edge scattering, the pollution of the scattering contrast can be suppressed using special algorithms reported elsewhere [66].

In Figure 4.15 one can see that there is still a significant signal preserved in the scattering images for strongly absorbing structures such as the pumping tubing, but the tubing is only visible in the horizontal scattering image. As the exact composition of the tubing is a trade secret, there might be several explanation to such strong direction-dependent scattering signal. The signal can be attributed to the unresolved differential phase signal as the curvatures of the tubing refract at the angles both resolved and unresolved by the imaging setup. Alternatively, the signal might be due to an internal structure in plastic, as some variants of the Tygon® tubing have multiple layers of different materials.

The finite resolution of the imaging setup performs spatial ensemble average. In our case, the spatial resolution of the final image is defined by the mask period P. The dampening of the contrast averaged over the mask's unit cell depends on the size of the scatterers presented in the sample [31]. The size sensitivity of the scattering contrast is defined by the setup organization [31]. The structure size probed in the setup is represented by the autocorrelation length $\xi = \lambda L/P$, where λ is the wavelength, P the mask period, and L is the distance from the object to the detector. For the setup (Figure 4.12) used in this experiment, the correlation length was 110 nm.

The scattering intensity can be interpreted in terms of the dark-field extinction coefficient (DFEC) [31], which defines the scattering intensity and is related to the autocorrelation function $G(\xi; D, \alpha)$ as [11] follows:

$$DFEC = \frac{3\pi^2}{\lambda^2}\phi|\Delta\chi|^2\left[1 - G(\xi; D, \alpha)\right]\frac{D}{\xi}, \tag{4.7}$$

where ϕ is the volume fractions of the scattering structure, $\Delta\chi$ the difference of complex refractive indices between the scattering material and the surrounding media, and D is the scattering structure size. The simplest form for the autocorrelation function corresponds to the model [95, 96], where signal fluctuations are treated like surface roughness:

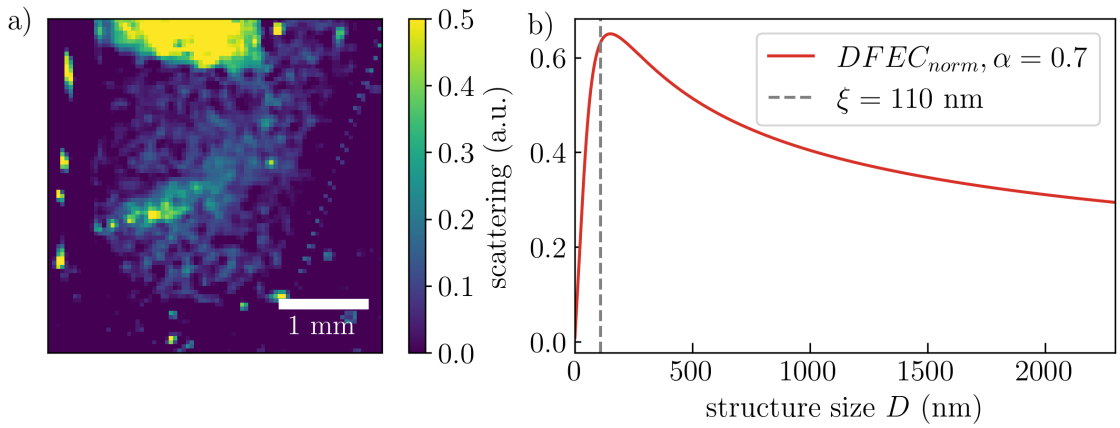

Figure 4.16: (**a**) Scattering contrast image at $t = 320$ s (sum over the two orthogonal directions); (**b**) the dark-field extinction coefficient (DFEC) calculated using Equation (4.7) for the autocorrelation function according to the simplest general model (Equation (4.8)) versus scattering structure size. The roughness exponent α was set to 0.7 as obtained for densely packed structures [12].

$$G(\xi; D, \alpha) = \exp\left[-\left(\frac{\xi}{D}\right)^{2\alpha}\right], \tag{4.8}$$

where α is the roughness exponent related to the fractal dimension of the scattering structure [96]. The roughness exponent α was calculated to be about 0.7 for densely packed structures [12]. We used the normalized DFEC $DFEC_{norm} = [1 - G(\xi; D, \alpha)]D/\xi$ to illustrate how the value of DFEC depends on the structure size (Figure 4.16b).

The scattering image obtained as a sum over the two orthogonal directions is shown in Figure 4.16a. The obtained values of the scattering signal are the average of the scattering intensity within the range of probed correlation lengths. As one can see from Figure 4.16b, the DFEC peaks close to the value of correlation length $\xi = 110$ nm, thus demonstrating that the highest input to the signal is coming from the structures with sizes about 100–200 nm (location of the peak). The largest scatterer, which still can influence the value of the scattering signal, can be estimated as $\xi_{max} \approx \lambda L/PS \approx 2.3$ µm, where PS is the effective pixel size of the imaging setup.

4.3.2.4 Discussion

Due to the technical restrictions of the setup, the pumping started several seconds before the image acquisition, such that a small amount of NaOH was already present in the tube. Thus, we performed the imaging of the course of the reaction but not its initiation.

The images for the three values of measurement time demonstrating the absorption, reconstructed phase, and the average scattering contrast are shown. One can see how each contrast modality illustrates the reaction evolution with time. As the aqueous sodium hydroxide solution is pumped into the copper(II) sulfate pentahydrate solution, the solid precipitate forms along the mixing line. The solid precipitate absorbs more X-rays than the aqueous solutions of reactants, which is reflected in the absorption contrast images. Copper (II) hydroxide has a different refractive index than the reagents. When a sufficient amount of the precipitate is formed, the difference in the introduced phase shift is detectable in the phase map. The average scattering contrast obtained from the scattering in two orthogonal directions illustrates the distribution of unresolved structures with sizes around 100–200 nm.

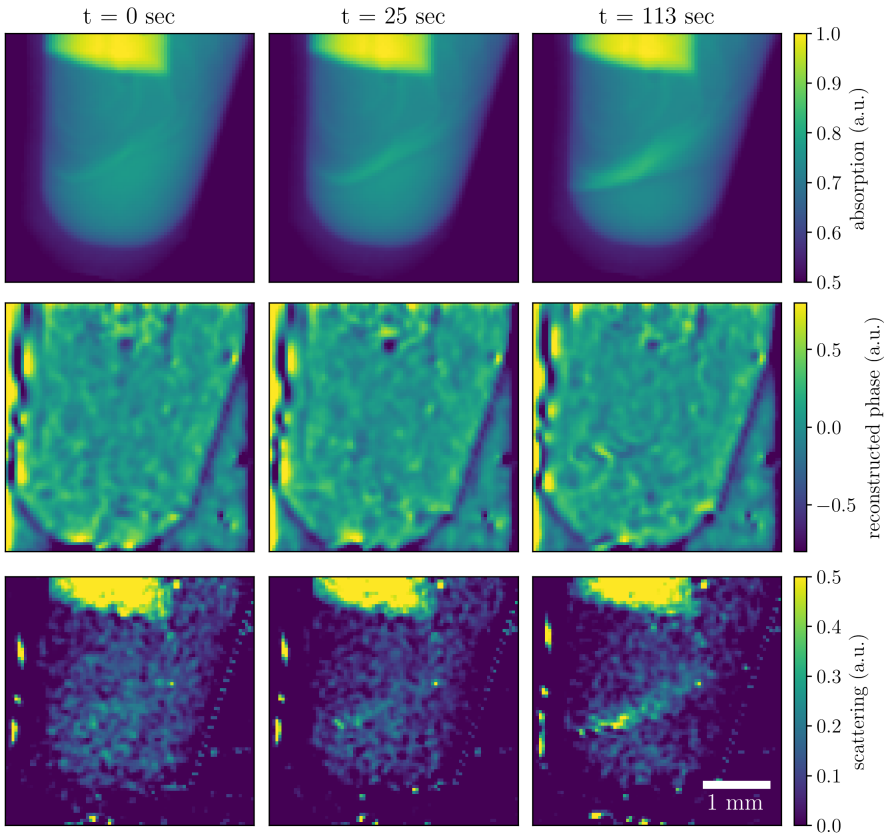

Figure 4.17: Absorption, reconstructed phase, and average scattering contrasts recorded at different measurement times (0, 25, and 113 s) illustrate the evolution of the chemical reaction.

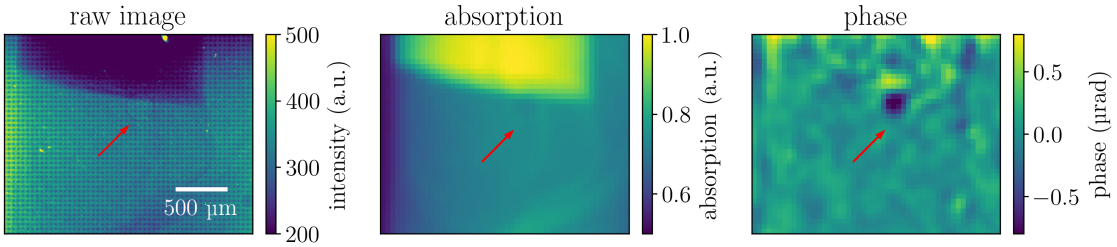

Figure 4.18: Raw, absorption, and reconstructed phase images in the area of an air bubble at t = 25 s. The arrow indicates the location of the bubble in the raw image.

The advantage of differential phase contrast for weakly absorbing structures can be clearly seen in Figure 4.18. It shows the cropped area of the air bubble pumped in the first second of the experiment. One can notice increased contrast on the bubble edges in the phase image in contrast to the raw and absorption images where it is barely visible.

We illustrate the evolution of the absorption and scattering contrast channels over the 320 s in Figure 4.19. The data points represent the mean value of signal intensity in ROI indicated in Figure 4.12. The data were smoothed using the Savitzky–Golay filter with a third-degree polynomial and a window of 21 data points. The formation of the precipitate occurred during the first 320 s of the measurement as indicated by the jumps in the absorption signal (25 and 113 s of the measurement) (Figure 4.19a). Then, the signal stabilizes after the precipitate is formed. The evolution of the mean scattering contrast during the measurement is shown in Figure 4.19b. The signal starts to increase after the first precipitate formation at the 25th until the 50th

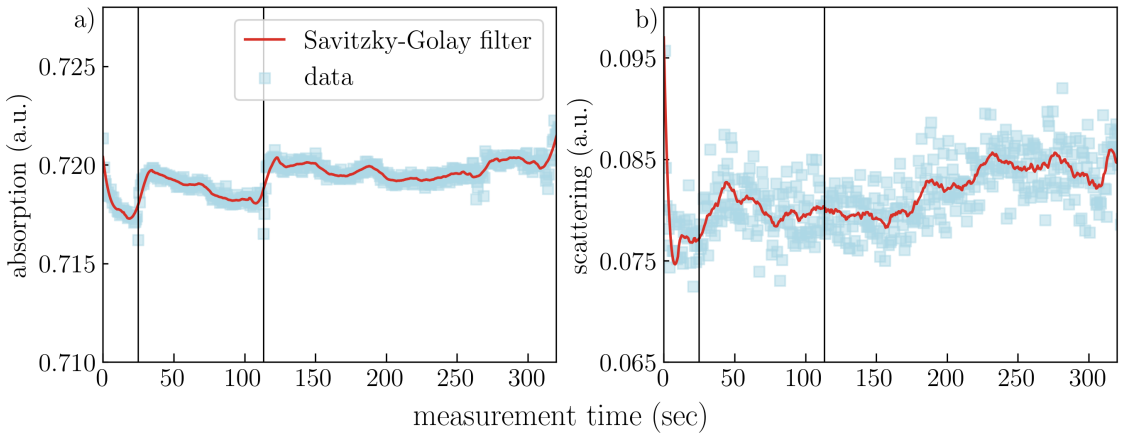

Figure 4.19: Evolution of the absorption (a) and scattering (b) contrast signals over the 320 s of measurement time. The data points represent the mean value of the signal in ROI (Figure 4.12), and the red line is the result of data filtering with the Savitzky-Golay filter with a third-degree polynomial and a window of 21 data points. The gray and black vertical lines indicate the 25th and 113th seconds, respectively.

second and then slightly decreases. The scattering contrast does not change significantly from 70 to 170 s and then starts to increase again. Note that there is no significant change in scattering signal, although the absorption signal shows the jump at 113 s. This implies that the volume fraction of scattering particles with sizes 100–200 nm keeps increasing, while the amount of resolved precipitate does not change significantly.

4.3.2.5 Conclusions

The single-shot multicontrast X-ray imaging setup used in this experiment allows for directly resolving the precipitates via absorption contrast and differential phase-contrast with the spatial resolution of 50 µm and the angular resolution of 4 µrad. Additionally, the scattering contrast enables tracking the submicron features. The formation of precipitate was completed after 130 s of the measurements, as seen from the stabilized absorption signal. The scattering signal continued to increase after forming a precipitate, indicating the increase in volume fraction of scattering structures with sizes of 100-200 nm. The short image acquisition time offered by single-shot X-ray imaging allows for monitoring of dynamic processes. Using brighter sources and detectors with a higher frame acquisition rate would further improve the time resolution.

The method is easy to implement and does not require a high degree of coherence. Flux-efficient inverted Hartmann masks are not susceptible to chromatic aberrations, enabling them to be used with polychromatic low-flux X-ray tubes. However, the adaptation to laboratory sources requires the special attention to factors such as the blur and magnification of the mask projection, which results in larger projected periods (lower spatial resolution). For such applications, the object-before-mask geometry of the setup can be advantageous. Moreover, the polychromaticity of the radiation can lead to the spurious signal in scattering images, which can be suppressed with the decorrelation algorithms [29, 66].

Hartmann masks are easy to handle and do not require precise alignment, making the setup flexible and straightforward to tailor for different applications. The single-shot multicontrast X-ray imaging with the inverted Hartmann mask can be used to study dynamic processes at different time scales. Only the source flux density and the detector frame limit the time resolution. Such a robust and flexible approach can have various applications in materials science and medical imaging.

5 Scattering contrast in multimodal X-ray imaging

5.1 Theoretical description of scattering contrast

The scattering contrast is associated with the signal coming from the structures well below the resolution of the imaging setup. The input from such structures decreases the contrast of the projected mask pattern. Such decrease in contrast have been observed in multiple phase-contrast imaging techniques and has been falsly attributed to the loss of coherence. However, the rigorous calculations aimed to find the origin of the decoherence and extinction contrast in linear shift invariant optical system done by Nesterets [40] have demonstrated that the decrease in the contrast of the phase images comes from the diffuse scattering introduced by the unresolved fine structures.

Nesterets applied the theoretical formalism within the wave-optical theory to propagation-based and analyzer-based X-ray imaging in order to explain the "decoherence effect" and "extinction contrast" which were observed experimentally in those two techniques, respectively [97, 98]. The observed low coherence component in the beam is not an actual loss of coherence, but rather the spatial ensemble average performed by the limited resolution, while the degree of coherence is actually preserved [99]. When the object contains features, which are much smaller than the resolution of the system, these features significantly affect the phase-contrast images by reducing the contrast of the resolved features, or the mask visibility in case of the imaging with Hartmann masks.

Following the approach of Nesterets, we can look at the imaging system with Hartmann masks like at the linear shift invariant (LSI) optical system, where so-called extinction contrast is observed because of the unresolved features present in the sample under investigations. A plane monochromatic wave $\exp(ikz)$ is incident on the object with transmission function $q(x) = \exp[-\mu(x) + i\phi(x)]$, where μ is the absorbance of the object and $\phi(x)$ is the phase shift. For simplicity, a one-dimensional object is assumed with transmission function changing in x-direction. The transmission function here consists of two types of features: smooth macroscopic features which are resolved by the imaging system (further denoted as $q_s(x) = \exp[-\mu_s(x) + i\phi_s(x)]$), and fine features ($q_f(x) = \exp[-\mu_f + i\phi_f(x))$ which are well below the resolution with a transmission function:

$$\begin{aligned} q(x) = \; & \exp[-\{\mu_s(x) + \mu_f(x)\}] \cdot \exp[i\{\phi_s(x) + \phi_f(x)\}] = \\ & \exp[-\mu_s(x) + i\phi_s(x)] \cdot \exp[-\mu_f + i\phi_f(x)] = \\ & q_s(x) \cdot q_f(x). \end{aligned} \tag{5.1}$$

The complex amplitude of the wave in the in the exit plane $E(x)$ is a product

$$E(x) = \exp(ikz) \cdot q(x) \tag{5.2}$$

In a setup with no optics the intensity of the wave is unity, which mean that no information on phase can be extracted. To tackle this, optical system can be introduced behind or in front of the object. LSI optical

system is characterized in real space by a complex propagator $P(x)$, which relates the complex amplitude of the incident wave to the exit wave.

If the optical system is behind the object (between the object and the detector), the complex amplitude of the wave at the detector plane is[1]

$$E(x) = \exp(ikz) \int \mathrm{d}x' P(x') q(x - x') \tag{5.3}$$

then the intensity in the detector plane $I(x) = E(x) \cdot E^*(x)$:

$$I(x) = \int \int \mathrm{d}x' \, \mathrm{d}x'' P(x') P^*(x'') q(x - x') q^*(x - x''). \tag{5.4}$$

This intensity would be obtained by the ideal system with delta-like resolution. However, the intensity distribution recorded by the imaging system is conditioned by its finite resolution (finite source size and the detector pixel size). This imperfection can be characterized by the point spread function of the system (PSF). The convolution of intensity $I(x)$ given by Eq. 5.4 with the $PSF(y)$ would result in the actual image recorded by the detector:

$$\tilde{I}(x) = \int \mathrm{d}y I(x - y) PSF(y) \tag{5.5}$$

Thus, the intensity in the image is

$$\begin{aligned} \tilde{I}(x) = & \int \int \mathrm{d}x' \, \mathrm{d}x'' P(x') P^*(x'') \int \mathrm{d}y PSF(y) q(x - y - x') q^*(x - y - x'') = \\ & \int \int \mathrm{d}x' \, \mathrm{d}x'' P(x') P^*(x'') \int \mathrm{d}y PSF(y) \\ & \times \exp[-\{\mu_s(x - y - x') + \mu_f(x - y - x')\}] \\ & \times \exp[-\{\mu_s(x - y - x'') + \mu_f(x - y - x'')\}] \\ & \times \exp[i\{\phi_s(x - y - x') + \phi_f(x - y - x')\}] \\ & \times \exp[-i\{\phi_s(x - y - x'') + \phi_f(x - y - x'')\}]. \end{aligned} \tag{5.6}$$

For simplicity let us assume a pure phase object. Then the exponential term with $\mu(x)$ will be equal to unity and by grouping $\phi_s(x)$ and $\phi_f(x)$ together we get

$$\begin{aligned} \tilde{I}(x) = & \int \int \mathrm{d}x' \, \mathrm{d}x'' P(x') P^*(x'') \int \mathrm{d}y PSF(y) \\ & \times \exp[i\{\phi_s(x - y - x') - \phi_s(x - y - x'')\}] \\ & \times \exp[i\{\phi_f(x - y - x') - \phi_f(x - y - x'')\}] \end{aligned} \tag{5.7}$$

If the unresolved fine features are randomly distributed and the average size is much smaller than the resolution of the imaging system represented by the width W of the PSF, the latter term can be well approximated by averaging around x [12, 40]:

$$\begin{aligned} & \overline{\exp[i\{\phi_f(x - y - x') - \phi_f(x - y - x'')\}]} = \\ & \frac{1}{W} \int_{-W/2}^{W/2} \mathrm{d}x \exp[i\{\phi_f(x - y - x') - \phi_f(x - y - x'')\}], \end{aligned} \tag{5.8}$$

[1] Here and further the integration is performed over the detector area, if not stated otherwise.

which depends only on the coordinates difference $\xi = x' - x''$ with $x - y$ being a parameter indicating that the statistics properties of the random phase $\phi_f(x)$ can vary within object. It is the function of the random phase induced by the unresolved features and will be further denoted as $S(\xi; x - y)$.

Then, the intensity in the image can be rewritten as

$$\begin{aligned}\tilde{I}(x) = & \int \mathrm{d}y PSF(y) \int\int \mathrm{d}x'\, \mathrm{d}x'' P(x') P^*(x'') \\ & \times \exp[i\{\phi_s(x - y - x') - \phi_s(x - y - x'')\}] \\ & \times S(\xi; x - y).\end{aligned} \tag{5.9}$$

If the phase shift $\phi_f(x)$ is random, it can be modelled as Gaussian random process [100], so as the phase difference. Then the autocorrelation function for such Gaussian process is the following:

$$\begin{aligned}S(\xi; x) = \overline{\exp[i\{\phi_f(x - y - x') - \phi_f(x - y - x'')\}]} = \\ \exp\{-\sigma^2(x)[1 - G(\xi; x)]\}.\end{aligned} \tag{5.10}$$

where $\sigma^2(x) = \overline{\phi_f^2(x)}$ is the random phase variance and $G(\xi)$ is the real-space autocorrelation function (projection of the autocorrelation funtion to the real space). Different forms of the real-space autocorrelation functions will be discussed in the following Section 5.1.1.

Generally speaking, the final image can be split into several components: resolution function of the image (PSF), absorption by the object, differential phase and a function of unresolved features, which constitutes the dark-field/scattering contrast. The absorption and the phase shift can be both retrieved by the procedures described in the previous chapters, and then the signal that is left after considering these inputs is the dark-field image.

This unresolved signal decays exponentially with the thickness [31] and size of the unresolved features. If the scattering structures are very small (much smaller than the angular width of the mask period expressed by $\lambda D/P$), the unresolved structures diffract in a large angular spread), and this only introduces a constant background. If the structures are of a compatible size with the angular width of the Hartmann mask (larger structures diffract in a smaller angular spread), their influence of the image intensity (contrast dampening) starts to be more pronounced. These calculations were further extended for Talbot interferometry by *Yashiro et al.* [12] and mask-before-sample geometry, where the assumption of the plane wave incident on the object is no longer valid [31]. However, the final result obtained by *Lynch et al.* is similar to the general approach of Nesterets.

The dark field extinction coefficient (DFEC) has been derived analytically for diluted hard monodisperse spheres in a homogeneous solution [31]

$$\mu_d = \frac{3\pi^2}{\lambda^2}\varphi|\Delta\chi|^2 \begin{cases} D - \sqrt{D^2 - \xi^2}\left(1 + \frac{1}{2}\left(\frac{\xi}{D}\right)^2\right) + \\ \left(\frac{\xi^2}{D} - \frac{\xi^4}{4D^3}\right)\ln\left[\frac{1-\sqrt{1-\left(\frac{\xi}{D}\right)^2}}{1+\sqrt{1-\left(\frac{\xi}{D}\right)^2}}\right], \text{ for } \xi < D; \\ D, \text{ for } \xi \geq D. \end{cases} \tag{5.11}$$

here the DFEC considered to be the coefficient such that scattering intensity S decays exponentially with the sample thickness t

$$S = e^{-\mu_d t}. \tag{5.12}$$

The link between the DFEC and the autocorrelation functions has been drawn by Strobl [11], where he demonstrated, that the DFEC can be expressed in terms of autocorrelation function of electron density according to the following equality

$$S = e^{-\mu_d t} = e^{-\Sigma[1-G(\xi)]}, \tag{5.13}$$

where Σ is the macroscopic scattering cross-section of the X-rays passing through the material under study. Macroscopic scattering cross-section is defined by the average number of times the X-ray get scattered when transversing the sample. It depends on the properties of the material and X-ray energy. It can be defined for the case of diluted hard monodisperse spheres as

$$\Sigma = \frac{3\pi^2}{\lambda^2}\varphi|\Delta\chi|^2 tD, \tag{5.14}$$

where λ is the wavelength, φ is the volume fraction of spheres, $\Delta\chi$ is the difference between the complex refractive indices of spheres and the solution, t is the sample thickness, and D is the sphere diameter.

Considering Eq. 5.13 and Eq.5.14, we can define the connection between the DFEC and the autocorrelation function as

$$\mu'_d = [1 - G(\xi)] \cdot d/\xi, \tag{5.15}$$

where μ'_d is the normaized unitless DFEC as defined in [31], $G(\xi)$ is the real-space autocorrelation function.

The approach where the real-space autocorrelation function $G(\xi)$ is related to the scattering intensity $S(\xi)$ as

$$S(\xi) = \exp\left[-\Sigma(1 - G(\xi))\right], \tag{5.16}$$

has been used in various works [11, 55, 101]. The advantage of this formalism is that the expressions for the autocorrelation function of electron density has been derived for spin-echo small-angle neutron scattering, and can be applied for the qualitative interpretation of scattering contrast.

5.1.1 Autocorrelation function

The scattering intensity depends on the autocorrelation function which has the general property of decaying from unity at $\xi = 0$ to zero when $\xi \to \infty$. The exact form of this function depends on the electron density fluctuations, which reflects the structure and the characteristic sizes of the object features. The simplest phenomenological model [95, 96] has been reported to be:

$$G(\xi) = \exp\left[-\left(\frac{\xi}{d}\right)^{\alpha}\right], \tag{5.17}$$

where α is related to to the phase boundary and interface roughness [40, 95, 96], d is the average scatterer size.

The real-space autocorrelation function according to Eq.5.17 is plotted in Figure 5.1a and Figure 5.1b. One can see that the increasing average size of the fine features d transforms the shape of the function making the decay to 0 with increasing ξ less steep. The change of the α-value also transforms the shape of the function but in the inverse way: $G(\xi)$ decays faster for larger α.

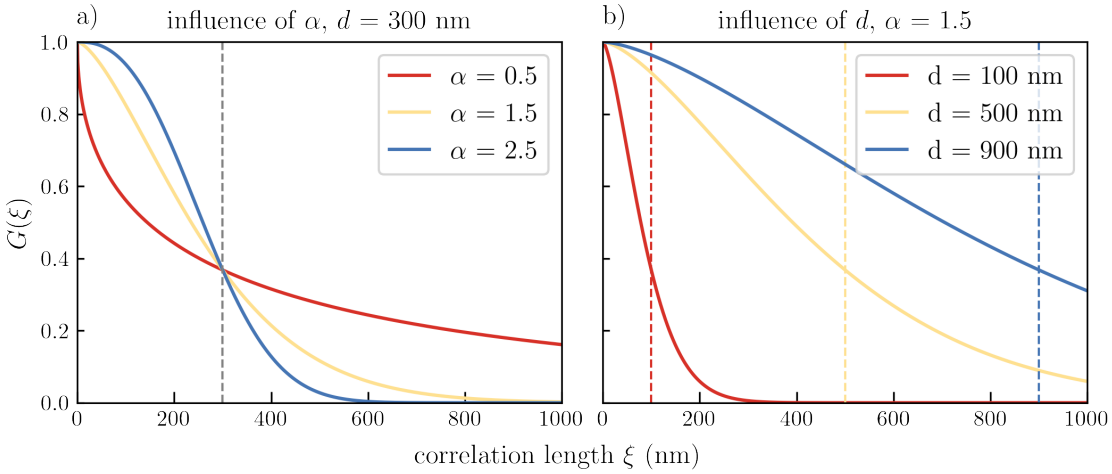

Figure 5.1: The real-space autocorrelation function, the simpliest model reported by *Sinha et al.* [95] Eq. 5.17: a) for different values of α, b) for different values of d (b).

The autocorrelation function for diluted hard monodisperse spheres (DHMS) have been reported [102] for SEANS measurements

$$G_{DHMS}(\xi) = \sqrt{1-\left(\frac{\xi}{D}\right)^2}\left(1+\frac{1}{2}\left(\frac{\xi}{D}\right)^2\right) + 2\left(\frac{\xi}{D}\right)^2\left[1-\left(\frac{\xi}{2D}\right)^2\right]\ln\left[\frac{\frac{\xi}{D}}{1+\sqrt{1-\left(\frac{\xi}{D}\right)^2}}\right], \tag{5.18}$$

where D is the sphere diameter and $0 \leq \frac{\xi}{D} \leq 1$.

In [31], theoretical model for the dark field extinction coefficient μ_d have been derived, which is the $\sigma^2(x) * (1 - G(\xi))$ in our terms. From the normalized dark field extinction coefficient $\mu'_d = \mu_d/\sigma^2(x)$ derived there as well, one can derive $G(\xi) = 1 - \mu'_d/D$. Then, the real-space autocorrelation function is presented as a piecewise function:

$$G_{DHMS}(\xi) = \begin{cases} \sqrt{1-\left(\frac{\xi}{D}\right)^2}\left(1+\frac{1}{2}\left(\frac{\xi}{D}\right)^2\right) + \\ \left(\frac{\xi}{D}\right)^2\left(1-\left(\frac{\xi}{2D}\right)^2\right)\ln\left[\frac{1-\sqrt{1-\left(\frac{\xi}{D}\right)^2}}{1+\sqrt{1-\left(\frac{\xi}{D}\right)^2}}\right], & \text{for } \xi < D; \\ 0, \text{ for } \xi \geq D, \end{cases} \tag{5.19}$$

which behaves identically to the Eq. 5.18 reported above: it equals unity at $\xi = 0$ and decays to 0 at $\xi = D$ (Figure 5.2).

Other form of the autocorrelation functions for different media have been defined for the SESANS measurements but are transferable to X-ray scattering. For example, dense but disordered structures can be characterized by the real-space autocorrelation function for random self-affine (RSA) density distributions [96, 103, 104]

$$G_{RSA}(\xi) = \frac{2}{\Gamma(H+1/2)}\left(\frac{\xi}{2a}\right)^{H+1/2} K_{H+1/2}\left(\frac{\xi}{a}\right), \tag{5.20}$$

where a is characteristic size parameter, $K_{H+1/2}(x)$ the modified Bessel function of the second kind of real order $(H + 1/2)$ and Γ the Gamma function. H is the so-called Hurst exponent ($0 < H < 1$) related to the dimensionality of the structure, namely to the interface roughness between the two phases of the material [105].

The Hurst exponent H from Eq. 5.20 reflects the space-filling capacity of the structure and defines its fractal dimension

$$D_f = D_E + 1 - H, \tag{5.21}$$

where D_E is the Euclidean dimension of the scattering structure: 1 for filamentous, 2 for sheet-like, and 3 for bulk scatterers [105, 106]. From this relation one can see that the value of the Hurst exponent reflects the fractal dimension and the specific surface area of porous material. Two domains are usually discussed: $H > 1/2$ indicating that the density distribution is persistent (long-range correlations) with smoother and more interconnected pores, and $H < 1/2$, which corresponds to antipersistent distributions with smaller and more confined pores and low permeability [107].

The characteristic size of the structure d for random two-phase media can be understood as the average pore size and is derived from the size parameter a and the Hurst exponent H as follows [104]

$$d = \frac{2\sqrt{\pi}a\Gamma(H + 1/2)}{\Gamma(H)}, \tag{5.22}$$

where Γ is a gamma-function. If the values of H and a are determined by fitting the experimental data, then the error for the average size of the structures is defined from the partial derivatives of ξ as the error of indirect measurements

$$\Delta_d = \sqrt{\left(\frac{\partial d}{\partial a} \cdot \Delta_a\right)^2 + \left(\frac{\partial d}{\partial H} \cdot \Delta_H\right)^2} = \frac{2\sqrt{\pi}\Gamma(H + 0.5)}{\Gamma(H)} \times \sqrt{(\Delta_a)^2 + \left(\left[\psi^{(0)}(H + 0.5) - \psi^{(0)}(H)\right] \cdot \Delta_H\right)^2}, \tag{5.23}$$

where $\psi^{(0)}$ is the digamma function.

5.2 Data analysis approaches

5.2.1 Decrease in visibility

If periodic structure is used to produce the wavefront modulation, then the presence of the sample with scatterers below the resolution of the imaging setup will result in the dampening of visibility of the mask relative to the reference image. The reference image is the projection of the mask without the object in the beam path. Thus, if relative decrease in visibility defines the scattering intensity, the scattering contrast S can be defined as

$$S = -\ln\left(\frac{V}{V_0}\right) \tag{5.24}$$

where V is the measured mask visibility with the sample in the beam path and V_0 is the mask visibility in the reference image. The visibility is defined for each unit cell of the mask and shows the difference between

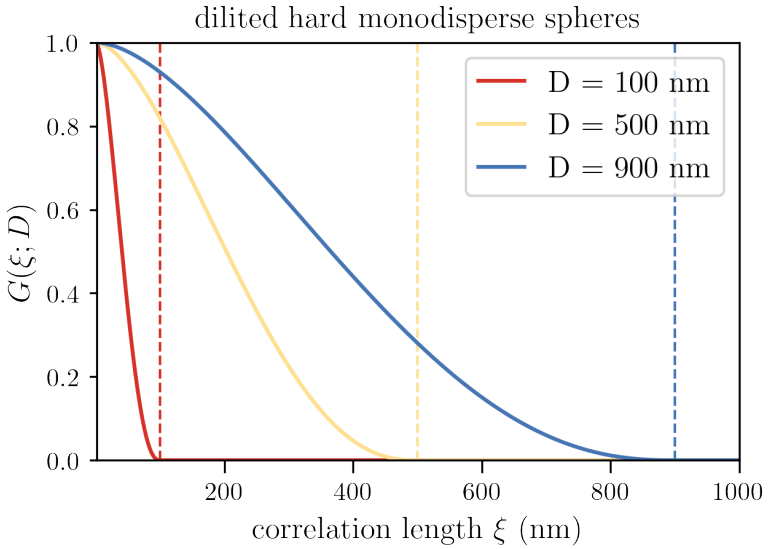

Figure 5.2: The real-space autocorrelation function for diluted hard monodisperse spheres for different diameters D as indicated in the legend. Note that the autocorrelation funciton decays to 0 at $\xi = D$.

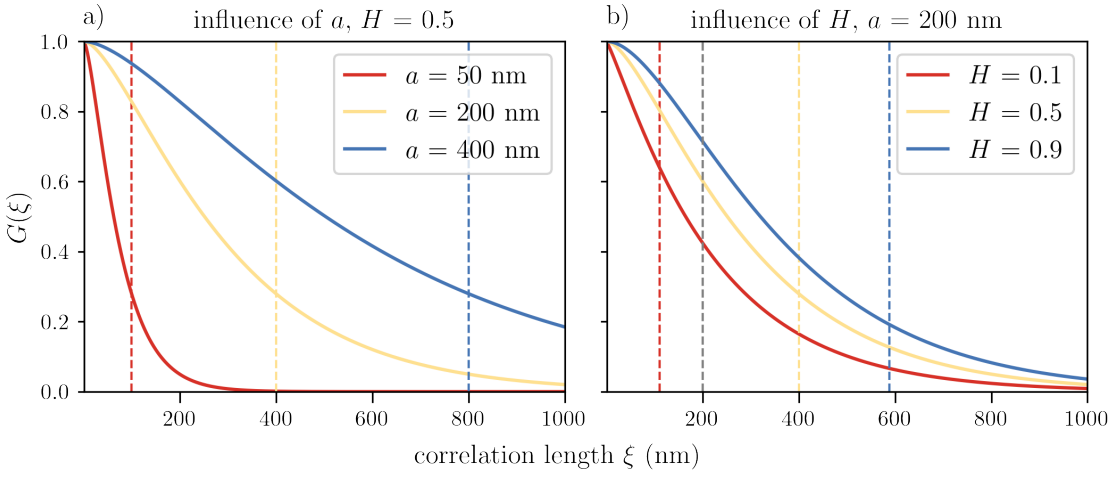

Figure 5.3: The real-space autocorrelation function for self-affine distribution: a) with the value of Hurst exponent $H = 0.5$ (perfectly random solid) for different values of characteristic sizes a and average size d; b) with characteristic size a = 200 nm for different values of Hurst exponent H. The average structure size d is marked by the dashed lines.

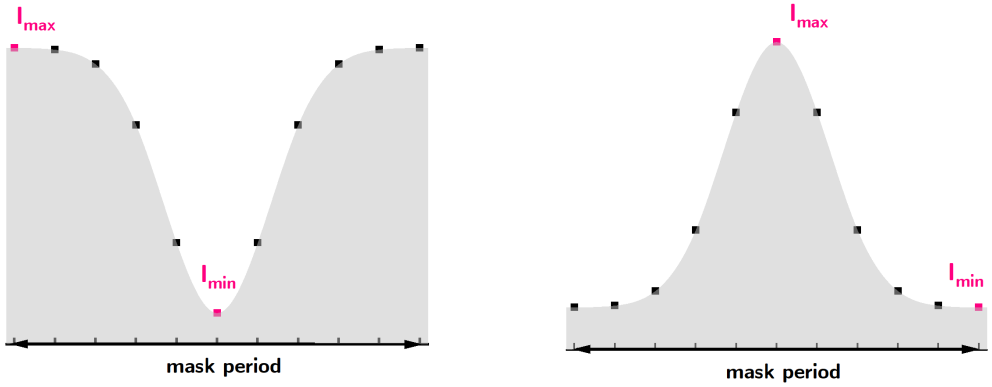

(a) conventional Hartmann mask

(b) inverted Hartmann mask

Figure 5.4: Schematic representation of how the visibility of mask pattern is evaluated.

the intensity behind the absorbing structure and the intensity recorded behind the transmitting substrate. It is commonly defined as

$$V = \frac{I_{max} - I_{min}}{I_{max} + I_{min}} \tag{5.25}$$

where I_{max} and I_{min} are the maximum and minimum intensities detected in the unit cell of the Hartmann mask. The illustration of this approach for conventional and inverted Hartmann masks is shown in Figure 5.4.

5.2.2 Width of the individual beamlets

The periodic modulation introduced by the Hartmann mask can be treated as a set of Gaussian distributions [17, 64]. Then each beamlet (unit cell of the mask) can be individually fitted by a two-dimensional Gaussian distribution according to

$$g = o + h \cdot \exp\left\{-\frac{1}{2}\left[\left(\frac{x - x_0}{w_x}\right)^2 + \left(\frac{y - y_0}{w_y}\right)^2\right]\right\}, \tag{5.26}$$

where o is offset (the average value of the corner pixels), h height of the Gaussian (maximum intensity with subtracted offset), x_0 peak position in x-direction, y_0 peak position in y-direction, w_x width in x-direction, w_y width in y-direction (Figure 5.5). The peak positions can be estimated as the center of mass (first image moment), the width represents the variance of the data in horizontal and vertical directions and can be calculated as the second image moments. Then, the least-square fitting of the two-dimensional Gaussian distribution according to Eq. 5.26 [29, 65].

If the reference projection of the undisturbed mask pattern is recorded, transmission contrast can be defined as $T = h/h^{ref}$, phase shift in two directions is the change in the peak position coordinates $x_0 - x_0^{ref}$ and $y_0 - y_0^{ref}$. The widths w_x and w_y are the changes in full width at half maximum of the Gaussian and can serve as a direct measure of the scattering intensity

$$S_x = w_x - w_x^{ref} \quad \text{and} \quad S_y = w_y - w_y^{ref}. \tag{5.27}$$

The advantage of multi-Gaussian fitting for two-dimensional optical elements such as Hartmann masks is that the scattering can be detected in two orthogonal directions x and y. Such approach is very attractive because it allows to study microstucture parameters in two directions. It has also been reported to be less

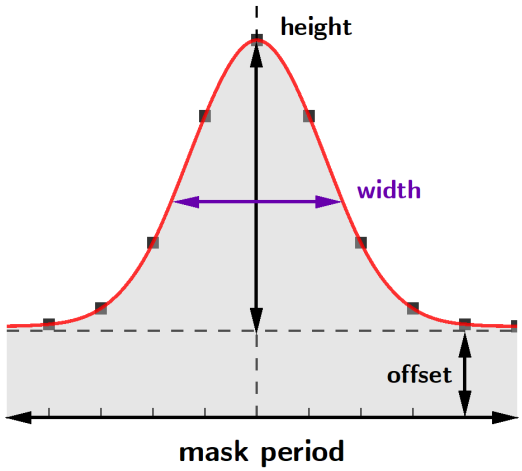

Figure 5.5: Schematic representation of the Gaussian fitting of mask projection and the outline of the derived parameters. For simplicity, a one-dimensional Gaussian is illustrated.

susceptible to the cross-talk between absorption and scattering contrast [64]. However, it has also been noted [65] and confirmed in this work that such approach is very susceptible to noise, especially for low mask projection sampling rates (N_{pix}) or detector imperfection (dust, hot or dead pixels, etc.). Besides, it has been reported that high transmission changes within the beamlet zone can lead to errors in both scattering and differential phase signals [65]. These drawbacks can be mitigated by pre-filtering of the images before the fitting, but it complicates the data analysis and questions the reliability of the results. However, if there is no strong changes in transmission and the visibility of the mask is not too low (higher SNR), it can be used as an intuitive and useful approach to evaluate the scattering contrast.

Besides, in such setting it is also possible to define visibility as [65]

$$V_G = \frac{h}{h + 2 \cdot o}, \tag{5.28}$$

because the height of the Gaussian h is nothing else but the maximum intensity I_{max} with the subtracted noise defined by the offset o, and which is equal to I_{min}. Thus $I_{max} = h - o$ and $I_{min} = o$ (Figure 5.5).

5.2.3 Intensity of the higher order harmonics in Fourier domain

As have been discussed in Chapter 2, Fourier analysis can also be used to evaluate the scattering contrast from the changes in higher order harmonics. Usually the first order harmonics with $(m, n) = (1, 0)$ and $(0, 1)$ are analysed, which represent the horizontal and vertical directions, respectively, because the signal intensities decrease at higher orders in Fourier space due to the counting statistics. However, it has been proposed that the higher orders are sensitive to larger scatterers [94], which was later confirmed by simulations [65]. This makes it possible to differentiate between different sizes by using higher orders. This approach has been experimentally implemented for single-shot scattering imaging for arrays of Fresnel zone plates [101]. While interesting, this approach suffers from the low correlation length sampling defined by the number of pixels per mask period. The higher sampling rates thus can be achieved by using detectors with small pixel size or mask with large periods. There are trade-off to both approaches. Using smaller pixels seems more advantageous because then the final image size can be preserved. However, the available pixel size is limited and the detectors with smaller pixel sizes usually have small field-of-view. Using larger mask periods will reduce the final image size, thus lowering the resolution of macroscopic imaging.

It has been reported that such approach can lead to the strong spurious scatter signal due to the cross-talk between these two signals [64]. The Fourier analysis method implicitly assumes that intensity without the sample is the product of transmission and the intensity with the sample when only absorption is considered. This assumption holds true for monochromatic radiation, however, when polychromatic sources are used and the sample exhibits high absorption, a special attention should be paid to the possible cross-talk between the scattering and absorption due to the beam hardening [64, 66].

5.3 Scattering from porous media

The form of the real-space autocorrelation function depends on the structural organization of the material (see Section 5.1.1). While several experimental studies [31] confirmed that the formula for diluted monodisperse particles correctly predicts the scattering signal obtained from such structures. Although the equivalence of dark field extinction coefficient and the autocorrelation function formulas derived for neutrons have been highlighted [11], there have been limited attempts to benefit from it and derive multiple quantitative characteristics of bulk morphology for dense materials of different structural organizations. The simplified phenomenological formula proposed by *Sinha et al.* [95] has been applied to derive the size of scattering structures [12, 55, 108], but there have been few attempts to derive quantitative parameters related to the scatterers spatial distribution and orientation [12, 108].

Porous materials are widely applied as adsorbers, thermal insulators, catalytic and electrode materials, etc. Bulk microstructure is of great importance to study because it defines the physical, chemical, thermal, and electrical properties of porous materials. However, porous materials are challenging objects for characterization: they typically exhibit a wide range of pore sizes, solid material opacity, possible anisotropy of the pores, and structure inhomogeneity in bulk. While the fine nanostructure of the sample can be studied by precise methods such as SAXS, the range of pores from several tens up to several hundreds of nanometers is challenging to study. Conventionally applied for these ranges microscopic techniques have a limited field of view which often makes the characterization they offer confined and incomprehensive. Moreover, they are often either used for the surface characterization or are destructive, which might be a critical limitation.

Scattering contrast offered in multimodal X-ray imaging has the advantages of covering a large field of view and the simple and flexible setup. Due to size-sensitivity of the scattering signal the range it covers lays between the range accessible in SAXS and the resolution of X-ray imaging, thus covering the gap between those techniques. In order to test this approach, the fine porous graphite was chosen as an object for characterization due to the wide range of pores presented and low X-ray absorption, which allows us to assume a pure scattering object with structures smaller than the resolution of the setup and no strong phase shifts due to the absence of border and interfaces which would contribute to the resolved differential phase contrast. The sizes of the pores for fine grade graphite is usually in the sub-µm range and is represented by a wide range of pores, which makes it a perfect candidate to illustrate the capabilities of the scattering contrast in multimodal X-ray imaging.

Another advantage of using graphite is that due to its conductivity and a high specific surface area it can be used as a substrate for UV lithography, thus making it possible to manufacture the Hartmann masks directly on its surface. In this case, the Hartmann mask will have the highest visibility and flux efficiency, which is important for the setups with a monochromatic beam which usually have lower intensity.

In this section, I will compare the scattering data for graphite with fine pores achieved with conventional and inverted Hartmann mask designs. The quantitative analysis of the scattering data will be verified by the specifications provided by the manufacturer. The additional surface pore size distribution analysis was

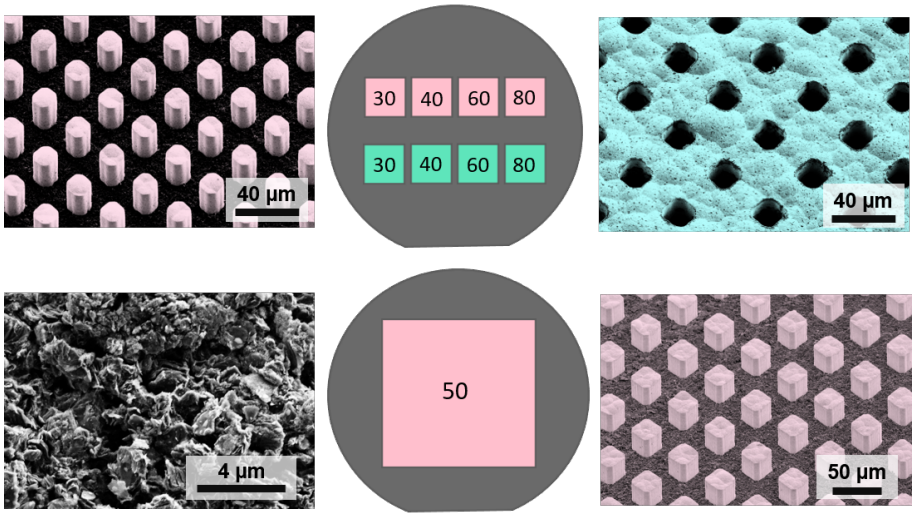

Figure 5.6: Outline of the wafers used for experiment with SEM images of the masks and the graphite wafer surface. In SEM images the masks were rotated to 45° for better visualization. Inverted Hartmann mask areas are denoted as pink squares and Hartmann masks as green squares with periods 30, 40, 60, 80 μm. The rows of pillars/holes are alighted parallel to the flat edge of the wafer. On the first wafer, all the areas of the masks were 1 cm^2. The inverted Hartmann mask with 50 μm period and area of 25 cm^2 was manufactured on a separate wafer.

performed based on SEM images to compare the obtained data with the resolved images of the surface structure. The chapter includes the comparison of different data retrieval algorithms to the conventional visibility map calculation approach, and will explore the directional information offered by the Hartmann masks. Moreover, I propose an approach to estimate the pore size distribution based on the parameters retrieved from the fit of the experimental data.

5.3.1 Sample

The wafers purchased from Ohio Carbon Blank, Inc were synthetic graphite labeled "angstrofine" with a porous structure and an average grain size of 1 μm as reported by the supplier (supplier identifier EDM-AF5) [109]. The apparent density of the EDM-AF grade graphite material is reported to be 1.8 g/cm^3 [110] . Since the apparent density measurements include the pore volume in the calculation and the theoretical density of graphite is 2.26 g/cm^3, the pore fraction of graphite is at least 20 %. The average pore size for the graphite with an apparent density of 1.8 g/cm^3 is 750 nm ± 150 nm as observed by mercury porosimetry [111]. The distribution of pore sizes for EDM-AF grade graphite is narrow compared to conventional graphite with reported nominal pore size rating from 0.2 to 0.8 μm [111]. The separate wafers with 4 inch diameter were cut out of the large graphite plate. Subsequently the wafers were polished on both sides and rinsed in isopropanol.

The technological process of fabricating Hartmann and inverted Hartmann masks was reported in the Chapter 3. Inverted and conventional Hartmann masks of various periods (30, 40, 60, and 80 μm) with the gold height of about 30 μm manufactured on the same substrate and a large area (5 cm x 5 cm) inverted Hartmann mask were used Figure 5.6. The masks will be further referred to as "Mask type-Period", e.g. iHM-30 for the inverted Hartmann mask of period 30 μm and HM-30 for conventional Hartmann mask of period 30 μm.

5.3.1.1 Surface pore analysis

In addition to the characteristics provided by the supplier, we obtained information about the surface pore size distributions based on the set of SEM images (Figure 5.7). The images were taken at different magnifications (5000X and 20000X). The lower magnification images were used in order to compensate for small field of view of the SEM and cover a representative surface, and higher magnification was applied to correctly mark the pores of smaller sizes. The pore distribution data from several images were merged in order to achieve higher statistics. The images were binarized using thresholding procedure.

The pores where identified using *Analyze particles* function in ImageJ. Identified pore areas were approximated by ellipses, and then the Feret's diameter was calculated as the longest distance between any two points along the selection boundary (maximum caliper diameter). The pore size distribution histogram was fitted with log-normal distribution function. The mode of the distribution was at 585 nm. One can see from the cumulative histogram that more than 60 % of the pores are below 800 nm in agreement with the nominal pore size rating reported for graphite wafers of EDM-AF grade.

Based on a set of SEM images (examples in Figure 5.7 and Figure 5.8(a)), we performed surface pore size analysis. We identified the pores on the images by thresholding. Then, we estimated their Feret diameter (the longest distance between any two points along the selection boundary) to obtain the pore size distribution histogram (Figure 5.8(b)). The histogram follows a log-normal distribution with the peak at 550 nm. One can see that more than 60 % of the pores are below 800 nm, which is in agreement with the nominal pore size rating reported for graphite wafers of EDM-AF grade [111].

5.3.2 Experimental setup

In the reported method we attribute the decrease in visibility to the ultra small angle X-ray scattering in graphite. However, the imperfections of the setup can also cause a possible decrease in the visibility during sample and optical element movement, because the source size and the source-sample distance are both finite. Large source size (opposite to the point-like source) will cause penumbral blur, and the insufficient distance between the source and the sample will contradict the parallel beam geometry assumption because of the beam divergence. We analyzed the setup characteristics to ensure that the assumptions of point-like source and parallel beam are valid for the performed measurements.

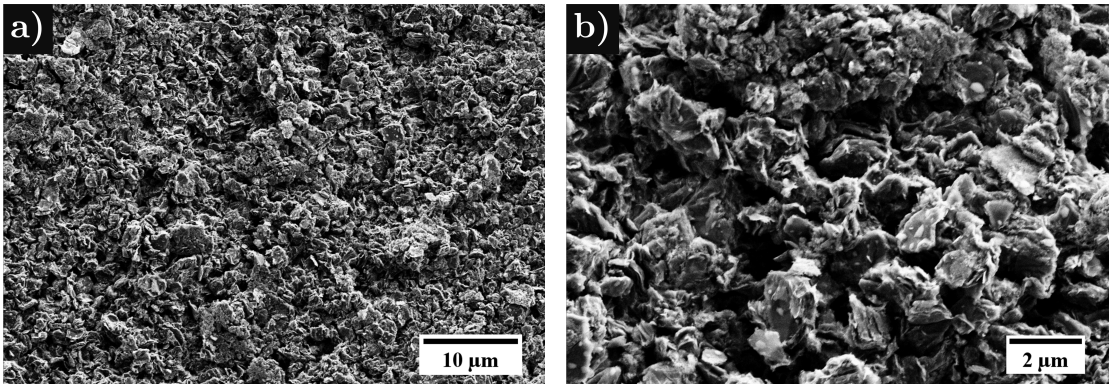

Figure 5.7: SEM images of graphite surface: a) overview with lower magnification (5000X), b) close up view with higher magnification (20000X).

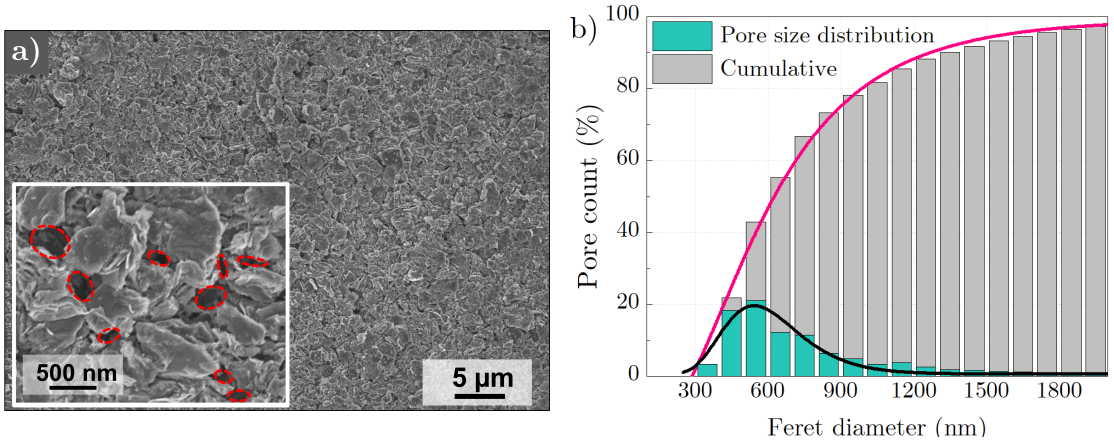

Figure 5.8: The surface structure of graphite: a) SEM image of graphite surface with a close-up view outlining the pores in red; b) surface pore size distributions histogram (green) and cumulative pore number (gray) versus Feret diameter based on the SEM image analysis.

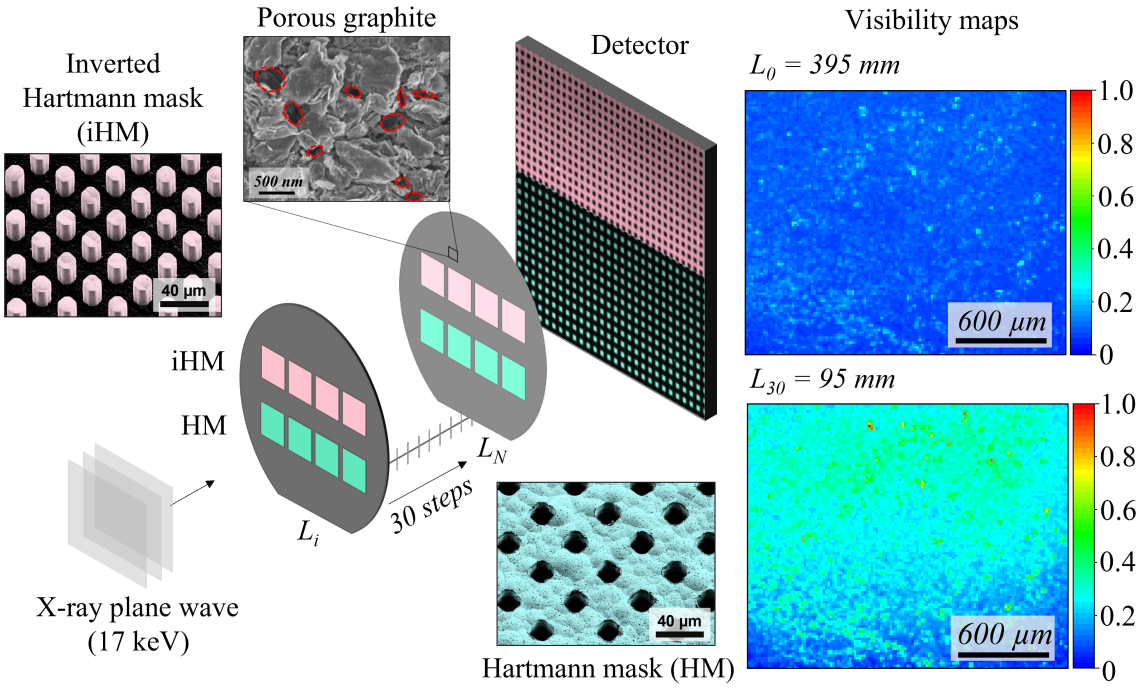

Figure 5.9: Experimental setup for visibility measurements. Monochromatic X-rays are incident on the mask, which is moving towards the detector with steps of 10 mm. The measurements were done with inverted and conventional Hartmann masks of different periods produced on porous graphite. For each step, a projection is recorded from which the visibility map is plotted. The visibility maps for two distances are shown in the right part of the graph.

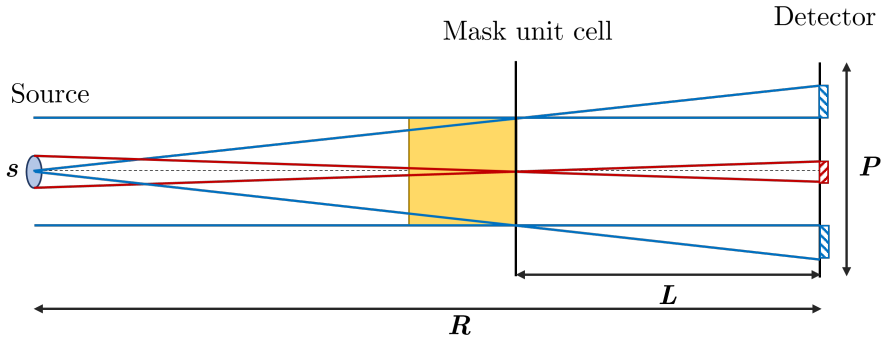

Figure 5.10: Schematic representation of blur of the mask image induced by the finite source size (red lines) and deviation from the parallel-beam geometry (blue lines) for the horizontal direction (not to scale). The source with the size s is located at the distance $R \approx 30$ m from the detector, the maximum mask-detector distance is $L = 0.395$ m, and the period of the mask is denoted as P. Here, the pillar of the inverted Hartmann mask is shown, however, the same considerations are valid for the conventional Hartmann mask.

5.3.2.1 Source blurring

At the IPS imaging cluster of the KIT synchrotron facility (TOPO-TOMO beamline), the horizontal source size (800 µm) is larger than the vertical (200 µm). Therefore the blurring caused by the finite source size is stronger in the horizontal direction. The most substantial blur will occur at the largest mask-detector distance; thus, we consider conditions for horizontal direction and the largest mask-detector distance as the limiting factor. The mask-detector distance of 0.395 m was the largest for all masks but iHM-50, for which the maximum mask-detector distance was 1.12 m. The maximum blur of the projection at the detector plane due to the finite source size can be defined as

$$B_{max} = s_{hor} \cdot \frac{L}{R-L} \approx s_{hor} \cdot \frac{L}{R}, \tag{5.29}$$

where s_{hor} is source size in the horizontal direction, L is object-detector distance, R is source-detector distance (Figure 5.10).

For the maximum blur to affect the visibility map, it has to be larger than the mask period P (which is the pixel size at the final visibility map image) so that the minimum intensity value is increased, making the visibility value lower. For the masks with periods 30, 40, 60, and 80 µm, the maximum blur is 10 µm, and for the iHM-50 placed at 1.12 m from the detector, the blur is 30 µm (Table 5.1). In both cases, the blur is smaller than the corresponding mask period; thus, it does not significantly affect the mean visibility value.

5.3.2.2 Beam divergence

Another important factor to possibly affect the visibility is the beam divergence: the deviation of the rays from the parallel geometry. The maximum deviation from the parallel-beam projection is observed for the outermost pillar/hole position (Figure 5.10). The deviation can be neglected if it is smaller than the effective pixel size (PS) of the detector (pixel size of the final image). From the scheme in Figure 5.10 one can see that the size of the deviation can be defined as

$$deviation = \frac{P \cdot L}{R} < PS. \tag{5.30}$$

which leads to the restriction on the mask period

$$P < \frac{PS \cdot R}{L}. \tag{5.31}$$

One can see that for the pixel size $PS = 2.36\ \mu m$, distances $L = 0.395\ m$ and $R = 30\ m$, the requirement on the mask period is

$$P < \frac{2.36 \cdot 10^{-6} \cdot 30}{0.395} \approx 180\ \mu m. \tag{5.32}$$

This condition is fulfilled for all masks used in the experiment. For the iHM-50, which was placed at the distance $d = 1.12$ m, the same condition holds true, but by a smaller margin:

$$P < \frac{2.36 \cdot 10^{-6} \cdot 30}{1.12} \approx 63\ \mu m. \tag{5.33}$$

Therefore, the divergence of the beam did not significantly affect the mean visibility value acquired in the experiment.

Alternatively, this criteria can be formulated as dimensionless ratio imposing a restriction on the number of pixels per mask period N (sampling of mask projection)

$$N < R/L \tag{5.34}$$

As one can see from the values presented in Table 5.1, the inequality given by Eq. 5.34 holds true for all measurements.

5.3.2.3 Energy bandwidth and the correlation length error

The measurements were performed for the energy 17 keV with bandwidth $\Delta E/E \approx 2\%$, $E = 17 \pm 0.34\, keV$. The correlation length value ξ depends on the energy as:

$$\xi = \frac{hc}{E} \cdot \frac{L}{P} \tag{5.35}$$

The error of the indirect measurement for ξ will be defined as:

$$\Delta_\xi = \sqrt{\left(\frac{\partial \xi}{\partial E}\Delta E\right)^2} = \sqrt{\left(-\frac{hc \cdot L}{P \cdot E^2}\Delta E\right)^2}. \tag{5.36}$$

The maximum error due to the bandwidth $\Delta E/E$ is $\Delta_\xi = 33\ nm$ and is reached for the longest mask-detector distance $L = 1.12\ m$ and the $P = 50\ \mu m$. For the distance $L = 0.395\ m$ the highest error $\Delta_\xi \approx 20\ nm$ corresponds to the smallest period $P = 30\ \mu m$ (Table 5.1). Such small errors do not affect the fitting parameters derived from the data.

5.3.3 Scattering intensity via standard visibility

5.3.3.1 Results

The visibility maps were calculated using the projection images of the masks at different distances to detector (thus, different probed correlation lengths). For each projection in the unit cell of the mask maximum and minimum intensity have been evaluated according to Eq. 5.25. The mean values of the visibility maps for

Table 5.1: Setup criteria for plane wave assumption.

Period (μm)	L-range (mm)	B_{max} (μm)	N	R/L	ξ-range (nm)	Δ_{ξ}^{max} (nm)
30	95-395	10	13	75	231 - 960	19
40	95-395	10	15	75	173 - 720	14
50 [2]	95-395, 1120	30	20	26	139 - 576, 1634	33
60	95-395	10	25	75	115 - 480	10
80	95-395	10	31	75	87 - 360	7

[2] Only iHM

each mask versus the probed correlation length are presented in Figure 5.11 (green for HM and pink for iHM). The error bars are the standard deviations of intensity in the visibility map.

One can see that visibilities of conventional Hartmann masks were higher than for the inverted Hartmann masks for all measurements. An explanation could be that for iHM the area covered with gold (and thus, behind which most of the X-rays are attenuated), is smaller, and thus the effective area of the sample, which impacts the final signal, is larger. In case of highly scattering objects, like graphite, it leads to a stronger dampening of the measured visibility. The values of visibilities for HM and iHM are different, but the trend they follow with changed sample-detector distances is the same. In Figure 5.11 one can see the curvature which reflects the non-linear dependence of the scattering intensity from the probed correlation length.

Albeit each mask was moved in the same way (same L-range and same number of sampling steps), the spanned range and the scanning step of probed correlation lengths is different due to the different period of the mask (Eq. 2.16). The period of 30 μm (HM30, iHM30) offers a wide range of probed correlation lengths (Figure 5.11), while for the P = 80 μm (HM80, iHM80) the ξ-range is quite narrow. The advantage of using larger mask periods is that smaller values of correlation length can be reached, although for the samples with scatterers of various sizes using smaller periods can be preferred, as the larger range of correlation lengths can be analyzed.

The curvatures of the trends in Figure 5.11 are related to the shape of the autocorrelation function of the electron density in the graphite. The relation between the mean visibility and the real-space autocorrelation function is represented in Eq. 5.16. The scattering function $G(\xi)$ is represented by the decrease in the visibility of the mask pattern and can be defined as

$$\frac{V_{\xi}}{V_0} = \exp\left[-\Sigma(1 - G(\xi))\right], \tag{5.37}$$

where $G(\xi)$ is the real-space autocorrelation function for the dense random media (Eq. 5.20).

As have been demonstrated in Section 5.3.1, the structure of graphite can be described as an ihnomogeneous random media with fractal-like distribution of scattering structures. The real-space autocorrelation function of such media can be well approximated by Eq. 5.20. Using the analytical expression of the real-space autocorrelation function and the relation in Eq. 5.37, we can perform the fit with the fitting function

$$-\ln\left(\frac{V_{\xi}}{V_0}\right) = \Sigma\left[1 - \frac{2}{\Gamma(H+1/2)}\left(\frac{\xi}{2a}\right)^{H+1/2} K_{H+1/2}\left(\frac{\xi}{a}\right)\right]. \tag{5.38}$$

Three characteristic parameters can be derived from this fit: macroscopic scattering cross-section Σ, characteristic size parameter a and the Hurst exponent H. Note that the value of a is not the average scatterer [96], which can be found using the values of a and H according to Eq. 5.22.

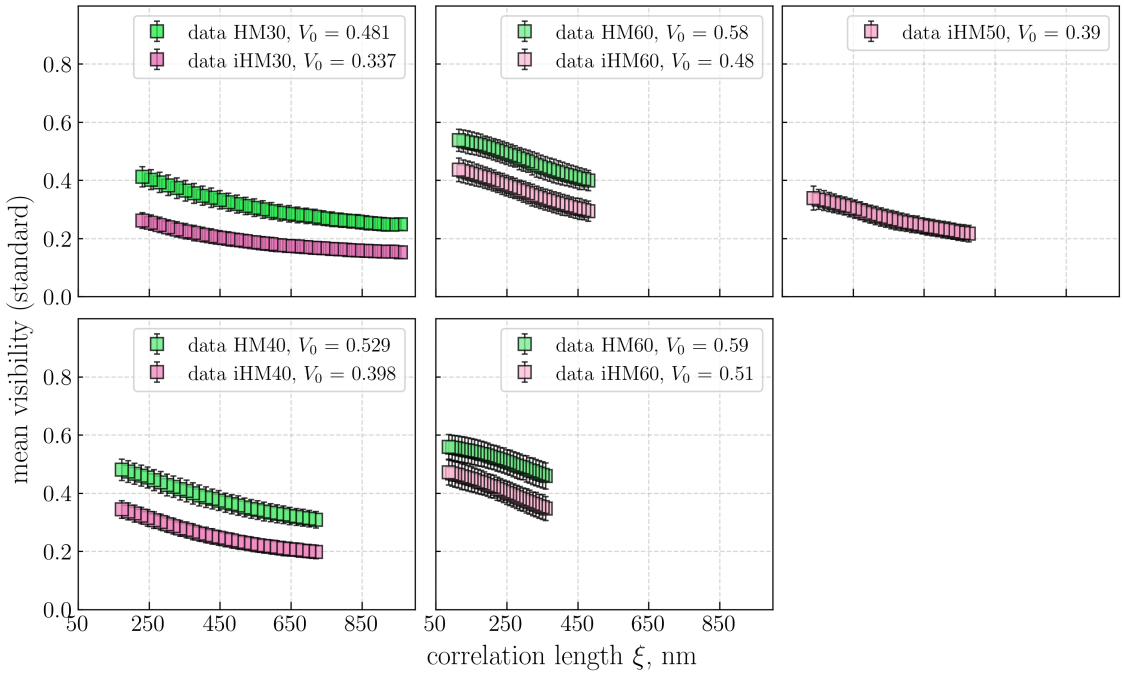

Figure 5.11: Mean visibilities calculated using Eq. 5.25 for Hartmann masks (HM and iHM) with periods 30 μm (HM30, iHM30), 40 μm (HM40, iHM40), 50 μm (iHM50), 60 μm (HM60, iHM60), 80 μm (HM80, iHM80).

Assuming the predominantly spherical shape of the graphite pores we can calculate the macroscopic scattering cross-section as

$$\Sigma = \frac{3\pi^2}{\lambda^2} d \left|\Delta\chi\right|^2 \phi_p \phi_s t \tag{5.39}$$

where λ is the wavelength, $|\Delta\chi|$ is the difference in complex refractive index between graphite and air, d is the average pore size, ϕ_s is a relative fraction of solid media, ϕ_p is the pore relative fraction, and t is the sample thickness. If we know the object thickness and the material which constitutes it, we can find the relative pore fraction ϕ_p from the Eq. 5.39 by solving the quadratic equation:

$$\phi_p^2 - \phi_p + \frac{\Sigma\lambda^2}{3\pi^2 d \left|\Delta\chi\right|^2 t} = 0, \tag{5.40}$$

where $\phi_s = (1 - \phi_p)$. This quadratic equation has two solutions which are representing the pore volume fraction and the relative solid fraction. Alternatively, the formula in Eq. 5.39 can be incorporated in the fitting function (Eq. 5.38) directly with an additional condition $\phi_p = 1 - \phi_s$. Here, the macroscopic cross-section was obtained from the fit first to avoid introducing two more fitting parameters.

The error of the relative pore fraction can be calculated as

$$\Delta_{\phi_p} = \sqrt{\left(\frac{\partial\phi_p}{\partial\Sigma} \cdot \Delta_\Sigma\right)^2 + \left(\frac{\partial\phi}{\partial d} \cdot \Delta_d\right)^2}. \tag{5.41}$$

Thus, from fitting the values of mean visibility (Figure 5.11) using Eq. 5.38, we can obtain:

- macroscopic scattering cross-section Σ, from which the relative pore fraction ϕ_p (Eq. 5.40) can be calculated;

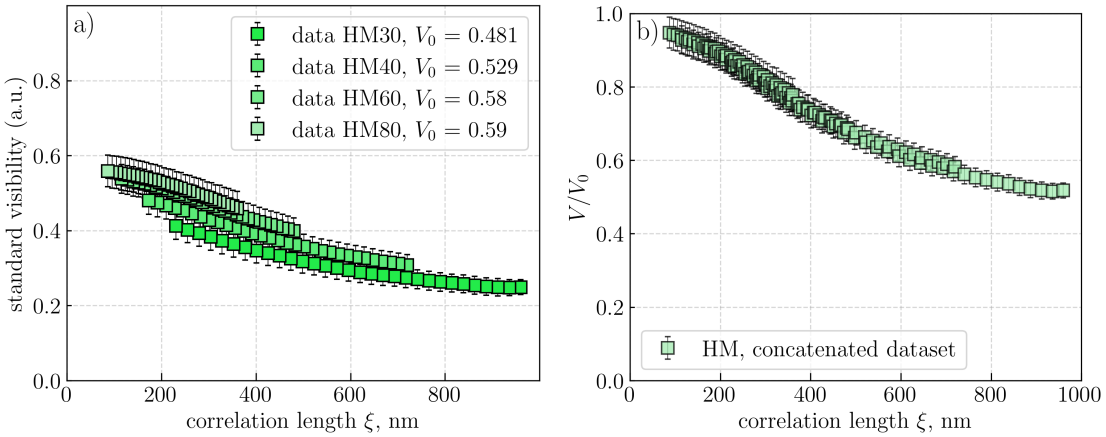

Figure 5.12: Visibility data for the Hartmann masks (HM30, HM40, HM60, HM80): a) the mean visibilities for each mask with the values of V_0 (Eq. 5.43); b) concatenated data set for all Hartmann masks.

- the value of Hurst exponent H, from which the fractal dimension (Eq. 5.21) can be estimated;
- average pore size d (Eq. 5.22).

However, to apply this fitting function we need to know the mean visibility V_0 at no scattering such that $\xi = 0$ (equivalent to the mean of the modulation function). In a typical imaging setting this would be the visibility of the reference image without the object. This visibility value V_0 is affected by a plethora of factors, including the detector PSF, source blurring and divergence, energy and intensity of the source, and mask quality. The latter includes the shape and the height of the absorbing structures, the absorbance and the homogeneity of the substrate, etc. The most practical way to estimate this value is from the experimental data.

As one can see in Figure 5.12a, the value of V_0 would the visibility at the intersection with the ordinate axis at $\xi = 0$. Following this logic, one can determine V_0 from fitting the set of mean visibility V_i for each mask acquired for ξ_i with $i = 1, 2, ..., 30$. The fitting function for the mean visibility values normalized by visibility at the smallest probed scattering length ξ_{min} for each mask is

$$\frac{V_i}{V_{\xi_{min}}} = \exp\left[\sigma t(G(\xi_i) - G(\xi_{min}))\right], \tag{5.42}$$

where $G(\xi)$ is the real-space autocorrelation function at the correlation length ξ (Eq. 5.20). The obtained fitting parameters were plugged into the following equation

$$V_0 = \frac{V_{\xi_i}}{\exp\left[\sigma t(G(\xi_i) - 1)\right]} \tag{5.43}$$

to obtain the mean visibility values at no scattering V_0 for each mask. Then the data set for each mask can be normalized by V_0 and concatenated together to obtain fine sampling of the real-space autocorrelation function over the range from 87 to 960 nm (Figure 5.12b).

The same procedure can be performed for the inverted Hartmann mask design (iHM) (Figure 5.13). The concatenated datasets in Figure 5.12b and Figure 5.13b can be used for fitting according to Eq. 5.38.

The fitting was performed using SciPy library available for Python. The errors for fitting parameters σt, a, H were determined from the generated covariance matrix. The average pore size and the relative pore volume fraction were calculated according to Eq. 5.22 and Eq. 5.40, and their errors according to Eq. 5.23

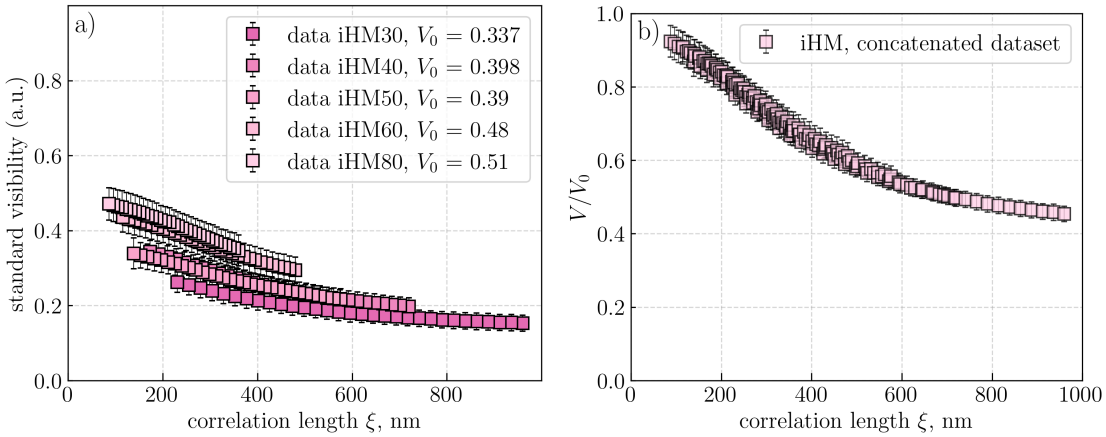

Figure 5.13: Visibility data for the inverted Hartmann masks (iHM30, iHM40, iHM50, iHM60, iHM80): a) the mean visibilities for each mask with the values of V_0 (Eq. 5.43); b) concatenated data set for all inverted Hartmann masks.

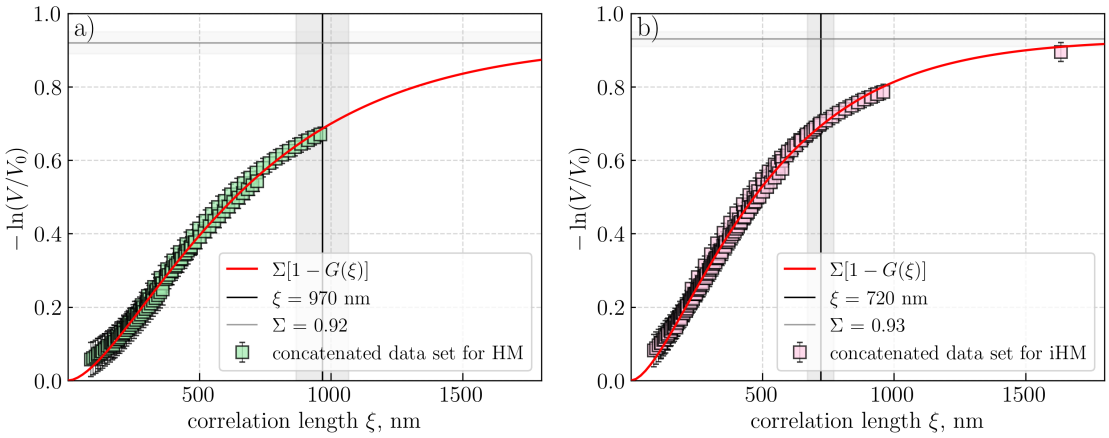

Figure 5.14: Values of the scattering intensity $-\ln(V/V_0)$ and the fitting function for a) the conventional Hartmann mask design (HM), b) the inverted Hartmann mask design (iHM).

and Eq.5.41, respectively. The fitted curves for the scattering intensity are shown in Figure 5.14. The values obtained from the fit are summarized in Table 5.2.

To check if the fit correctly predicts the value of scattering intensity at correlation lengths larger than 1 μm, we used the projection image for iHM-50 at the distance of 1120 mm from the detector, corresponding to the correlation length ξ = 1.6 μm. Note that the extra point acquired for the iHM-50 represents 1 % of the data, and its influence on the fitting function can be neglected. As one can see from Figure 5.14(b), the value of the extra data point is well predicted by the fitting function.

The final results of the fit and the calculated values of d and ϕ_p for HM and iHM are presented in Table 5.2 in the first two rows (under "Standard"). Both pore fraction and the average pore size values are in close agreement with the values reported for "angstrofine" grade graphite [111].

5.3.3.2 Interpretation and Discussion

Hartmann vs. inverted Hartmann design. One can see from Table 5.2, that the error in fit parameters a and H, which are used to calculate the average pore size d, for inverted Hartmann masks is noticeably lower than that for the conventional Hartmann masks. The error for average pore size Δd was calculated as

Table 5.2: Parameters derived from the visibility measurements. Macroscopic cross-section σt, characteristic parameter a and Hurst exponent H are determined from the fit of experimental data. Average pore size d and relative pore fraction ϕ_p were calculated using the values of a, H and σt. The reference data is taken from the specifications for graphite [109, 110, 111].

Mask type	σt	a (nm)	H	d(nm) (Eq. 5.22)	ϕ_p (Eq. 5.39)
Standard					
HM	0.92 ± 0.03	437 ± 32	0.58 ± 0.06	970 ± 100	22 ± 2 %
iHM	0.93 ± 0.02	326 ± 15	0.58 ± 0.05	730 ± 50	22 ± 1 %
Gauss					
HM	1.00 ± 0.03	360 ± 22	0.72 ± 0.06	930 ± 60	18 ± 1 %
iHM	1.28 ± 0.06	310 ± 50	0.67 ± 0.16	760 ± 115	35 ± 4 %
Reference	-	-	-	750 ± 100	$\geq$ 20 %

the error of indirect measurements using partial derivatives of Eq. 5.23 (Table 5.2). The higher Δd might be caused by the fact that the area of the inverted Hartmann mask covered with gold is 25 % of the total field of view of the sample; hence the scattering signal is formed from a larger object area compared to the conventional Hartmann mask. The total amount of scattering centers contributing to the signal is larger, making the obtained results more representative of the bulk structure. The advantage of having a higher signal-to-noise ratio when using the inverted Hartmann mask design for differential phase contrast imaging has been reported in the previous chapters [91].

Hurst exponent and fractal dimension of pore structure. An important parameter for porous material is its fractal dimension D_f, which indicates how the pores are structured under fractal theory approximation [107, 112]. The fractal dimension is defined by its Euclidean dimension D_E as well as the value of Hurst exponent. Another terminology also uses the "roughness" exponent value α, which is related to the Hurst exponent:

$$D_f = D_E + 1 - H = 1.5D_E + 1 - \alpha. \tag{5.44}$$

As follows from Eq. 5.21, for the Euclidean dimension $D_E = 2$

Knowing that the phase boundary parameter α can be determined as $\alpha = H + D_E/2$, we can define the Euclidean dimension of the pore structure in graphite by performing a simplified fit according to the Eq. 5.17 on the same dataset. The fitting result indicated $\alpha = 1.46 \pm 0.02$ for iHM and $\alpha = 1.52 \pm 0.03$ for HM. From this, we can estimate the Euclidean dimension of the scatterers to be $D_E = 2$. The fractal dimension then is $D = D_E + 1 - H \approx 2.48 \pm 0.06$, attributed to fractal structures like Apollonian sphere packing ($D = 2.4739465$ [113]).

Considering that the Hurst exponent $H = 0.5$ is characteristic for a perfectly random inhomogeneous solid, the obtained $H = 0.58$ suggests that the distributions of ihnomogeneities in graphite is predominantly random with a slight inclination to being persistent. The fractal dimension of $D = 2.48$ implies that the pore structure of graphite can be represented by the spheres of different size cotangent to each other [114].

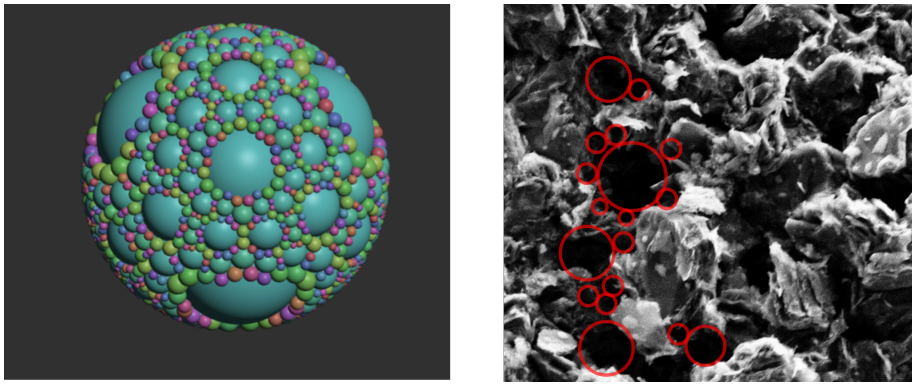

Figure 5.15: Illustration of the Apollonian sphere packing using the software ApolFrac (7 iterations) and how it can be interpreted for the graphite structure.

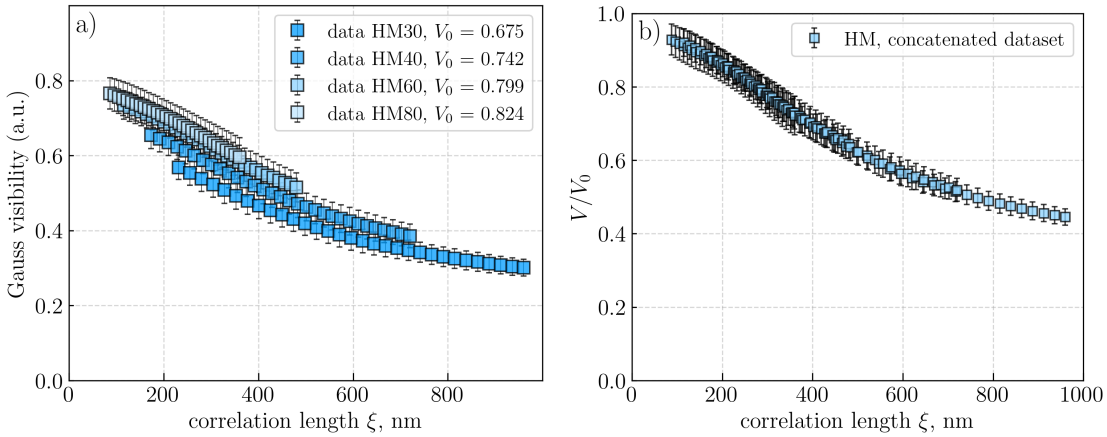

Figure 5.16: Visibility data for the Hartmann masks (HM30, HM40, HM60, HM80): a) the mean visibilities for each mask calculated from Gaussian fitting with the values of V_0 (Eq. 5.43); b) concatenated data set for all Hartmann masks.

5.3.4 Scattering intensity via multi-gaussian fitting

As have been mentioned in Section 5.2.2, analysis of the periodic pattern can be done via multi-gaussian fitting of the mask projection. This approach is intuitive and provides the direct measure of the increasing width of the individual beamlet.

The fitting of the projections obtained from the conventional and inverted Hartmann masks have been done with fitmultigaussian function [65] used in Shack-Hartman sensor wavefront reconstruction software [92].

5.3.4.1 Visibility via multigaussian fitting

The visibility value from individual beamlet fitting was obtained using Eq. 5.28; the results are shown in Figure 5.16 and Figure 5.17 for the conventional and inverted masks, respectively. The obtained data sets for mean visibility where treated in a similar manner, as reported in the previous subsection, and the resulting concatenated data sets were fitted using Eq. 5.38. The results of the fit are presented in Table 5.2 as well.

One can see, that the results obtained with multigaussan fitting are similar to the ones retrieved from fitting the curves obtained with standard visibility. The values of characteristic size parameter are similar, however, the values of Hurts exponent with Gauss visibility are noticeably higher. The resulting values of average pore size are close to the values obtained with standard visibility, and are in agreement with the specifications

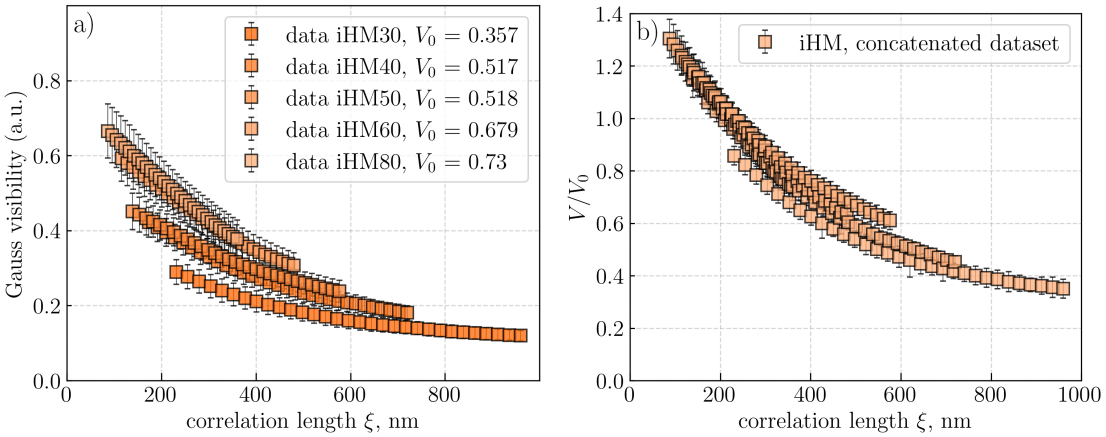

Figure 5.17: Visibility data for the inverted Hartmann masks (iHM30, iHM40, iHM50, iHM60, iHM80): a) the mean visibilities for each mask calculated from Gaussian fitting with the values of V_0 (Eq. 5.43); b) concatenated data set for all inverted Hartmann masks.

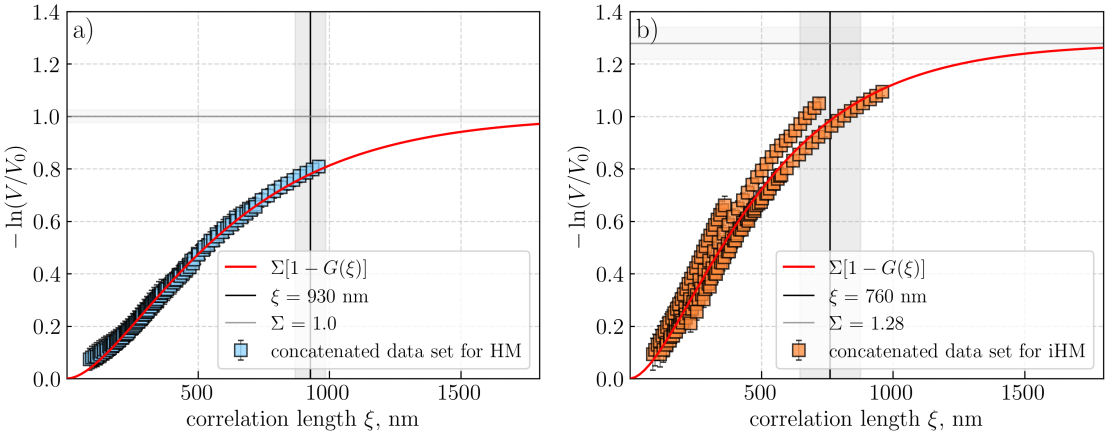

Figure 5.18: Values of the scattering intensity $-\ln(V/V_0)$ and the fitting function for Gaussian fitting: a) the conventional Hartmann mask design, b) the inverted Hartmann mask design.

from the graphite manufacturer. However, the estimated pore volume fraction for iHM and HM are quite different: it looks like for HM the relative pore volume fraction is too low, and for iHM too high. The change in visibility (the trend) measured by Gauss is similar, which makes it possible to retrieve the value of average pore size accurately; however, as the visibility values are shifted towards higher values, the value of macroscopic scattering cross-section is not accurately predicted by the fit.

It is important to note, that the visibility defined from multigaussian fitting coincides with the standard intensity visibility only for mask duty cycles up to 0.5. For higher duty cycles (larger relative beamlet widths), gaussian visibility provides inadequately high values, because the created intensity spot does not drop down to the background signal within the projected unit cell of the mask [65]. For all masks used in this experiment the duty cycle was 0.5 (0.25 relative beamlet width).

5.3.4.2 Directional scattering via Gaussian width

The visibility map analysis, while being easy and fast to implement, does not provide directional information about the scattering function [4, 12]. One of the advantages of using the Hartmann mask is that it offers periodic modulation in two directions, which enables separation of the horizontal and vertical components

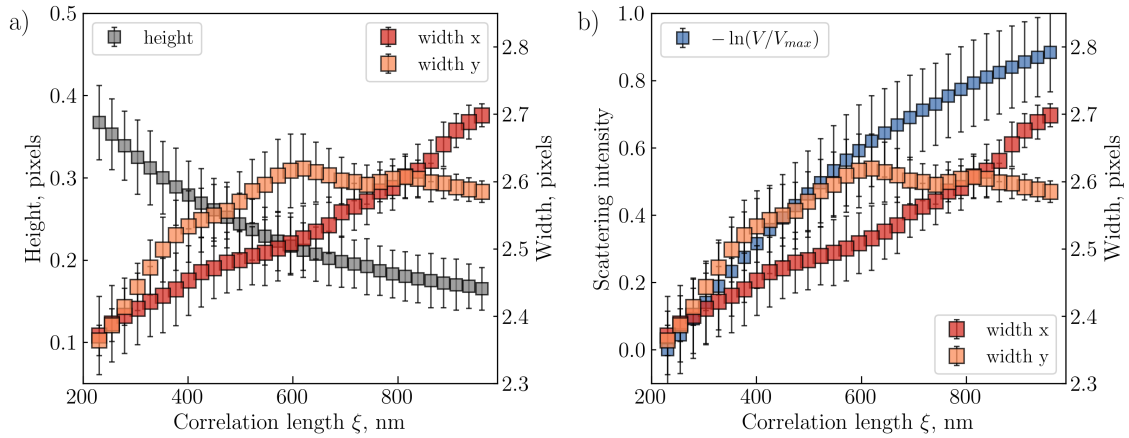

Figure 5.19: Data from multigaussian fitting for iHM30: a) the change in the average height and widths of the gaussians, b) the change in the scattering intensity calculated from the visibility decrease and the widths of the gaussians in two directions.

of the scattering signal. Such directional approach is possible to implement through multigaussian fitting or Fourier analysis.

Scattering of X-ray will dampens the projected pattern contrast: it will decrease the visibility but also results in the broadening of the beamlets. The diffuse scattering will "redistribute" the photons in a way, that the decrease in Gaussian height (visibility) should be proportional to the increase in its width. Fitting with 2D Gaussian distribution provides estimates of the width in two orthogonal directions, further denoted as width x and width y. In Gaussian fitting approach, the changes in the height of the individual Gaussians are interpreted as the changes in absorption. However, for strongly scattering objects with low absorption the decrease in the Gaussian height can be associated with the redistribution of intensity due to the scattering.

Figure 5.19a shows how the height and the width in two directions change for different correlation lengths: as the sample is moved further away from the detector (larger correlation length), the height of the beamlet decreases, while the width grows (redistribution of intensity). For the sample under study (500 µm graphite) the absorption is neglectable: graphite transmits more than 90 % of the incident radiation at 17 keV. In the setup the sample was moved along the beam axis but no change in absorption was supposed to be observed as the material thickness or composition was not changed. However for the multigaussian analysis a strong reduction in height is observed which would generally be interpreted as absorption (or transmission) signal. Thus, multigaussian fitting shows the cross-talk between the scattering and the transmission as well, especially pronounced for strongly scattering structure like graphite. Due to this cross-talk the changes in the width of the Gaussians can only be interpreted qualitatively: the width grows with the correlation length (Figure 5.19b), but the fluctuations cannot be reliably interpreted to estimate the anisotropy of the pore sizes in two directions.

5.3.5 Relative scattering intensity with Fourier analysis

Despite the cross-talk between the absorption and scattering due to the beam hardening, reported for highly absorbing structures and polychromatic radiation [17], Fourier analysis performs better for weakly absorbing scattering media such as graphite. In Figure 5.20 there is no spurious signal for absorption channel observed: it does not change with sample movement towards the detector. Only for the propagation distances above 1 m (Figure 5.20c), as was achieved for iHM50, there is a slight growth in absorption signal caused by the drastic increase in mask scattering. As was shown in Section 5.3.2, for such configuration ($P = 50\mu m$, $L = 1.12m$) the influence of beam divergence starts to be more pronounced.

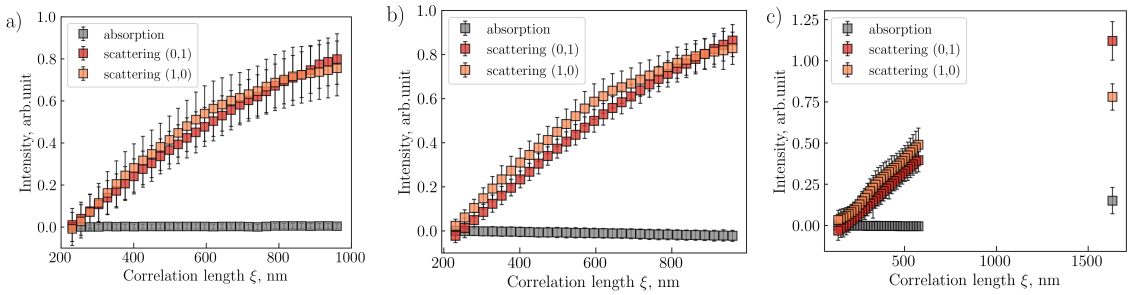

Figure 5.20: Fourier analysis results. Absorption and scattering in two orthogonal directions depending for probed scattering length: a) for iHM30, b) for HM30, c) for iHM50.

For scattering channels there is a strong signal grows when the scattering length approaches the average pore size, as have been observed for the analysis of visibility reduction. The same dependencies have been observed for all masks. This indicates that this approach can be used for the analysis of pore size anisotropy in graphite.

The spatial frequency spectrum of the Hartmann mask projection contains a strong primary peak around zero spatial frequency and a number of the sharp peaks (harmonics with orders $m, n = [0, 1, 2, ...]$) separated by the $N \cdot 2\pi/P$ distance, where P is the period of the mask and $N = \sqrt{m^2 + n^2}$. In such a setting, S_{01} and S_{10} are attributed to the first-order Fourier amplitudes in the horizontal and vertical directions, respectively, S_{02} and S_{20} are the second-order harmonics, etc. The "mixed" harmonics $S_{11}, S_{22}, ...$, are located on a diagonal from the (0,0) harmonic and contain the information about scattering in both directions. Note that the scattering length to which the harmonic is sensitive is assumed to scale with the harmonic order as $\xi = N \cdot \lambda L/P$.

Since no scattering-free reference image was obtained in the measurements (the mask was manufactured directly on the graphite), only the change in scattering intensity relative to the signal at the smallest correlation length can be retrieved.

5.3.5.1 First order spatial harmonic analysis

The first order analysis includes scattering intensity from harmonics (0,1), (1,0) and (1,1). In Figure 5.21 one can see the mean scattering intensity for these harmonics. Note that the scattering intensity $S_{(1,1)}$ will be sensitive to a larger correlation length range according to $\xi = \sqrt{2} \cdot \lambda L/P$. The continous line in Figure 5.21 indicates the theoretical function $(1 - G(\xi))$ with $G(\xi)$ from Eq. 5.20 with parameters a and H from the fitting of the visibility measurements (Table 5.2, standard) for the conventional and inverted Hartmann masks.

Since S_{01} and S_{10} are defined for each effective pixel of the imaging system, we obtained the scattering distribution maps in two dimensions for each correlation length ξ. Examples of such maps for correlation lengths ξ = 153 nm and ξ = 1634 nm are shown in Figure 5.22. One can see the directional distribution of scatterers in horizontal (green) and vertical (red) directions through the non-even distribution of red and green in the pseudo color images. The mean values of S_{01} and S_{10} for different correlation lengths represented by the data points show that the scattering is mostly isotropic for pores smaller than 580 nm. As the length scale increases up to 1600 nm, the horizontal scattering starts to dominate.

For the data in Figure 5.22 we applied the simplified fit according to Eq. 5.17 with $1 < \alpha < 2$. We determined the characteristic pore size in horizontal and vertical directions to be $d_{hor} = 890 \pm 60$ nm and $d_{vert} = 580 \pm 20$ nm, and the average of the two being 735 nm, which is in agreement with the average

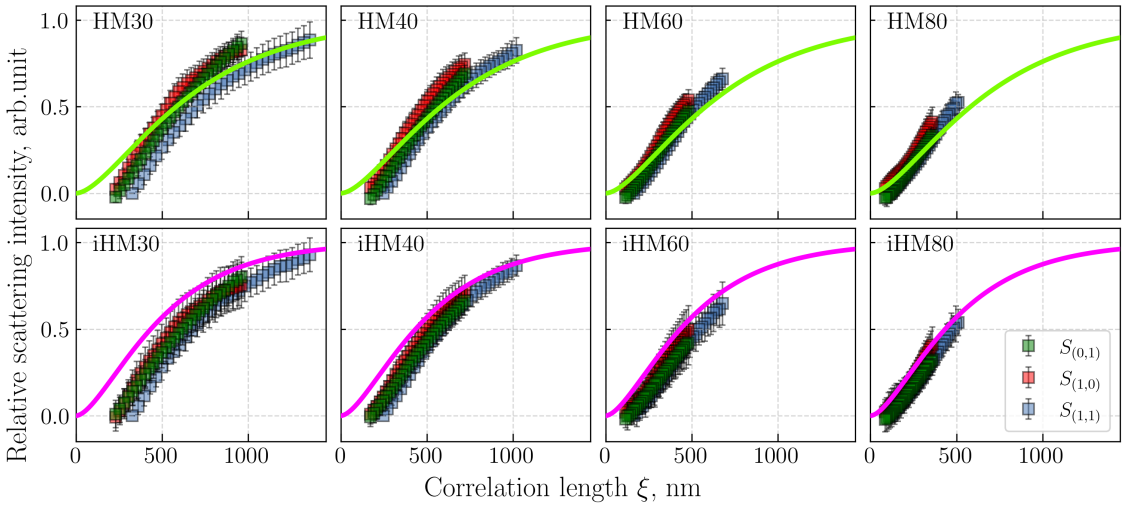

Figure 5.21: First order harmonic analysis: scattering intensity from harmonics (0,1) (green), (1,0) (red) and (1,1) (blue). The line is the $(1 - G(\xi)$ function with $G(\xi)$ from Eq. 5.20 and parameters a and H from Table 5.2 for standard visibility analysis. The top row shows the data for the conventional Hartmann masks and the lower row for the inverted Hartmann mask.

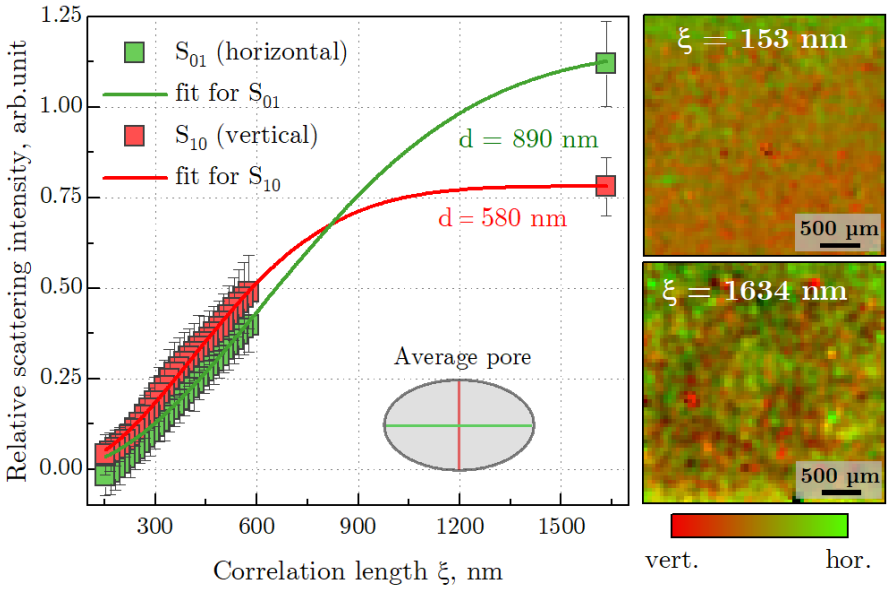

Figure 5.22: Directional analysis of scattering contrast represented by an overlay of the Fourier amplitudes S_{01} in horizontal (green) and S_{10} in vertical direction (red). The two-dimensional scattering intensity distribution maps for correlation lengths ξ = 153 nm and ξ = 1634 nm are shown on the right as pseudo color images. The inset in the graph shows the shape of an average pore.

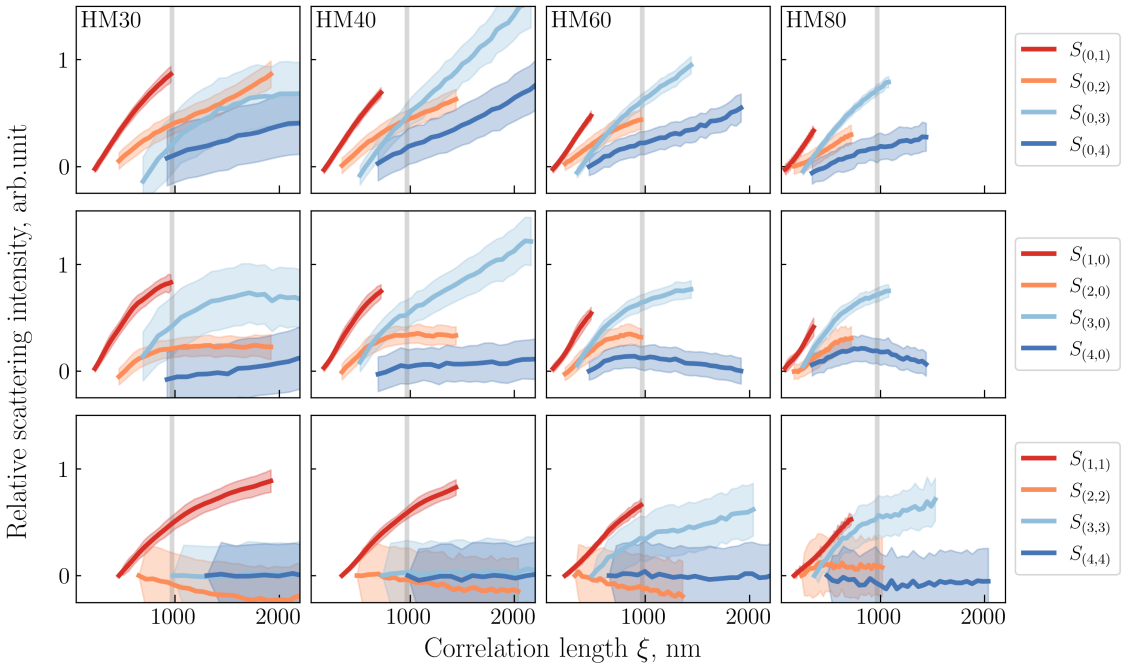

Figure 5.23: Changes in scattering intensity obtained from the first, second, third and fourth order harmonics in spatial Fourier spectrum for Hartmann masks: scattering in horizontal direction ($S_{(0,1)}$, $S_{(0,2)}$, $S_{(0,3)}$, $S_{(0,4)}$), in vertical direction ($S_{(1,0)}$, $S_{(2,0)}$, $S_{(3,0)}$, $S_{(4,0)}$), scattering in diagonal direction (($S_{(1,1)}$, $S_{(2,2)}$, $S_{(3,3)}$, $S_{(4,4)}$)). The gray vertical line indicates the value of 750 nm.

pore size obtained by the visibility map analysis. The average pore size in the horizontal direction is larger than in the vertical, indicating the elliptical shape of the characteristic pores (Figure 5.22). Note that relative scattering signal measurements cannot correctly predict the pore fraction and Hurst exponent.

5.3.5.2 On applicability of higher order spatial harmonics

Another advantage of Fourier analysis method is that it gives access to higher order harmonics which can be sensitive to larger scatterers [94]. The simulations of scattering intensity have shown [65] that the correlation length for higher orders shifts linearly with the distance to the central point in Fourier space (zeroth order harmonic). Figure 5.24 shows the changes in scattering intensity calculated for harmonics up to the fourth order for the inverted Hartmann mask. As the signal intensity is decreasing with the harmonic's order due to the limited photon statistics, and the error increases. One can clearly see this in Figure 5.25: already for $n = 2$ the standard deviation of the scattering intensity in the image is increasing, while the signal decreases down to 0 for $n = 4$.

In Figure 5.24 a and b we can see that the first and second order harmonics signal tends to reach a saturation value around 750 nm (gray line), which is in agreement with the results obtained in Section 5.3.3.1 of Chapter 5. As it was mentioned in Section 5.2.3, the number of spatial harmonics in Fourier space will depend on the sampling of the mask: how many pixels there are per mask period. If the mask is sufficiently sampled and the image quality is high, it is possible to retrieve scattering intensity at several correlation lengths in from a single frame. Such approach has been implemented with Fresnel zone plates array [101], but can also be used with Hartmann masks given high beam intensity and larger mask period or smaller pixel size. For the measurements of graphite scattering with Hartmann masks with period up to 80 µm the scattering intensity obtained from the fourth harmonic was already not distinguishable from noise (standard deviation of the signal within the image) for all measurements. The second and the third order harmonics have

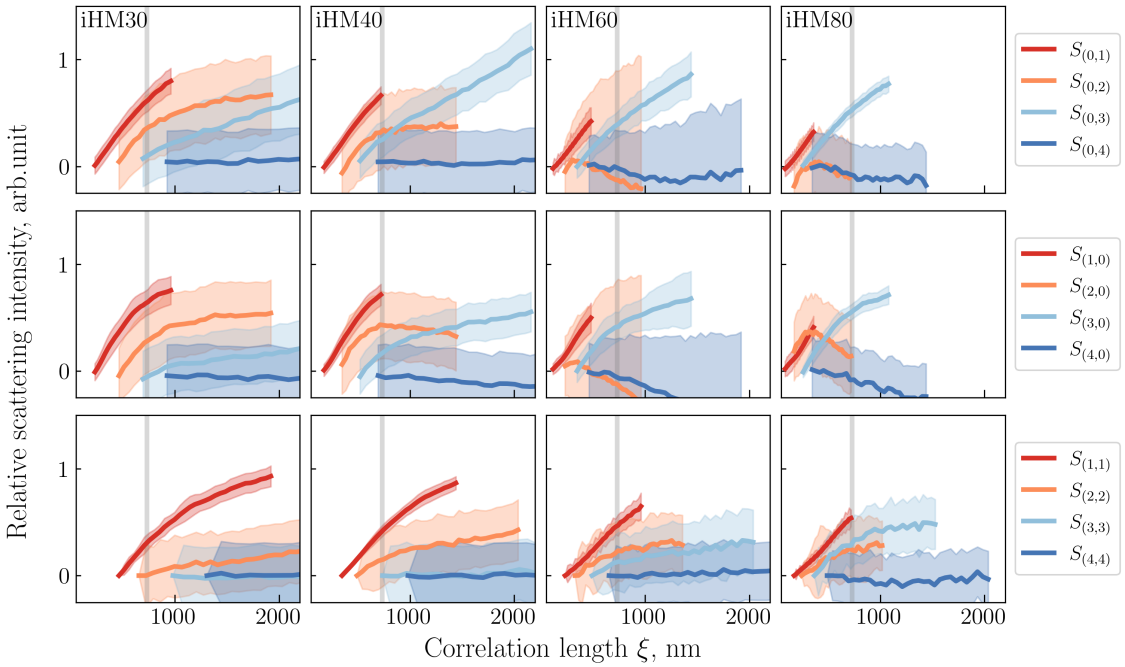

Figure 5.24: Changes in scattering intensity obtained from the first, second, third and fourth order harmonics in spatial Fourier spectrum for the inverted Hartmann masks: scattering in horizontal direction ($S_{(0,1)}$, $S_{(0,2)}$, $S_{(0,3)}$, $S_{(0,4)}$), in vertical direction ($S_{(1,0)}$, $S_{(2,0)}$, $S_{(3,0)}$, $S_{(4,0)}$), scattering in diagonal direction (($S_{(1,1)}$, $S_{(2,2)}$, $S_{(3,3)}$, $S_{(4,4)}$)). The gray vertical line indicates the value of 750 nm.

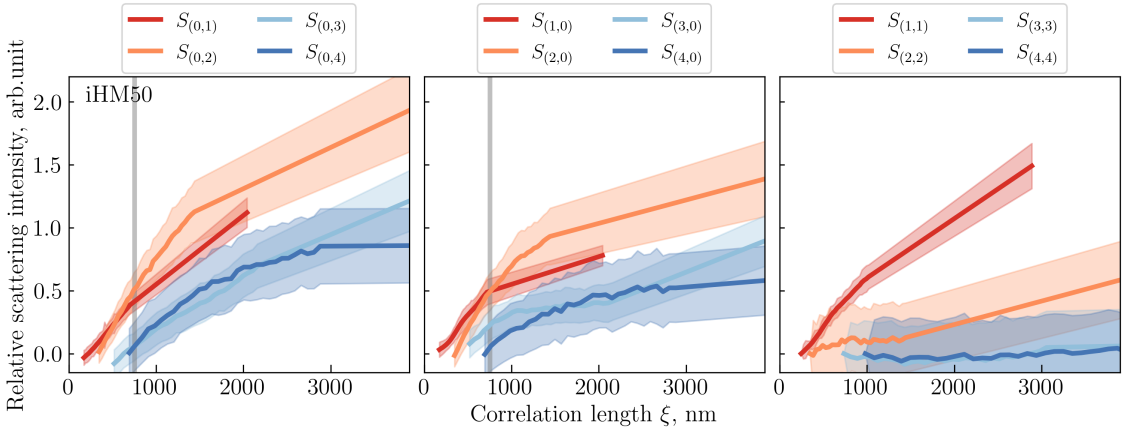

Figure 5.25: Changes in scattering intensity obtained from the first, second, third and fourth order harmonics in spatial Fourier spectrum for the inverted Hartmann mask with period 50 µm: scattering in horizontal direction ($S_{(0,1)}$, $S_{(0,2)}$, $S_{(0,3)}$, $S_{(0,4)}$), in vertical direction ($S_{(1,0)}$, $S_{(2,0)}$, $S_{(3,0)}$, $S_{(4,0)}$), scattering in diagonal direction (($S_{(1,1)}$, $S_{(2,2)}$, $S_{(3,3)}$, $S_{(4,4)}$)).

exhibited the expected behaviour and could be associated with sensitivity to larger pores and agglomerates with sizes about 1.5-2 µm.

5.3.6 Pore size distribution

The obtained values of average pore size and Hurst exponent can help to predict the pore size distribution. Practically important information about the pore size distribution is the peak (mode) of the distribution that indicates the most represented pore size, average (mean) pore size, and the width of the distribution - the range which contains most of the pores.

If we assume that pore sizes X are following a log-normal distribution, the expected value of the $ln(X)$ will be $\mu = ln(d)$, with d being the median of the pore size distribution. This value we obtain as characteristic pore size d. In case of log-normal distribution, the median equals a multiplicative mean, which is in agreement with the typical pore structuring: smaller pores cluster and form larger pores, such that the cluster size grows proportionally to the size of the individual pore.

The Hurst exponent characterizes the deviation of the electron density distribution from the mean value (or "roughness of the distribution") [96]. If we assume it to serve as an estimate of the standard deviation of the random variable $ln(X)$, the geometric standard deviation factor will be e^H. Using the values of average pore size d and Hurst exponent H, we can evaluate the pore size range containing 2/3 of all pores as the scatter intervals of the distribution from $d/e^H = 400$ nm to $d \cdot e^H = 1340$ nm. We can simulate the log-normal distribution of a random variable X based on the data obtained by the scattering contrast (Figure 5.26a). Therefore, the distribution of pore sizes X can be characterized by the following values:

$$Mode\,|X| = \exp\left[\ln(d) - H^2\right] = d \cdot e^{-H^2} \approx 520\ nm, \tag{5.45}$$

$$Median\,|X| = \exp\left[\ln(d)\right] = d \approx 730\ nm, \tag{5.46}$$

$$Mean\,|X| = \exp\left[\ln(d) + H^2/2\right] = d \cdot e^{H^2/2} \approx 860\ nm. \tag{5.47}$$

In Figure 5.26, we compare the simulated bulk pore size distribution to the surface pore size distribution obtained from the set of SEM images. Note that the distribution obtained from SEM images is not comprehensive and is only valid for a restricted field of view (hence with limited pore size statistics) on the surface of graphite. Nevertheless, it is a valuable benchmark to see if the simulated distribution is realistic. Figure 5.26 shows that, although the distributions differ in shape, the mode of the simulated distribution (dashed line at 519 nm in Figure 5.26(b)) is close to the mode of the surface pore size distribution (shown as the dashed line at 585 nm in Figure 5.26(a)). The median of the simulated distribution (730 nm) is very close to the median of the measured one (717 nm), however, the means differ noticeably. However, we can see that the fit for the measured SEM distribution does not closely approximate the larger pores in the range from 900 nm to 1500 nm. This might be due to the small field of view which limits the statistics obtained from

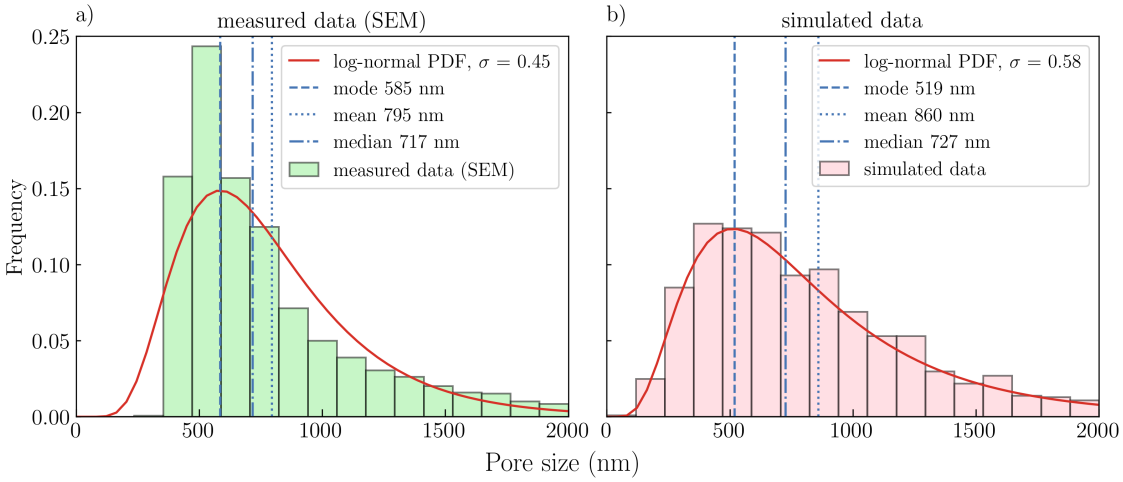

Figure 5.26: Comparison of the pore size distributions: a) simulated bulk pore size distribution based on the scattering data, b) surface pore size distribution obtained from a set of SEM images. Modes of the distributions are indicated by the dashed lines and the medians by the solid lines.

the SEM images. The two distributions are very similar in shape, which implies that the data obtained with the scattering contrast in multimodal X-ray imaging can be used derive information about size distribution of dense media with random feature sizes.

6 Summary and Outlook

Fabrication of conventional and inverted Hartmann masks for X-ray imaging

UV lithography in combination with gold electroplating enabled a robust and available fabrication of high-quality conventional and inverted Hartmann masks. The manufacturing approach allows for customization of masks to the final application in terms of the required period (from 10 to 100 µm, depending on required thickness), area (at least up to 5 x 5 cm), thickness (gold height at least up to 30 µm are accessible), and substrate carrier. Using polyimide with conductive coatings to fabricate inverted Hartmann masks is possible when minimization of absorption in the optical component is required. As a possible way to create a substrate-less conventional Hartmann mask, the conductive carbon coating can be stripped away, and the mask can be detached from the substrate carrier.

Shorter wavelengths for lithography can also be applied, as offered by deep X-ray lithography. It would potentially limit the accessibility and robustness of the manufacturing procedure and might not be necessary for most applications due to the limited pixel size available. However, if periods below 10 µm or absorber heights above 50 µm are required, deep X-ray lithography can be a viable option to create Hartmann masks.

Characterization of Hartmann masks

Characterization of Hartmann masks guides and consults the fabrication procedure. The relative absorption histogram approach helps to evaluate the gold absorber height homogeneity across the mask area and predict mask performance in the imaging setup. Further development of this method can include pattern recognition algorithms evaluating the impact of local defects on the projection histogram. As a potential development direction, neural networks can enhance and accelerate the evaluation of mask quality from its projection and facilitate the classification of typical defects.

Conventional and inverted Hartmann masks performance

The inverted Hartmann masks achieve images with higher SNR and are less prone to the cross-correlation of absorption and scattering contrast modalities for setups susceptible to beam hardening (e.g., with poly-chromatic sources). However, the conventional design is more mechanically stable and can be manufactured without the substrate carrier, which can be an essential advantage for imaging at lower X-ray energies. Both mask designs enable multimodal X-ray imaging with the same spatial and angular resolution; thus, the choice of the mask can be motivated by the final application.

Time-resolved imaging with inverted Hartmann masks

The inverted Hartmann masks with higher flux efficiency compared to conventional design can be applied for time-resolved imaging. Multimodal X-ray imaging with Hartmann masks is a truly single-shot method and requires no mask or sample movement. Dynamic processes at different time scales can be visualized with three contrast modalities. The time resolution is primarily restricted by the mask but depends on the brilliance of the available X-ray source and the frame acquisition rate of the detector. Time-resolved multimodal X-ray imaging with Hartmann masks can be performed for various applications in science and industry. Amongst possible examples are visualizations of chemical reactions, laser ablation, additive manufacturing.

Quantitative sub-µm characterization of complex structures using the scattering contrast modality

With Hartman masks, fine sampling of the real-space autocorrelation function can be achieved using a simple radiographic X-ray imaging setup with relaxed beam coherence and optical element requirements. In addition to the macroscopic imaging of the object, it offers a possibility to scan the real-space autocorrelation function of the electron density.

Various structural parameters can be obtained, such as average pore size in two orthogonal directions, relative pore fraction, fractal dimension, and the value of the Hurst exponent related to the space-filling capacity of the structure. The autocorrelation functions defined for spin-echo small-angle neutron scattering combined with fine scanning of correlation length show promise for studying complex features. For example, hollow microspheres or cohesive powders typically used as catalytic materials can be studied, as well as fibers (infinite cylinder structures) used for woven hierarchical polymer composites.

Such a versatile and straightforward technique can impact research devoted to studying complex structures like porous materials, colloids, or powders. Apart from the immediate profit for the development and characterization of porous catalytic materials, numerous medical applications related to early-stage cancer diagnostics and lung diseases can profit from knowing the morphology and fractal dimensions of complex interconnected structures.

Another possible direction of study can be associated with the higher-order spatial harmonics obtained using Hartmann masks. Combining high-brilliance source and Hartmann masks with efficient wavefront modulation can increase signal-to-noise ratio for higher-order harmonics and determine the autocorrelation function from a single projection, albeit with a lower sampling rate. Such an approach can be beneficial for incorporating autocorrelation function sampling for dynamic processes.

A Mask projection simulation

```
def create_HM_proj(det_area, pix_size, period, flux):
    """
    simulates the ideal projecion of the conventional
    Hartmann mask with duty cycle of 0.5.

    Parameters
    ----------
    det_area : tuple
        Area of the detector in pixels
    pix_size : int, float
        Detector pixel size (effective)
    period : int
        period of the mask.
    flux : int, float
        maximum flux/photon count.

    Returns
    -------
    grid : the simulated ideal projection.

    """

    import math
    import numpy as np
    half_pitch = math.ceil(period/(2*pix_size)) # DC 0.5
    fourth_pitch = math.ceil(period/(4*pix_size)) # DC 0.5
    pitch = math.ceil(period/pix_size) # period in pixels
    (pix_hor, pix_vert) = det_area # image size
    rep_x = math.ceil(pix_hor/pitch)
    rep_y = math.ceil(pix_vert/pitch)

    matrix = np.concatenate((
                    np.zeros((half_pitch,fourth_pitch)),
                    np.ones((half_pitch,half_pitch)),
                    np.zeros((half_pitch,fourth_pitch)
                    )), axis=1)

    unit_cell = np.concatenate((
                    np.zeros((math.ceil(matrix.shape[0]/2),
                    matrix.shape[1])),matrix,
```

```
                    np.zeros((math.ceil(matrix.shape[0]/2),
                    matrix.shape[1]))),axis=0)

    grid_temp = flux*np.tile(unit_cell,(rep_x,rep_y))
    grid = grid_temp[np.arange(pix_hor)[:,None],
                    np.arange(pix_vert)[None,:]]

    return grid

def create_iHM_proj(det_area, pix_size, period, flux):
    """
    simulates the ideal projecion of the inverted
    Hartmann mask with duty cycle of 0.5.

    Parameters
    ----------
    det_area : tuple
        Area of the detector in pixels
    pix_size : int, float
        Detector pixel size (effective)
    period : int
        period of the mask.
    flux : int, float
        maximum flux/photon count.

    Returns
    -------
    grid : the simulated ideal projection.

    """
    import math
    import numpy as np
    half_pitch = math.ceil(period/(2*pix_size)) # DC 0.5
    fourth_pitch = math.ceil(period/(4*pix_size)) # DC 0.5
    pitch = math.ceil(period/pix_size) # period in pixels
    (pix_hor, pix_vert) = det_area # image size
    rep_x = math.ceil(pix_hor/pitch)
    rep_y = math.ceil(pix_vert/pitch)

    matrix = np.concatenate((
                    np.ones((half_pitch,fourth_pitch)),
                    np.zeros((half_pitch, half_pitch)),
                    np.ones((half_pitch,fourth_pitch))),
                    axis=1)

    unit_cell = np.concatenate((
                    np.ones((math.ceil(matrix.shape[0]/2),
                    matrix.shape[1])),matrix,
```

```
                np.ones((math.ceil(matrix.shape[0]/2),
                matrix.shape[1]))),axis=0)

grid_temp = flux*np.tile(unit_cell,(rep_x,rep_y))
grid = grid_temp[np.arange(pix_hor)[:,None],
                np.arange(pix_vert)[None,:]]

return grid
```

List of Figures

List of Tables

List of Publications

As a first author

[1] Andrey Mikhaylov, Margarita Zakharova, Vitor Vlnieska, Ankita Khanda, Sabine Bremer, Marcus Zuber, Sergio Henrique Pezzin, and Danays Kunka. Inverted hartmann mask made by deep x-ray lithography for single-shot multi-contrast x-ray imaging with laboratory setup. *Opt. Express*, 30(6):8494–8509, Mar 2022.

[2] Margarita Zakharova, Andrey Mikhaylov, Stefan Reich, Anton Plech, and Danays Kunka. Bulk morphology of porous materials at sub-micrometer scale studied by dark-field x-ray imaging with hartmann mask. *preprint at arXiv*, 2021.

[3] Margarita Zakharova, Andrey Mikhaylov, Vitor Vlnieska, and Danays Kunka. Single-shot multicontrast x-ray imaging for in situ visualization of chemical reaction products. *Journal of Imaging*, 7(11):221, 2021.

[4] Margarita Zakharova, Stefan Reich, Andrey Mikhaylov, Vitor Vlnieska, Tomy dos Santos Rolo, Anton Plech, and Danays Kunka. Inverted hartmann mask for single-shot phase-contrast x-ray imaging of dynamic processes. *Optics letters*, 44(9):2306–2309, 2019.

[5] Margarita Zakharova, Vitor Vlnieska, Heike Fornasier, Martin Börner, Tomy dos Santos Rolo, Jürgen Mohr, and Danays Kunka. Development and characterization of two-dimensional gratings for single-shot x-ray phase-contrast imaging. *Applied Sciences*, 8(3):468, 2018.

In collaboration

[1] Sara Ferreira Da Costa, Marcus Zuber, Margarita Zakharova, Andrey Mikhaylov, Tilo Baumbach, Danays Kunka, and Sergio Henrique Pezzin. Self-healing triggering mechanism in epoxy-based material containing microencapsulated amino-polysiloxane. *Nano Select*, 2021.

[2] Andrey Mikhaylov, Stefan Reich, Margarita Zakharova, Vitor Vlnieska, Roman Laptev, Anton Plech, and Danays Kunka. Shack–hartmann wavefront sensors based on 2d refractive lens arrays and super-resolution multi-contrast x-ray imaging. *Journal of synchrotron radiation*, 27(3):788–795, 2020.

[3] Anton Plech, Bärbel Krause, Tilo Baumbach, Margarita Zakharova, Soizic Eon, Caroline Girmen, Gernot Buth, and Hartmut Bracht. Structural and thermal characterisation of nanofilms by time-resolved x-ray scattering. *Nanomaterials*, 9(4):501, 2019.

[4] Vitor Vlnieska, Andrey Mikhaylov, Margarita Zakharova, Eva Blasco, and Danays Kunka. Epoxy resins for negative tone photoresists. *Polymers*, 11(9):1457, 2019.

[5] Vitor Vlnieska, Margarita Zakharova, Martin Börner, Klaus Bade, Jürgen Mohr, and Danays Kunka. Chemical and molecular variations in commercial epoxide photoresists for x-ray lithography. *Applied Sciences*, 8(4):528, 2018.

[6] Vitor Vlnieska, Margarita Zakharova, Andrey Mikhaylov, and Danays Kunka. Lithographic performance of aryl epoxy thermoset resins as negative tone photoresist for microlithography. *Polymers*, 12(10):2359, 2020.

Conference contributions

[1] Andrey A Mikhaylov, Stefan Reich, Anton Plech, Margarita Zakharova, Vitor Vlnieska, and Danays Kunka. 2d lens array for multi-contrast x-ray imaging. In *EUV and X-ray Optics: Synergy between Laboratory and Space VI*, page 1103208, April 2019.

[2] Margarita Zakharova, Stefan Reich, Andrey Mikhaylov, Vitor Vlnieska, Marcus Zuber, Sabine Engelhardt, Tilo Baumbach, and Danays Kunka. A comparison of customized hartmann and newly introduced inverted hartmann masks for single-shot phase-contrast x-ray imaging. In *EUV and X-ray Optics: Synergy between Laboratory and Space VI*, page 110320U, April 2019.

Bibliography

[1] SW Wilkins, Ya I Nesterets, TE Gureyev, SC Mayo, A Pogany, and AW Stevenson. On the evolution and relative merits of hard x-ray phase-contrast imaging methods. *Philosophical Transactions of the Royal Society A: Mathematical, Physical and Engineering Sciences*, 372(2010):20130021, 2014.

[2] Franz Pfeiffer, Martin Bech, Oliver Bunk, Philipp Kraft, Eric F Eikenberry, Ch Brönnimann, Christian Grünzweig, and Christian David. Hard-x-ray dark-field imaging using a grating interferometer. *Nature materials*, 7(2):134–137, 2008.

[3] UetMHART Bonse and M Hart. An x-ray interferometer. *Applied Physics Letters*, 6(8):155–156, 1965.

[4] Franz Pfeiffer, Timm Weitkamp, Oliver Bunk, and Christian David. Phase retrieval and differential phase-contrast imaging with low-brilliance x-ray sources. *Nature physics*, 2(4):258–261, 2006.

[5] Atsushi Momose. Phase-sensitive imaging and phase tomography using x-ray interferometers. *Optics express*, 11(19):2303–2314, 2003.

[6] Adrian Sarapata, Maite Ruiz-Yaniz, Irene Zanette, Alexander Rack, Franz Pfeiffer, and Julia Herzen. Multi-contrast 3d x-ray imaging of porous and composite materials. *Applied Physics Letters*, 106(15): 154102, 2015.

[7] Lorenzo Massimi, Samuel J Clark, Sebastian Marussi, Adam Doherty, Joachim Schulz, Shashidhara Marathe, Christoph Rau, Marco Endrizzi, Peter D Lee, and Alessandro Olivo. Dynamic multicontrast x-ray imaging method applied to additive manufacturing. *Physical Review Letters*, 127(21):215503, 2021.

[8] A Olivo, D Chana, and R Speller. A preliminary investigation of the potential of phase contrast x-ray imaging in the field of homeland security. *Journal of Physics D: Applied Physics*, 41(22):225503, 2008.

[9] Erin A Miller, Timothy A White, Benjamin S McDonald, and Allen Seifert. Phase contrast x-ray imaging signatures for security applications. *IEEE Transactions on Nuclear Science*, 60(1):416–422, 2013.

[10] Ashley F Stein, Jan Ilavsky, Rael Kopace, Eric E Bennett, and Han Wen. Selective imaging of nanoparticle contrast agents by a single-shot x-ray diffraction technique. *Optics express*, 18(12):13271–13278, 2010.

[11] Markus Strobl. General solution for quantitative dark-field contrast imaging with grating interferometers. *Scientific reports*, 4(1):1–6, 2014.

[12] Wataru Yashiro, Y Terui, K Kawabata, and A Momose. On the origin of visibility contrast in x-ray talbot interferometry. *Optics express*, 18(16):16890–16901, 2010.

[13] Christian David, B Nöhammer, H_H Solak, and E Ziegler. Differential x-ray phase contrast imaging using a shearing interferometer. *Applied physics letters*, 81(17):3287–3289, 2002.

[14] Shivaji Bachche, Masahiro Nonoguchi, Koichi Kato, Masashi Kageyama, Takafumi Koike, Masaru Kuribayashi, and Atsushi Momose. Laboratory-based x-ray phase-imaging scanner using talbot-lau interferometer for non-destructive testing. *Scientific reports*, 7(1):1–7, 2017.

[15] A Olivo, Fulvia Arfelli, Giovanni Cantatore, Renata Longo, RH Menk, S Pani, M Prest, P Poropat, Luigi Rigon, G Tromba, et al. An innovative digital imaging set-up allowing a low-dose approach to phase contrast applications in the medical field. *Medical physics*, 28(8):1610–1619, 2001.

[16] Alessandro Olivo, Konstantin Ignatyev, Peter RT Munro, and Robert D Speller. Noninterferometric phase-contrast images obtained with incoherent x-ray sources. *Applied Optics*, 50(12):1765–1769, 2011.

[17] Fabio A Vittoria, Gibril KN Kallon, Dario Basta, Paul C Diemoz, Ian K Robinson, Alessandro Olivo, and Marco Endrizzi. Beam tracking approach for single–shot retrieval of absorption, refraction, and dark–field signals with laboratory x–ray sources. *Applied Physics Letters*, 106(22):224102, 2015.

[18] ES Dreier, A Bergamaschi, Gibril K Kallon, R Brönnimann, Ulrik Lund Olsen, A Olivo, and M Endrizzi. Tracking based, high-resolution single-shot multimodal x-ray imaging in the laboratory enabled by the sub-pixel resolution capabilities of the mönch detector. *Applied Physics Letters*, 117(26):264101, 2020.

[19] Maximilian von Teuffenbach, Thomas Koehler, Andreas Fehringer, Manuel Viermetz, Bernhard Brendel, Julia Herzen, Roland Proksa, Ernst J Rummeny, Franz Pfeiffer, and Peter B Noël. Grating-based phase-contrast and dark-field computed tomography: a single-shot method. *Scientific reports*, 7(1):1–8, 2017.

[20] Harold H Wen, Eric E Bennett, Rael Kopace, Ashley F Stein, and Vinay Pai. Single-shot x-ray differential phase-contrast and diffraction imaging using two-dimensional transmission gratings. *Optics letters*, 35(12):1932–1934, 2010.

[21] Binbin Wu, Yanan Liu, Christoph Rose-Petruck, and Gerald J Diebold. X-ray spatial frequency heterodyne imaging. *Applied Physics Letters*, 100(6):061110, 2012.

[22] F Krejci, Jan Jakubek, and Martin Kroupa. Single grating method for low dose 1-d and 2-d phase contrast x-ray imaging. *Journal of Instrumentation*, 6(01):C01073, 2011.

[23] C Kottler, C David, F Pfeiffer, and O Bunk. A two-directional approach for grating based differential phase contrast imaging using hard x-rays. *Optics express*, 15(3):1175–1181, 2007.

[24] P Bruša, D Panek, M Vrbova, V Fidler, and C Rose-Petruck. Spatial frequency heterodyne imaging in the soft x-ray water window. *Applied Physics Letters*, 104(25):254101, 2014.

[25] Danielle Rand, Edward G Walsh, Zoltan Derdak, Jack R Wands, and Christoph Rose-Petruck. A highly sensitive x-ray imaging modality for hepatocellular carcinoma detection in vitro. *Physics in Medicine & Biology*, 60(2):769, 2015.

[26] J Hartmann. *Bemerkungen über den Bau und die Justirung von Spektrographen*. Springer, 1900.

[27] Tomy dos Santos Rolo, Stefan Reich, Dmitry Karpov, Sergey Gasilov, Danays Kunka, Edwin Fohtung, Tilo Baumbach, and Anton Plech. A shack-hartmann sensor for single-shot multi-contrast imaging with hard x-rays. *Applied Sciences*, 8(5):737, 2018.

[28] Andrey Mikhaylov, Stefan Reich, Margarita Zakharova, Vitor Vlnieska, Roman Laptev, Anton Plech, and Danays Kunka. Shack–hartmann wavefront sensors based on 2d refractive lens arrays and super-resolution multi-contrast x-ray imaging. *Journal of synchrotron radiation*, 27(3):788–795, 2020.

[29] Stefan Reich, Tomy dos Santos Rolo, Alexander Letzel, Tilo Baumbach, and Anton Plech. Scalable, large area compound array refractive lens for hard x-rays. *Applied Physics Letters*, 112(15):151903, 2018.

[30] Han Wen, Eric E Bennett, Monica M Hegedus, and Stefanie C Carroll. Spatial harmonic imaging of x-ray scattering—initial results. *IEEE transactions on medical imaging*, 27(8):997–1002, 2008.

[31] Susanna K Lynch, Vinay Pai, Julie Auxier, Ashley F Stein, Eric E Bennett, Camille K Kemble, Xianghui Xiao, Wah-Keat Lee, Nicole Y Morgan, and Han Harold Wen. Interpretation of dark-field contrast and particle-size selectivity in grating interferometers. *Applied optics*, 50(22):4310–4319, 2011.

[32] Jens Als-Nielsen and Des McMorrow. *Elements of modern X-ray physics*. John Wiley & Sons, 2011.

[33] Henry N Chapman, Carl Caleman, and Nicusor Timneanu. Diffraction before destruction. *Philosophical Transactions of the Royal Society B: Biological Sciences*, 369(1647):20130313, 2014.

[34] Peiping Zhu, Kai Zhang, Zhili Wang, Yijin Liu, Xiaosong Liu, Ziyu Wu, Samuel A McDonald, Federica Marone, and Marco Stampanoni. Low-dose, simple, and fast grating-based x-ray phase-contrast imaging. *Proceedings of the National Academy of Sciences*, 107(31):13576–13581, 2010.

[35] I Zanette, M Bech, F Pfeiffer, and T Weitkamp. Interlaced phase stepping in phase-contrast x-ray tomography. *Applied Physics Letters*, 98(9):094101, 2011.

[36] Jian Fu, Xianhong Shi, Wei Guo, and Peng Peng. Fast x-ray differential phase contrast imaging with one exposure and without movements. *Scientific reports*, 9(1):1–8, 2019.

[37] Alberto Astolfo, Marco Endrizzi, Fabio A Vittoria, Paul C Diemoz, Benjamin Price, Ian Haig, and Alessandro Olivo. Large field of view, fast and low dose multimodal phase-contrast imaging at high x-ray energy. *Scientific reports*, 7(1):1–8, 2017.

[38] Wilhelm Conrad Röntgen. On a new kind of rays. *Science*, 3(59):227–231, 1896.

[39] Spyridon Gkoumas, Pablo Villanueva-Perez, Zhentian Wang, Lucia Romano, Matteo Abis, and Marco Stampanoni. A generalized quantitative interpretation of dark-field contrast for highly concentrated microsphere suspensions. *Scientific reports*, 6(1):1–8, 2016.

[40] Ya I Nesterets. On the origins of decoherence and extinction contrast in phase-contrast imaging. *Optics communications*, 281(4):533–542, 2008.

[41] A Malecki, G Potdevin, and F Pfeiffer. Quantitative wave-optical numerical analysis of the dark-field signal in grating-based x-ray interferometry. *EPL (Europhysics Letters)*, 99(4):48001, 2012.

[42] Thomas Koenig, Marcus Zuber, Barbara Trimborn, Tomas Farago, Pascal Meyer, Danays Kunka, Frederic Albrecht, Sascha Kreuer, Thomas Volk, Michael Fiederle, et al. On the origin and nature of the grating interferometric dark-field contrast obtained with low-brilliance x-ray sources. *Physics in Medicine & Biology*, 61(9):3427, 2016.

[43] Wataru Yashiro and Atsushi Momose. Effects of unresolvable edges in grating-based x-ray differential phase imaging. *Optics express*, 23(7):9233–9251, 2015.

[44] André Ritter, Peter Bartl, Florian Bayer, Karl C Gödel, Wilhelm Haas, Thilo Michel, Georg Pelzer, Jens Rieger, Thomas Weber, Andrea Zang, et al. Simulation framework for coherent and incoherent x-ray imaging and its application in talbot-lau dark-field imaging. *Optics express*, 22(19):23276–23289, 2014.

[45] Georg Pelzer, Gisela Anton, Florian Horn, Jens Rieger, André Ritter, Johannes Wandner, Thomas Weber, and Thilo Michel. A beam hardening and dispersion correction for x-ray dark-field radiography. *Medical physics*, 43(6Part1):2774–2779, 2016.

[46] Michael Chabior, Tilman Donath, Christian David, Oliver Bunk, Manfred Schuster, Christian Schroer, and Franz Pfeiffer. Beam hardening effects in grating-based x-ray phase-contrast imaging. *Medical physics*, 38(3):1189–1195, 2011.

[47] Yi Yang and Xiangyang Tang. The second-order differential phase contrast and its retrieval for imaging with x-ray talbot interferometry. *Medical physics*, 39(12):7237–7253, 2012.

[48] Johannes Wolf, Jonathan I Sperl, Florian Schaff, Markus Schüttler, Andre Yaroshenko, Irene Zanette, Julia Herzen, and Franz Pfeiffer. Lens-term-and edge-effect in x-ray grating interferometry. *Biomedical optics express*, 6(12):4812–4824, 2015.

[49] Youngju Kim, Jacopo Valsecchi, Jongyul Kim, Seung Wook Lee, and Markus Strobl. Symmetric talbot-lau neutron grating interferometry and incoherent scattering correction for quantitative dark-field imaging. *Scientific reports*, 9(1):1–10, 2019.

[50] Seho Lee, Ohsung Oh, Youngju Kim, Daeseung Kim, Junhyeok Won, and Seung Wook Lee. Study on dark-field imaging with a laboratory x-ray source: Random stress variation analysis based on x-ray grating interferometry. *Review of Scientific Instruments*, 92(1):015103, 2021.

[51] Pascal Mercère, Mourad Idir, Johan Floriot, and Xavier Levecq. Hartmann and shack–hartmann wavefront sensors for sub-nanometric metrology. In *Modern Developments in X-Ray and Neutron Optics*, pages 219–232. Springer, 2008.

[52] Jon B Hagen. *Radio-frequency electronics: circuits and applications*. Cambridge University Press, 2009.

[53] Max Born and Emil Wolf. *Principles of Optics: 60th Anniversary Edition*. Cambridge University Press, 7 edition, 2019. doi: 10.1017/9781108769914.

[54] Matias Kagias, Zhentian Wang, Pablo Villanueva-Perez, Konstantins Jefimovs, and Marco Stampanoni. 2d-omnidirectional hard-x-ray scattering sensitivity in a single shot. *Physical Review Letters*, 116(9): 093902, 2016.

[55] F Prade, A Yaroshenko, J Herzen, and F Pfeiffer. Short-range order in mesoscale systems probed by x-ray grating interferometry. *EPL (Europhysics Letters)*, 112(6):68002, 2016.

[56] Bernd Jähne. Digital image processing 6th revised and extended edition, 2005.

[57] Eric E Bennett, Rael Kopace, Ashley F Stein, and Han Wen. A grating-based single-shot x-ray phase contrast and diffraction method for in vivo imaging. *Medical physics*, 37(11):6047–6054, 2010.

[58] Danays Kunka, Jürgen Mohr, Vladimir Nazmov, Jan Meiser, Pascal Meyer, Maximilian Amberger, Frieder Koch, Joachim Schulz, Marco Walter, Thomas Duttenhofer, et al. Characterization method for new resist formulations for har patterns made by x-ray lithography. *Microsystem technologies*, 20 (10-11):2023–2029, 2014.

[59] Genta Sato, Takeshi Kondoh, Hidenosuke Itoh, Soichiro Handa, Kimiaki Yamaguchi, Takashi Nakamura, Kentaro Nagai, Chidane Ouchi, Takayuki Teshima, Yutaka Setomoto, et al. Two-dimensional gratings-based phase-contrast imaging using a conventional x-ray tube. *Optics letters*, 36(18):3551–3553, 2011.

[60] FM Schunk, D Rand, and C Rose-Petruck. Spatial frequency heterodyne imaging of aqueous phase transitions inside multi-walled carbon nanotubes. *Physical Chemistry Chemical Physics*, 17(46):31237–31246, 2015.

[61] Michael S Hibbs. System overview of optical. *Microlithography: Science and Technology*, page 1, 1998.

[62] G Weber. X-Ray attenuation and absorption calculator. `http://www.web-docs.gsi.de/~stoe_exp/web_programs/x_ray_absorption/index.php`, 2017. Online; accessed on 2017-06-17.

[63] Kaye S Morgan, David M Paganin, and Karen KW Siu. Quantitative single-exposure x-ray phase contrast imaging using a single attenuation grid. *Optics express*, 19(20):19781–19789, 2011.

[64] Fabio A Vittoria, Marco Endrizzi, Paul C Diemoz, Anna Zamir, Ulrich H Wagner, Christoph Rau, Ian K Robinson, and Alessandro Olivo. X–ray absorption, phase and dark–field tomography through a beam tracking approach. *Scientific reports*, 5(1):1–5, 2015.

[65] Stefan Reich. *Hierarchical imaging of the dynamics during pulsed laser ablation in liquids*. PhD thesis, KIT-Bibliothek, 2019.

[66] Sebastian Kaeppler, Florian Bayer, Thomas Weber, Andreas Maier, Gisela Anton, Joachim Hornegger, Matthias Beckmann, Peter A Fasching, Arndt Hartmann, Felix Heindl, et al. Signal decomposition for x-ray dark-field imaging. In *International Conference on Medical Image Computing and Computer-Assisted Intervention*, pages 170–177. Springer, 2014.

[67] A Snigirev, I Snigireva, V Kohn, S Kuznetsov, and I Schelokov. On the possibilities of x-ray phase contrast microimaging by coherent high-energy synchrotron radiation. *Review of scientific instruments*, 66(12):5486–5492, 1995.

[68] Atsushi Momose, Shinya Kawamoto, Ichiro Koyama, Yoshitaka Hamaishi, Kengo Takai, and Yoshio Suzuki. Demonstration of x-ray talbot interferometry. *Japanese journal of applied physics*, 42(7B): L866, 2003.

[69] TJ Davis, D Gao, TE Gureyev, AW Stevenson, and SW Wilkins. Phase-contrast imaging of weakly absorbing materials using hard x-rays. *Nature*, 373(6515):595–598, 1995.

[70] Kaye S Morgan, David M Paganin, and Karen KW Siu. X-ray phase imaging with a paper analyzer. *Applied Physics Letters*, 100(12):124102, 2012.

[71] Yanan Liu, Brian Ahr, Alexander Linkin, Gerald J Diebold, and Christoph Rose-Petruck. X-ray spatial harmonic imaging of phase objects. *Optics letters*, 36(12):2209–2211, 2011.

[72] Atsushi Momose, Wataru Yashiro, Hirohide Maikusa, and Yoshihiro Takeda. High-speed x-ray phase imaging and x-ray phase tomography with talbot interferometer and white synchrotron radiation. *Optics express*, 17(15):12540–12545, 2009.

[73] MP Olbinado, J Grenzer, P Pradel, T De Resseguier, P Vagovic, M-C Zdora, VA Guzenko, C David, and A Rack. Advances in indirect detector systems for ultra high-speed hard x-ray imaging with synchrotron light. *Journal of Instrumentation*, 13(04):C04004, 2018.

[74] Alexander Letzel, Stefan Reich, Tomy dos Santos Rolo, Alexander Kanitz, Jan Hoppius, Alexander Rack, Margie P Olbinado, Andreas Ostendorf, Bilal Gökce, Anton Plech, et al. Time and mechanism of nanoparticle functionalization by macromolecular ligands during pulsed laser ablation in liquids. *Langmuir*, 35(8):3038–3047, 2019.

[75] Oliver Preusche. Choosing sensitivity to reduce x-ray dose in medical phase contrast imaging. *Optics express*, 26(8):10339–10357, 2018.

[76] Volker Saile, Ulrike Wallrabe, Osamu Tabata, and Jan G Korvink. *LIGA and its Applications*, volume 7. Wiley Online Library, 2009.

[77] Margarita Zakharova, Vitor Vlnieska, Heike Fornasier, Martin Börner, Tomy dos Santos Rolo, Jürgen Mohr, and Danays Kunka. Development and characterization of two-dimensional gratings for single-shot x-ray phase-contrast imaging. *Applied Sciences*, 8(3):468, 2018.

[78] Nima Arjmandi. *Resist Homogeneity*. InTech, 2013.

[79] Margarita Zakharova, Stefan Reich, Andrey Mikhaylov, Vitor Vlnieska, Tomy dos Santos Rolo, Anton Plech, and Danays Kunka. Inverted hartmann mask for single-shot phase-contrast x-ray imaging of dynamic processes. *Optics letters*, 44(9):2306–2309, 2019.

[80] Shyjumon Ibrahimkutty, Philipp Wagener, Andreas Menzel, Anton Plech, and Stephan Barcikowski. Nanoparticle formation in a cavitation bubble after pulsed laser ablation in liquid studied with high time resolution small angle x-ray scattering. *Applied Physics Letters*, 101(10):103104, 2012.

[81] Stefan Reich, Patrick Schönfeld, Philipp Wagener, Alexander Letzel, Shyjumon Ibrahimkutty, Bilal Gökce, Stephan Barcikowski, Andreas Menzel, Tomy dos Santos Rolo, and Anton Plech. Pulsed laser ablation in liquids: Impact of the bubble dynamics on particle formation. *Journal of colloid and interface science*, 489:106–113, 2017.

[82] Konstantin M Pavlov, Heyang Thomas Li, David M Paganin, Sebastien Berujon, Hélène Rougé-Labriet, and Emmanuel Brun. Single-shot x-ray speckle-based imaging of a single-material object. *Physical Review Applied*, 13(5):054023, 2020.

[83] Genta Sato, Hidenosuke Itoh, Kentaro Nagai, Takashi Nakamura, Kimiaki Yamaguchi, Takeshi Kondoh, Soichiro Handa, Chidane Ouchi, Takayuki Teshima, Yutaka Setomoto, et al. Single-shot x-ray phase-contrast imaging using two-dimensional gratings. In *AIP Conference Proceedings*, volume 1466, pages 29–34. American Institute of Physics, 2012.

[84] Atsushi Momose, Wataru Yashiro, Sébastien Harasse, and Hiroaki Kuwabara. Four-dimensional x-ray phase tomography with talbot interferometry and white synchrotron radiation: dynamic observation of a living worm. *Optics express*, 19(9):8423–8432, 2011.

[85] Mutairu B Olatinwo, Kyungmin Ham, Jonathan McCarney, Shashidhara Marathe, Jinghua Ge, Gerry Knapp, and Leslie G Butler. Analysis of flame retardancy in polymer blends by synchrotron x-ray k-edge tomography and interferometric phase contrast movies. *The Journal of Physical Chemistry B*, 120(9): 2612–2624, 2016.

[86] Stefan Reich, Jörg Göttlicher, Anna Ziefuss, René Streubel, Alexander Letzel, Andreas Menzel, Olivier Mathon, Sakura Pascarelli, Tilo Baumbach, Marcus Zuber, et al. In situ speciation and spatial mapping of zn products during pulsed laser ablation in liquids (plal) by combined synchrotron methods. *Nanoscale*, 12(26):14011–14020, 2020.

[87] Jianrong Zeng, Guilin Zhang, Shilei Long, Ke Liu, Lingling Cao, Liangman Bao, and Yan Li. Sea salt deliquescence and crystallization in atmosphere: an in situ investigation using x-ray phase contrast imaging. *Surface and interface analysis*, 45(5):930–936, 2013.

[88] Linda CP Croton, Kaye S Morgan, David M Paganin, Lauren T Kerr, Megan J Wallace, Kelly J Crossley, Suzanne L Miller, Naoto Yagi, Kentaro Uesugi, Stuart B Hooper, et al. In situ phase contrast x-ray brain ct. *Scientific reports*, 8(1):1–12, 2018.

[89] Kristin Høydalsvik, Jostein Bø Fløystad, Tiejun Zhao, Morteza Esmaeili, Ana Diaz, Jens W Andreasen, Ragnvald H Mathiesen, Magnus Rønning, and Dag W Breiby. In situ x-ray ptychography imaging of high-temperature co2 acceptor particle agglomerates. *Applied physics letters*, 104(24):241909, 2014.

[90] FJ Koch, TJ Schröter, D Kunka, P Meyer, J Meiser, A Faisal, MI Khalil, L Birnbacher, M Viermetz, M Walter, et al. Note: Gratings on low absorbing substrates for x-ray phase contrast imaging. *Review of Scientific Instruments*, 86(12):126114, 2015.

[91] M Zakharova, S Reich, A Mikhaylov, V Vlnieska, Marcus Zuber, Sabine Engelhardt, T Baumbach, and D Kunka. A comparison of customized hartmann and newly introduced inverted hartmann masks for single-shot phase-contrast x-ray imaging. In *EUV and X-ray Optics: Synergy between Laboratory and Space VI*, volume 11032, page 110320U. International Society for Optics and Photonics, 2019.

[92] Stefan Reich and Anton Plech. Shack-hartman sensor wavefront reconstruction software, 2018. 56.03.20; LK 01.

[93] Biswajit Pathak and Bosanta R Boruah. Improved wavefront reconstruction algorithm for shack–hartmann type wavefront sensors. *Journal of Optics*, 16(5):055403, 2014.

[94] Han Wen, Eric E Bennett, Monica M Hegedus, and Stanislas Rapacchi. Fourier x-ray scattering radiography yields bone structural information. *Radiology*, 251(3):910–918, 2009.

[95] SK Sinha, EB Sirota, S Garoff, and HB Stanley. X-ray and neutron scattering from rough surfaces. *Physical Review B*, 38(4):2297, 1988.

[96] Robert Andersson, Léon F Van Heijkamp, Ignatz M De Schepper, and Wim G Bouwman. Analysis of spin-echo small-angle neutron scattering measurements. *Journal of Applied Crystallography*, 41(5): 868–885, 2008.

[97] Marcus John Kitchen, D Paganin, Robert A Lewis, Naoto Yagi, K Uesugi, and Stephen Thomas Mudie. On the origin of speckle in x-ray phase contrast images of lung tissue. *Physics in medicine & biology*, 49(18):4335, 2004.

[98] Oral Oltulu, Zhong Zhong, Moumen Hasnah, Miles N Wernick, and Dean Chapman. Extraction of extinction, refraction and absorption properties in diffraction enhanced imaging. *Journal of Physics D: Applied Physics*, 36(17):2152, 2003.

[99] Keith A Nugent, Chanh Quoc Tran, and A Roberts. Coherence transport through imperfect x-ray optical systems. *Optics express*, 11(19):2323–2328, 2003.

[100] IA Vartanyants and IK Robinson. Origins of decoherence in coherent x-ray diffraction experiments. *Optics communications*, 222(1-6):29–50, 2003.

[101] Matias Kagias, Zhentian Wang, Goran Lovric, Konstantins Jefimovs, and Marco Stampanoni. Simultaneous reciprocal and real space x-ray imaging of time-evolving systems. *Physical Review Applied*, 15 (4):044038, 2021.

[102] Timofei Krouglov, Ignatz M De Schepper, Wim G Bouwman, and M Theo Rekveldt. Real-space interpretation of spin-echo small-angle neutron scattering. *Journal of applied crystallography*, 36(1): 117–124, 2003.

[103] CJR Sheppard. Scattering by fractal surfaces with an outer scale. *Optics communications*, 122(4-6): 178–188, 1996.

[104] R Andersson, WG Bouwman, S Luding, and IM De Schepper. Stress, strain, and bulk microstructure in a cohesive powder. *Physical Review E*, 77(5):051303, 2008.

[105] Martin Hunter, Vadim Backman, Gabriel Popescu, Maxim Kalashnikov, Charles W Boone, Adam Wax, Venkatesh Gopal, Kamran Badizadegan, Gary D Stoner, and Michael S Feld. Tissue self-affinity and polarized light scattering in the born approximation: a new model for precancer detection. *Physical review letters*, 97(13):138102, 2006.

[106] Richard F Voss. Random fractal forgeries. In *Fundamental algorithms for computer graphics*, pages 805–835. Springer, 1985.

[107] Martin Prostredny, Ashleigh Fletcher, and Paul Mulheran. Modelling the formation of porous organic gels–how structural properties depend on growth conditions. *RSC advances*, 9(35):20065–20074, 2019.

[108] Wataru Yashiro, Sébastien Harasse, Katsuyuki Kawabata, Hiroaki Kuwabara, Takashi Yamazaki, and Atsushi Momose. Distribution of unresolvable anisotropic microstructures revealed in visibility-contrast images using x-ray talbot interferometry. *Physical Review B*, 84(9):094106, 2011.

[109] Ohio Carbon Blank, Inc. Graphite Supplier and Graphite Machining: EDM-AF5®. `https://www.ohiocarbonblank.com/index.php?file=graphitematerial_detail&url=edm-af5`, 2019. Online; accessed 2021-06-17.

[110] Ohio Carbon Blank, Inc. Material specification information. `https://www.ohiocarbonblank.com/index.php?file=template&url=material-specifications`, 2019. Online; accessed 2021-06-17.

[111] Entegris, Inc. Properties and characteristics of graphite. `https://www.entegris.com/content/dam/web/resources/brochures/brochure-properties-and//-characteristics-of-graphite-7329.pdf`, 2013. Online; accessed 2021-06-17.

[112] PM Adler and J-F Thovert. Fractal porous media. *Transport in porous media*, 13(1):41–78, 1993.

[113] Micha Borkovec, Walter De Paris, and Ronald Peikert. The fractal dimension of the apollonian sphere packing. *Fractals*, 2(04):521–526, 1994.

[114] José S Andrade Jr, Hans J Herrmann, Roberto FS Andrade, and Luciano R Da Silva. Apollonian networks: Simultaneously scale-free, small world, euclidean, space filling, and with matching graphs. *Physical review letters*, 94(1):018702, 2005.

[115] Luděk Klimeš. Correlation functions of random media. *Pure and applied geophysics*, 159(7):1811–1831, 2002.

[116] Maxim Kalashnikov, Wonshik Choi, Chung-Chieh Yu, Yongjin Sung, Ramachandra R Dasari, Kamran Badizadegan, and Michael S Feld. Assessing light scattering of intracellular organelles in single intact living cells. *Optics express*, 17(22):19674–19681, 2009.

[117] Kirsten Taphorn, Fabio De Marco, Jana Andrejewski, Thorsten Sellerer, Franz Pfeiffer, and Julia Herzen. Grating-based spectral x-ray dark-field imaging for correlation with structural size measures. *Scientific Reports*, 10(1):1–9, 2020.

[118] Kirsten Taphorn, Korbinian Mechlem, Thorsten Sellerer, Fabio De Marco, Manuel Viermetz, Franz Pfeiffer, Daniela Pfeiffer, and Julia Herzen. Direct differentiation of pathological changes in the human lung parenchyma with grating-based spectral x-ray dark-field radiography. *IEEE Transactions on Medical Imaging*, 40(6):1568–1578, 2021.

[119] Michael Helmberger, Michael Pienn, Martin Urschler, Peter Kullnig, Rudolf Stollberger, Gabor Kovacs, Andrea Olschewski, Horst Olschewski, and Zoltan Balint. Quantification of tortuosity and fractal dimension of the lung vessels in pulmonary hypertension patients. *PloS one*, 9(1):e87515, 2014.

[120] I Zanette, Tunhe Zhou, Anna Burvall, Ulf Lundström, Daniel H Larsson, M Zdora, P Thibault, Franz Pfeiffer, and Hans M Hertz. Speckle-based x-ray phase-contrast and dark-field imaging with a laboratory source. *Physical review letters*, 112(25):253903, 2014.

[121] Sebastien Berujon, Hongchang Wang, and Kawal Sawhney. X-ray multimodal imaging using a random-phase object. *Physical Review A*, 86(6):063813, 2012.

[122] Francesco Dallari, Avni Jain, Marcin Sikorski, Johannes Möller, Richard Bean, Ulrike Boesenberg, Lara Frenzel, Claudia Goy, Jörg Hallmann, Yoonhee Kim, et al. Microsecond hydrodynamic interactions in dense colloidal dispersions probed at the european xfel. *IUCrJ*, 8(5), 2021.

[123] RP Harti, J Valsecchi, P Trtik, D Mannes, C Carminati, Markus Strobl, Jeroen Plomp, CP Duif, and Christian Grünzweig. Visualizing the heterogeneous breakdown of a fractal microstructure during compaction by neutron dark-field imaging. *Scientific reports*, 8(1):1–10, 2018.

[124] Fei Yang, Friedrich Prade, Michele Griffa, Rolf Kaufmann, Julia Herzen, Franz Pfeiffer, and Pietro Lura. X-ray dark-field contrast imaging of water transport during hydration and drying of early-age cement-based materials. *Materials Characterization*, 142:560–576, 2018.

[125] Sheridan C Mayo, Andrew W Stevenson, and Stephen W Wilkins. In-line phase-contrast x-ray imaging and tomography for materials science. *Materials*, 5(5):937–965, 2012.

[126] Timm Weitkamp, Ana Diaz, Christian David, Franz Pfeiffer, Marco Stampanoni, Peter Cloetens, and Eric Ziegler. X-ray phase imaging with a grating interferometer. *Optics express*, 13(16):6296–6304, 2005.

[127] Danielle Rand, Zoltan Derdak, Rolf Carlson, Jack R Wands, and Christoph Rose-Petruck. X-ray scatter imaging of hepatocellular carcinoma in a mouse model using nanoparticle contrast agents. *Scientific reports*, 5(1):1–15, 2015.